STARS

University of Central Florida
STARS

Electronic Theses and Dissertations, 2004-2019

2007

Far-infrared/millimeter Wave Source And Component Development For Imaging And Spectroscopy

Todd Du Bosq
University of Central Florida

 Part of the Physics Commons
Find similar works at: https://stars.library.ucf.edu/etd
University of Central Florida Libraries http://library.ucf.edu

This Doctoral Dissertation (Open Access) is brought to you for free and open access by STARS. It has been accepted for inclusion in Electronic Theses and Dissertations, 2004-2019 by an authorized administrator of STARS. For more information, please contact STARS@ucf.edu.

STARS Citation

Du Bosq, Todd, "Far-infrared/millimeter Wave Source And Component Development For Imaging And Spectroscopy" (2007). *Electronic Theses and Dissertations, 2004-2019*. 3149.
https://stars.library.ucf.edu/etd/3149

FAR-INFRARED/MILLIMETER WAVE SOURCE AND COMPONENT DEVELOPMENT FOR IMAGING AND SPECTROSCOPY

by

TODD WILLIAM DU BOSQ
B.S. Stetson University, 2001
M.S. University of Central Florida, 2003

A dissertation submitted in partial fulfillment of the requirements
for the degree of Doctor of Philosophy
in the Department of Physics
in the College of Sciences
at the University of Central Florida
Orlando, Florida

Spring Term
2007

Major Professors: Glenn D. Boreman
and Robert E. Peale

© 2007 Todd William Du Bosq

ABSTRACT

The far-infrared and millimeter wave (FIR/mmW) (wavelength 75 μm to 10 mm) portion of the electromagnetic spectrum is fairly underdeveloped technologically, owing to the large amount of atmospheric attenuation in that range. At present, the FIR/mmW region is lacking in compact, high-brightness radiation sources and practical imaging systems. This dissertation focuses on development of two complementary technologies in this area – an active mmW imaging system and high-reflectivity Bragg mirrors for the FIR p-Ge laser. The imaging system uses a vector network analyzer in the frequency range of 90-140 GHz as the radiation source and receiver. Raster scanning is used to map a two-dimensional field of view, demonstrating the detection and imaging of buried plastic landmines. Principal components analysis is used for hyperspectral signal processing, where a series of images is taken at discrete frequencies. Results are obtained as a function of depth and disturbance of the soil surface. In support of this study, various types of soils were characterized for scattering loss across the mmW/FIR region, with measured results compared to theory. This mmW imaging system was also used to demonstrate imaging through walls and other obscuring materials, as well as for imaging of rocks beneath volcanic sand, simulating the conditions encountered by an imaging system on a Mars rover vehicle. Furthermore, a high-reflectivity Si-etalon FIR mirror design was developed and demonstrated as a cavity mirror for the p-Ge laser. These components stand to have a number of systems-level impacts on FIR imagers. In the context of an active illuminator, they may allow narrowband selection from the broad emission spectrum of the p-Ge laser source. These mirrors can also be used in a Fabry-Perot FIR scanning spectrometer, where the resulting high finesse would give discrimination advantages in chemical sensing and astrophysical spectroscopy applications.

To my loving family past, present, and future

ACKNOWLEDGMENTS

I would like to acknowledge my research advisors Dr. Glenn Boreman and Dr. Robert Peale for their advice, patience, and guidance throughout my time as a research assistant at the University of Central Florida. The knowledge and experience that I have gained from both of them is truly invaluable.

The majority of this research was funded by the Northrop Grumman Corporation and I would like to acknowledge David Muh, Dan Dillery, and Jeff Grantham for their continued support of this research.

I would like to acknowledge the Anritsu Company for favorable pricing on the vector network analyzer ME7808A used in this research.

I would like to acknowledge all of the past and present members of the IR Systems Lab and p-Ge Laser Lab with whom I have learned, laughed, and shared Krispy Kreme doughnuts with. I especially thank Guy Zummo for his ability to create just about anything I could conjure up. I also acknowledge Dr. Jose Manuel Lopez-Alonso and Dr. Javier Alda for their guidance and expertise on signal processing. I would also like to acknowledge Justin Cleary for his collaboration on the scanning Fabry-Perot filter.

I acknowledge my advisory committee, Dr. Brian Lail, and Dr. Daniel Britt, for their helpful insight to my research.

I would like to thank all of my friends who have provided constant support and happiness throughout my graduate career. I also thank my fellow rock climbers and game nighters for their constant companionship while providing an alternative to my daily research.

I acknowledge my family, in particular my parents, Chris, Ander, Jackie, Kenzie, and Mikey for all of their unconditional love and support.

Above all, I would like to thank Marianna for her love, patience, thoughtfulness, and ability to make each day better than the last.

TABLE OF CONTENTS

LIST OF FIGURES

LIST OF TABLES

LIST OF ABBREVIATIONS/ACRONYMS

a	Radius of the Sphere
A_s	Scattering cross sectional area
A	Ampere
a.u.	Arbitrary Units
atm	Atmospheric pressure
B	Magnetic Field
BWO	Backward Wave Oscillator
c	Speed of light
$CaCO_3$	Calcium Carbonate
cm	10^{-2} meters
cm^{-1}	Wavenumber
cm^2	Squared centimeter
cm^{-3}	Per cubic centimeter
CO_2	Carbon Dioxide
D	Diameter of lens
d	Diffraction limited spot size
dB	Decibel
dB/km	Decibels per kilometer
D_{exit}	Diameter of the exit pupil
d_i	Image distance

d_j	Thickness of the j^{th} layer
dL	Fractional path length
dP	Power lost per unit area
E	Electric Field
$\vec{E}_m$	Electric vector
f	Focal length
F	Finesse
f/#	f-number of the system
Far-IR	Far-infrared
Fe_2O_3	Iron Oxide
FEL	Free Electron Laser
FTIR	Fourier Transform Infrared Spectrometer
g	gram
Ga	Gallium
GaAs	Gallium Arsenide
Ge	Germanium
GHz	10^9 Hertz
H_2O	Water
HDPE	High Density Polyethylene
Hg	Mercury
$\vec{H}_m$	Magnetic vector
IF	Intermediate Frequency

InP	Indium Phosphate
InSb	Indium Antimonide
K	Kelvin
k	Resonance order
k_j	Extinction coefficient of j^{th} layer
kV/cm	Kilovolts per centimeter
L	Length
L_{Ge}	Length of the germanium crystal
$\vec{M}$	Product matrix of multilayer mirror
m	Meter
m^{-3}	Per cubic meter
MHz	10^6 Hertz
$\vec{M}_j$	j^{th} layer of the Bragg mirror
mm	10^{-3} meters
mm/s	Millimeter per second
mmW	Millimeter wave
m_s	Ratio of the index of the sphere to the index of the medium
mW	10^{-3} Watts
N_s	Number of spheres per unit volume
N	Number of random variables
N_A	Doping concentration
n_j	Index of refraction of the j^{th} layer

n_{lens}	Index of refraction of the lens
n_{med}	Index of refraction of the medium
n_{oil}	Index of Refraction of Oil
n_{quartz}	Index of Refraction of Quartz
NRCS	National Resource Conservation Service
n_{sph}	Index of refraction of the sphere
NVESD	Night Vision and Electronic Sensors Directorate
O_2	Molecular oxygen
Ohm-cm	Ohm centimeters
OIWC	Objective Individual Combat Weapon
P	Transmitted Power
PCA	Principal Component Analysis
p-Ge	p-type doped Germanium
P_I	Incident Power
PS	Polystyrene
q	Number of layers
QCL	Quantum Cascade Laser
R	Reflectivity
r	Reflection coefficient
rad	Radian
R_{max}	Maximum Reflectivity
R_{min}	Minimum Reflectivity

Si	Silicon
SiO_2	Silicon Dioxide
SNR	Signal to Noise Ratio
$SrTiO_3$	Strontium Titanate
STD	Standard Deviation
T	Tesla
T_s	Transmittance
ThF_4	Thorium fluoride
THz	10^{12} Hertz
TiO_2	Titanium Dioxide
UXO	Unexploded Ordnance
V	Volt
VNA	Vector Network Analyzer
V_{sph}	Volume of the sphere
W	Watts
WWII	World War II
x	Spatial coordinate
Y_α	Principal components
ZrO_2	Zirconium dioxide

Symbols

“	Inch

°C	Degree Celcius

Greek Letters

α	Laser gain
α_{abs}	Absorption attenuation coefficient
α_{liq}	Absorption attenuation coefficient of liquid
α_{sct}	Power scattering attenuation coefficient
α_{total}	Total power attenuation coefficient
β_{ast}	Astigmatism blur
β_{diff}	Diffraction blur
β_{coma}	Coma blur
β_{sph}	Spherical aberration blur
Δd	Full-width at half maximum of transmission maxima
δ	Minimum resolvable separation
δz'	Depth of focus
θ	Half field angle
θ_j	Angle of refraction of j^{th} layer
η_m	Effective refractive index of incident medium
η_s	Effective refractive index of medium behind mirror
λ	Wavelength
μm	10^{-6} meters

μs	10^{-6} seconds
μW	10^{-6} Watts
ν	Frequency
ρ	Packing density

CHAPTER 1: INTRODUCTION

Electromagnetic radiation varies by wavelength (or frequency, since the speed of light is equal to the frequency multiplied by the wavelength). The electromagnetic spectrum consists of radiation classified by its wavelength (or frequency). Various bands of the electromagnetic spectrum are referred to by particular names. These regions often overlap and the boundaries are not precise. Many times, the ranges of the bands vary depending on the components used to generate the radiation. For the purposes of this dissertation, the millimeter wave (mmW) range will be defined from 10 mm to 1 mm (30 GHz to 300 GHz) and the far-infrared or terahertz range will be defined from 1 mm to 20 μm (0.3 THz to 15 THz).

Portions of the far-infrared and mmW (75 μm to 10 mm or 4 THz to 30 GHz) ranges are fairly underdeveloped, lacking many useful sources, components, or proven applications. Part of this is due to the absorption of the atmosphere in these wavelength regions, shown in Figure 1. Some regions in these bands are attenuated close to 1000 dB/km [1]. The region below 15 GHz has relatively low atmospheric absorption. The 15-360 GHz range contains five absorption bands. Three absorption bands are due to the rotational energy level of water vapor [2-4] at 22.23 GHz, 183.31 GHz, and 325.15 GHz. At 60 GHz, the absorption band of atmospheric oxygen is produced by magnetic-dipole transitions between fine structure rotational energy levels [5]. A second absorption line from oxygen is located at 118.75 GHz [3-4]. The region above 360 GHz contains many atmospheric absorption lines due to water vapor [6-7].

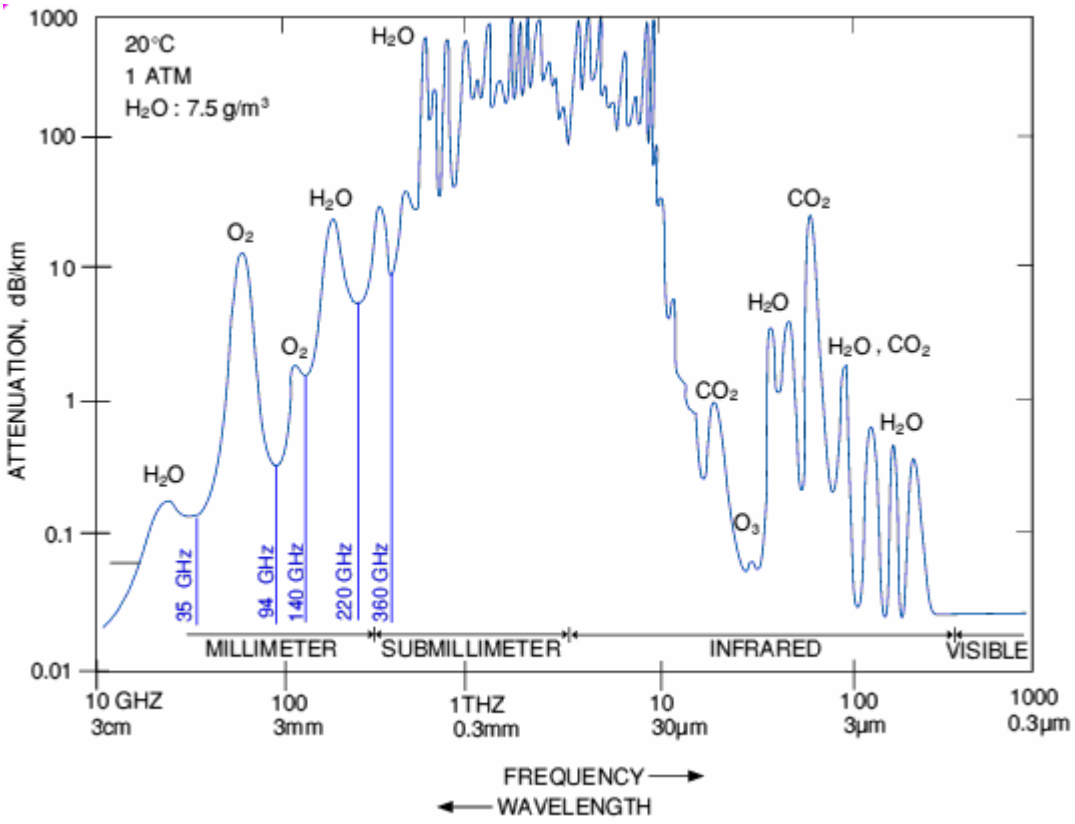

Figure 1: Atmospheric Attenuation from 10 GHz to 1000 THz [1]

The progress of THz and mmW sources consist of the extension of microwave electronics towards higher frequencies or the development of photonic devices from the optical region towards lower frequencies. Most of the sources suffer from certain disadvantages such as power, size, wavelength tuning, and cryogenic cooling. The major mmW and THz sources include vector network analyzers, Gunn oscillators, backward wave oscillators, mercury arc lamps, globar lamps, optically pumped gas lasers, p-germanium lasers, quantum cascade lasers, and free electron lasers. Each of these sources will be discussed below including their advantages and disadvantages, which are summarized in Table 1.

Vector network analyzers (VNA) are a common multi-port electronic test device used in the characterization of passive and active electric networks - including amplifiers, microwave filters, antennas, and waveguides [8]. Characterization occurs by measuring the ratio (phase and magnitude) of an incident signal from the VNA's signal generator to the reflected and transmitted signal at each of the device under test's ports. With these ratios, it is possible to calculate the device's s-parameters and, subsequently, gain, insertion loss, characteristic impedance, or other merits of interest. For generating signals at mmW, the VNA does not internally generate signals at the test frequency but instead relies on external modules to upconvert the incident signal and downcovert the returned signal. The magnitude of the returned signal is found using a superheterodyne receiver. Frequency sampling occurs by mixing the received signal with a signal from a tunable oscillator and then passing the resulting signal through an intermediate frequency (IF) filter. The phase of the received signal can be determined by comparing the phase of the source signal from the signal generator to the received. Phase differences introduced by path difference can be readily corrected in software. Typical VNA's in the mmW range operate from 0.04-325 GHz with an output power of 10 mW to a few μW [9]. The system does not require cryogenic cooling but is large, requiring a rack of electronics for operation.

Gunn diode oscillators or transfer electron devices consist of three layers of n-doped semiconductor, usually GaAs or InP [10-12]. The two outer layers are heavily doped with a thin lightly doped layer in between. When a voltage is applied to the device, the electrical gradient is largest across the thin middle layer. This layer starts to conduct, reducing the electrical gradient across the layer, which prevents further conduction. The electron concentration distribution

causes a region of accumulation and depletion growing in amplitude as it propagates from cathode to anode resulting in an oscillating current. Changing the doping concentration and the length of the layers, Gunn oscillators can operate from 10 GHz to 400 GHz with output power from 400 mW-1 mW [10]. They are compact sources and are not cryogenically cooled. Gunn oscillators can be electrically tuned about 200 MHz [10] and mechanically tuned using a micrometer screw 0.05-20 GHz [13].

Backward wave oscillators (BWO) are electro-vacuum diodes [14-17]. A heated cathode emits electrons which are accelerated by the high voltage and focused by the magnetic field. The electrons travel toward the anode over a comb-like decelerating system. Grouped in clusters, the electrons form an electromagnetic wave which travels in the opposite direction. The radiation exits into free space through an oversized waveguide. The BWO wavelengths are tuned by changing the applied voltage to the cathode. BWO operate from 30 GHz to 2.5 THz [14-15] with an output power of 100 mW-1 μW [17]. The system is large and does not need cryogenic cooling.

A mercury arc lamp is a bulb containing electrodes in a mercury gas. Power is applied to the electrodes creating an arc. This causes the pressure of the gas to increase. The mercury gas starts to ionize producing the far-infrared light. Mercury arc lamps emit from 120 GHz to 6 THz with very low spectral power density. The mercury arc lamp is compact and does not need cryogenic cooling.

Globar lamps are silicon carbide rods that are electrically heated. The heated silicon carbide becomes a graybody radiator producing the far-infrared radiation. A globar lamp emits from 300 GHz to 300 THz with very low spectral power density. A globar lamp is compact and does not require cryogenic cooling.

Optically pumped gas lasers use a grating-tuned CO_2 laser to pump the THz laser [18-19]. The pump laser is admitted through a small hole in one of the end mirrors of the laser cavity. The vacuum cavity is filled with a molecular gas at low pressure. The gas laser operates on molecular rotational transitions from the gas. An infrared photon, with energy close to the transition from a particular rotational state in the ground vibrational manifold to a rotational state in an excited vibrational manifold, is absorbed by the gas molecule [19]. This causes a population inversion between the two rotational states. The inverted transition lases in the THz range. The molecule is left in the excited vibrational manifold and returns to the ground manifold. The gas laser operates at many discrete lines from 0.3-7 THz using different gasses and cavity pressure [19], but is not continuously tunable. Gas laser output power ranges from 1-125 mW [19]. The system is large and operates at room temperature.

The p-Ge laser consists of a germanium crystal doped with gallium [20-23]. The end faces of the laser are polished parallel to each other. Two flat mirrors are attached directly to the end faces of the laser. One mirror is smaller than the crystal end face to allow output coupling. Ohmic contacts for applying high-voltage across the crystal are attached to the two narrow lateral faces of the crystal. The system is inserted into a superconducting solenoid or permanent magnet and

immersed in liquid helium. The mechanism of amplification of terahertz radiation in bulk p-Ge is based on direct optical transitions between light and heavy-hole valence sub-bands in strong crossed electric **E** and magnetic **B** fields [20]. Population inversion builds up at low temperatures for certain ratios E/B, when light holes are accumulated on closed trajectories below the optical phonon energy, while heavy holes are strongly scattered by optical phonons. Gain occurs over a broad range of wavelengths, depending on the applied fields. Without special selective cavities, the gain bandwidth is approximately 20 cm^{-1} and can be shifted by changing the E and B fields. Wavelength selection is achieved using silicon intracavity etalons or lamellar mirrors [21-23]. The p-Ge laser operates from 1.5-4.2 THz with an output peak power of 1 W [21-22].

The quantum cascade laser (QCL) [24-25] consists of alternating layers of two different semiconductors, an injector and an active region. Applying an electric field to the device, an electric sub-band minimum in a given period may be aligned with a higher energy sub-band minimum in the next period. A population inversion will occur and the electrons will transition to the lower energy level emitting THz photons. The electrons then tunnel to another quantum well and the injector region couples them to the higher energy level in the active region. The electrons cascade through many periods of the structure emitting photons. The wavelength of the radiation is determined by the thickness of the layers and their material properties. QCL operate at discrete frequencies from 1.9-5.0 THz [24] with output powers of 250 mW to a few μW [24-25]. QCL are not tunable and a different device must be made for each frequency needed. QCL are small but require cryogenic cooling.

A free electron laser (FEL) [26-28] is produced by accelerating a beam of electrons through a periodic transverse magnetic field. This field is created by placing magnets of alternating poles along the electron beam path. The alternating poles cause the electrons to oscillate sinusoidally releasing a photon [28]. Mirrors collimate the photons to create laser gain. The wavelength can be continuously tuned by adjusting the magnetic field strength or the electron beam energy. To produce the electrons for the FEL, an electron accelerator is used, such as a synchrotron or linac. The FEL can operate throughout the entire 0.1-10 THz range producing 100's of W of output power [28]. This source is extremely large and does not require cryogenic cooling.

Table 1: Advantages and Disadvantages of Current mmW and THz Sources

mmW/THz source	Advantages	Disadvantages
Vector Network Analyzer (0.04-325 GHz)	• Wavelength Tunable • Non-cooled	• Power (10 mW- a few μW) • Large System
Gunn Oscillator (10-400 GHz)	• Power (lower frequencies 400 mW) • Non-cooled • Compact System	• Power (Higher frequencies 1 mW) • Limited Wavelength Tuning
Backward Wave Oscillator (0.03-2.5 THz)	• Power (Lower frequencies 100 mW) • Non-cooled • Wavelength Tunable	• Power (Higher frequencies 1 μW) • Large System
Mercury Arc Lamp 0.12-6 THz	• Non-cooled • Continuous Spectrum • Compact Source	• Low power
Globar 0.3-300 THz	• Non-cooled • Continuous Spectrum • Compact Source	• Low power
Optically Pumped Gas Laser (0.3-7 THz)	• Power (Some lines 125 mW) • Non-cooled	• Power (Some lines 1 mW) • Discrete Line Tunability • Large System
p-Ge Laser (1.5-4.2 THz)	• Power (1 W peak power) • Wavelength Tunable • Laser is small	• Cryogenically Cooled • Large System due to Cooling
Quantum Cascade Laser (1.9-5.0 THz)	• Power (Higher Frequencies 250 mW) • Laser is small	• Power (Lower Frequencies a few μW) • Cryogenically Cooled • Non-tunable • Large System due to Cooling
Free Electron Laser (0.1-10 THz)	• High Power (100's of W) • Wavelength Tunable • Non-cooled	• Very Large System (requires an electron accelerator)

Along with sources, another challenge in the mmW and THz regions are the detectors and components used in the system. Some detectors include [29-30] helium cooled Si, Ge, and InSb bolometers, pyroelectric detectors, quantum dot detectors, Schottky diodes, electronic resonant detectors, photoconductive antennas, metal-oxide-metal diodes, and the golay cell. As with the sources, most of these detectors have their disadvantages associated with their advantages.

These include cryogenic cooling, low sensitivity, slow detection speeds, and narrow bandwidths. System components in the mmW and THz range include both metal waveguide and optical waveguide components. As the frequency increases above 140 GHz, metal waveguides can not be fabricated with the required precision, causing high losses to the system [30]. Optical waveguides can operate at higher power levels with little loss. Most of the loss in an optical waveguide is from the back reflection from the optical components like lenses. One disadvantage is the added bulk of the optical components. Components such as lenses, polarizers, mirrors, beamsplitters, attenuators, and antennas are not readily available commercially and must be custom built.

Applications in the mmW and THz region are currently limited due to the lack of commercially available sources and components. Some of the potential applications include [29-31] imaging through fog and dust, landmine detection, imaging through walls and soil, concealed weapon detection, wireless communication, medical imaging, earth remote sensing, satellite based astronomy, biological and chemical weapon detection, explosive detection, night vision, and composite inspection.

This dissertation research will focus on millimeter wave imaging in the 90-140 GHz range for the detection of plastic landmines, unexploded ordnance, objects behind barriers, and buried Mars rock along with the development of high reflectivity dielectric THz mirrors for the p-Ge laser and a scanning Fabry-Perot filter which could be used for earth remote sensing and satellite far-infrared astronomy.

CHAPTER 2: FAR-INFRARED AND MMW TRANSMISSION OF SOILS

Introduction

The ability to detect and image buried objects depends on the soil transmission and scattering at a given wavelength. Ground Penetrating Radars operate in the MHz to low GHz range (10's of centimeters to meters wavelength) to maximize penetration through the soil up to tens of feet depending on soil conditions [32]. With an increase of penetration due to longer wavelengths, the ability to detect and resolve the buried objects decreases. Operating at shorter wavelengths will increase the resolution of the system, since the limit of resolution is proportional to wavelength. An investigation of the transmission of soils at frequencies in the mmW and THz regions is needed to determine the shortest wavelength range where the penetration of the soil is still high. Soils with particle sizes larger than the wavelength have low transmittance due to scattering [33]. Reflections occur at the boundaries between the soil particles and air causing the light to scatter. The reflections at the soil particle/air boundaries can be reduced by replacing the air surrounding the soil with an index matching fluid. An index matching fluid with low absorption in the THz/mmW ranges will reduce scattering and increase transmission through the soil. This chapter reports the transmittance of different soils across the THz/mmW range. An increase in transmittance at higher frequencies when the soil is mixed with an index matching liquid is found.

Experimental Methods

Transmission spectra were measured for soils in the 90-4200 GHz range. A Bomem DA8 Fourier Transform Infrared (FTIR) spectrometer equipped with a Hg arc lamp, pellicle beamsplitter, and Infrared Labs Si bolometer (Figure 2) collected transmission spectra from 120 to 4200 GHz. The samples were measured containing 100 scans each with a sample pressure of 0.2 Torr. Immediately after the recording of the sample spectrum, a spectrum of the evacuated sample holder which consisted of 100 scans at 60 GHz resolution was recorded. The transmittance spectrum was obtained from the ratio of the sample spectrum to the evacuated sample holder. The ambient temperature during the scans was 296 K. Measurements were taken in the 120-450 GHz range using a 100 μm mylar beamsplitter at 60 GHz resolution with a 1.8 K Si bolometer. The 300-1500 GHz range was measured at 60 GHz resolution using a 50 μm mylar beamsplitter and a 4 K Si bolometer. Spectra were also collected in the range 1200-4200 GHz using a 12 μm mylar beamsplitter and the 4 K Si bolometer, but the transmission above 1500 GHz was found to be very low for all soil samples studied. The 1 mm high density polyethylene (HDPE) sample cell was placed in front of the off-axis ellipsoidal mirror, whereas the thicker 2.2 cm polystyrene (PS) sample cell was placed after the mirror.

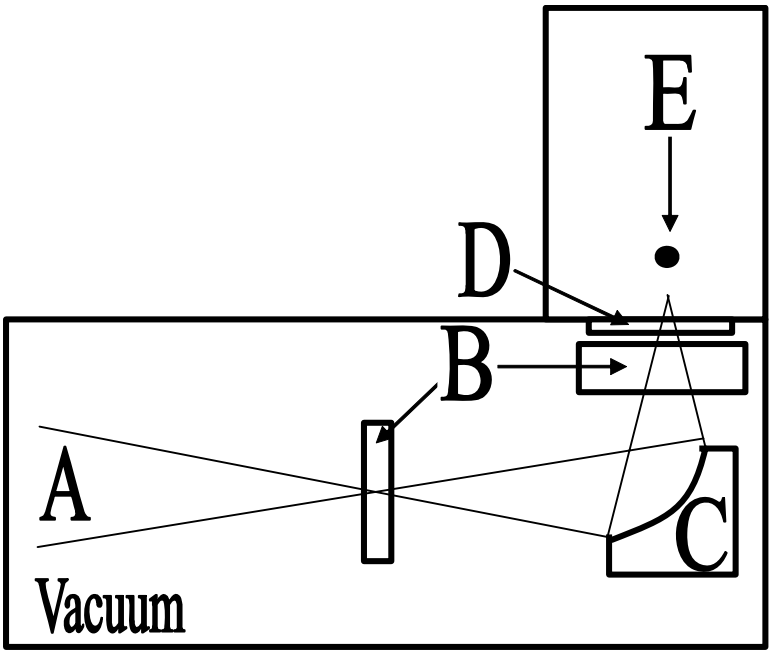

Figure 2: A Fourier transform spectrometer sample compartment with modulated beam (A), sample cell (1 mm or 2.2 cm) (B), off-axis ellipsoidal mirror (C), Polyethylene window (D), and cryogenic Si bolometer (E).

An Anritsu ME7808A vector network analyzer equipped with 16 degree horn antennas (Figure 3) collected transmission spectra from 90-140 GHz at 0.125 GHz resolution. The samples were measured with 100 averaged scans each at atmospheric pressure. Immediately after the recording of the sample spectrum, a spectrum of the empty sample holder was recorded, removing the absorption features due to the sample holder and the atmosphere. The transmittance spectrum was obtained from the ratio of the sample spectrum to the empty sample holder. The radiation is collimated onto the sample using HDPE lenses. This high resolution data was smoothed using adjacent point averaging to reduce oscillations in the baseline due to etalon resonances in the sample cell. The ambient temperature during the scans was 296 K.

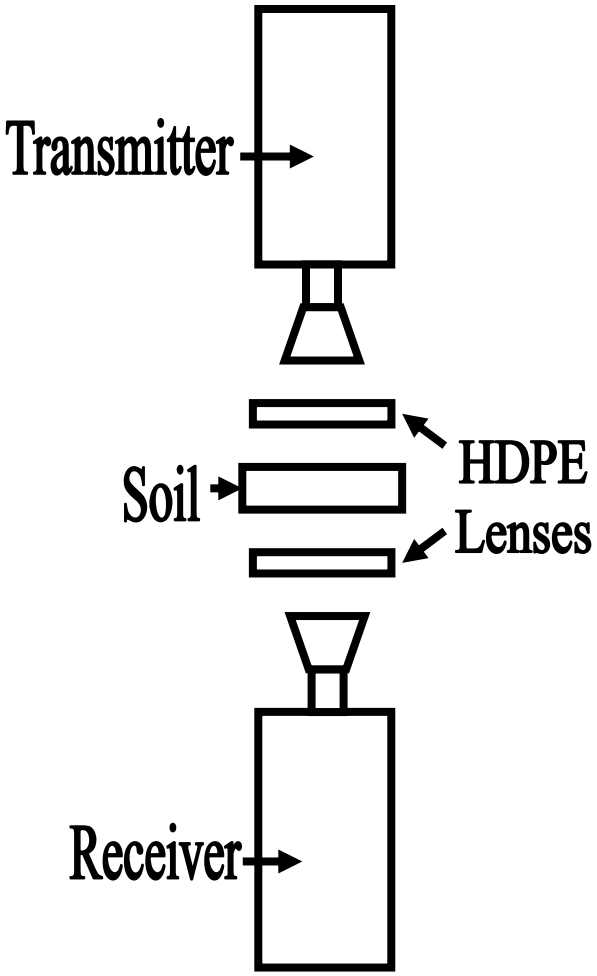

Figure 3: Schematic of the vector network analyzer's transmitter and receiver equipped with horn antennas and HDPE lenses in the transmission configuration.

Two sample cells were used during transmittance measurements. One sample was a HDPE cell that provided 1 mm path length through the soil. The HDPE flanges were wedged to inhibit etalon resonances. The second cell was made of PS with 2.2 cm path length through the soil. The PS sample cell was placed after the mirror to allow the soil to lay flat in the cell. This helped to prevent the soil from settling to the bottom of the holder in the upright position. The air gap created by the settled soil would cause the transmittance to increase giving an incorrect

measurement if the cell was not completely filled. All of the dry soil samples were measured in the PS sample cell, along with all of the VNA measurements. The liquid samples were measured in the FTIR using the wedged HDPE sample cell with the o-ring.

The mmW and far-infrared transmission spectra were collected over the range 90-4200 GHz for 12 soil samples obtained from National Resource Conservation Service (NRCS). These samples include surface and subsurface soil from Wakeland, Doakum, Montevallo, Angola, Minvale, and Sibley. These samples were pulverized with a mortar and pestle and sieved for maximum particle size of 250 μm. The soil samples were maintained in a laboratory environment with ~40% relative humidity.

Geologists recognize 12 distinct soil orders [33]. The NRCS samples belong to six of these. The orders are differentiated by chemical and other characteristics of their horizons. Our "Surface" samples are A-horizon, where much of the original rock structure has been obliterated, where soluble minerals have been leached out, and where humified organic matter has been accumulated. Anti-personnel mines would exclusively be located within A-horizons. Our "Subsurface" samples correspond to upper B-horizon, which occurs below the A-horizon. Though, much of the original rock structure is also obliterated, the B-horizon is compositionally distinct from the A-horizon. Anti-tank mines could conceivably be buried in B-horizon soils.

The "Sibley" samples are Mollisols, which usually have thick dark surface horizons [33]. They are characteristic of steppes, are extensive in sub-humid to semi-arid regions, on plains of North

America, Europe, Asia, South America, most extensively at mid-latitudes. They have enough available moisture to support perennial grasses. The fertile horizon is due to long term addition of organic matter from plant roots. Mollisols are found on ~6.9% of the ice free land on earth and ~21.5% of the U.S. land area.

The "Minvale" samples are representative of the Ultisol order. These soils usually have clay coatings on the surface of granules or pores, or as bridges between sand grains [33]. Ultisols are most extensive in warm humid climates with seasonal precipitation deficit. Utisols are strongly leached, and are often acid forest soils in older stable landscapes. They often have a strong yellow or red color from iron-oxides. Utisols are found on ~8.5% of the ice free land on earth and ~9.2% of the U.S. land area, especially in the southeast region.

The soil samples "Wakeland" are representative of the Entisol order, which is characterized by the absence of distinct subsurface diagnostic horizons within 1 m of the surface [33]. Such soils are found in steep rocky settings. This is the most extensive soil order containing ~16.2% of the ice free land area on earth and ~12.3% of the U.S. land area.

The soil samples "Doakum" are representative of the Aridisol order, which is characteristic of arid climates with little or no leaching [33]. Soluble salts may accumulate in these soils. There is no plant-available water for more than half the time that the temperature is above 5 ºC, when it is warm enough for growth. The soil never has water continuously available for as long as 90 consecutive days when the temperature is above 8 ºC. This soil also contains calcium carbonate

($CaCO_3$). Aridisols are found on ~12.0% of the ice free land on earth and ~8.3% of the U.S. land area.

The "Montevello" samples are representative of the Inceptisol order. These soils have weakly developed subsurface horizons [33]. Inceptisols are found on fairly steep slopes. Inceptisols are found on ~9.8% of the ice free land on earth and ~9.7% of the U.S. land area.

The samples "Angola" are representative of the Alfisol order. These soils are moderately leached with subsurface clay accumulation [33]. Alfisols are found in temperate, humid, and sub-humid regions. Alfisols are found on ~9.7% of the ice free land on earth and ~13.9% of the U.S. land area.

The six remaining soil orders were not studied at this time due to their unusual locations or low abundance on earth. They are Gelisols, Histosols, Spodosols, Andisols, Oxisols, and Vertisols [33]. Gelisols are soils found in very cold climates and contain permafrost within 2 m of the surface. They are found on ~8.6% of the ice free land on earth and ~8.7% of the U.S. land area. Histosols are soils composed of 30-40% organic materials and are only found on ~1.2% of the ice free land on earth and ~1.6% of the U.S. land area. Spodosols are acid soils containing a subsurface accumulation of humus which is complexed with aluminum and iron. They are found on ~2.6% of the ice free land on earth and ~3.5% of the U.S. land area. Andisols are soils formed in volcanic ash and are found on ~0.7% of the ice free land on earth and ~1.7% of the U.S. land area. Oxisols are very highly weathered soils found in intertropical regions. They are

found on ~7.5% of the ice free land on earth and ~0.02% of the U.S. land area, mainly in Hawaii. Vertisols are clay rich soils that shrink and swell with changes in moisture. They are found on ~2.4% of the ice free land on earth and ~2.0% of the U.S. land area.

Millimeter wave and far-infrared transmission spectra were collected (90-4200 GHz) for 6 different soil samples from Night Vision and Electronic Sensors Directorate Mine Lane Facility (NVESD) Fort Belvoir, VA [34] using the FTIR and VNA. These samples contained a wide range of particle sizes, including rocks of up to cm dimensions. Data were collected for these samples in their original mixed state, after sieving for a maximum particle size of 0.5 mm, and of the coarse remainder from the sieving process. Large rocks from the coarse remainder that did not fit in the sample holder were excluded from the measurement to ensure proper filling of the holder.

The six soil samples were obtained from the NVESD were Magnetite (Lane 1), Loam (Lane 2), Crusher Run Gravel (Lane 3), Bank Run Gravel (Lane 4), Virginia Clay (Lane 5), and White Beach Sand (Lane 6). Magnetite is a poorly graded gray sand containing no sizable rocks. It contains 74% Quartz, 20% Magnetite, 4.1% Ilmentite, 1.1% Plagioclase, and 1% total Phyllosilicates [34]. Magnetite has a higher amount of iron oxide (Fe_2O_3) than the other soils. Loam is a low-plasticity brown clay containing some rocks a few mm wide. It contains 89% Quartz, 6.1% total Phyllosilicates, 2.6% K-Feldspar, and 1.2% Plagioclase [34]. Crusher Run Gravel is a brown gravelly silty sand containing many rocks from 0.5 to 4 cm wide. It contains 46% Plagioclase, 22% quartz, 18% total Phyllosilicates, 9.2% K-Feldspar, 2.8% Dolomite, and

1.1% Calcite [34]. Bank Run Gravel is a gravelly low-plasticity reddish brown clay containing many rocks 0.1 to 5 cm wide. It contains 73% Quartz, 16% total Phyllosilicates, 7.2% Goethite, 2.7% K-Feldspar, and 1.5% Plagioclase [34]. Virginia Clay is a reddish brown gravelly silty sand containing many rocks 0.1 to 2.5 cm wide. It contains 89% Quartz, 8.4% total Phyllosilicates, 1.9% K-Feldspar, and 0.5% Plagioclase [34]. White Beach Sand is a light gray poorly graded sand containing small traces of rocks a few mm wide. It contains 98% Quartz and 1.8% total Phyllosilicates [34].

Transmission spectra were collected for some organic materials using the vector network analyzer in the range 90-140 GHz. Materials studied include wet and dry sod, organic debris (leaves, roots, sticks, etc) and water. One sample was sourced locally from Orlando, FL. Florida sand is mostly composed of quartz and is free from rocks or debris and has uniform particle sizes of ~250 μm. Transmission spectra were taken for the Florida sand from 90-140 GHz using the VNA and from 120-1500 GHz using the FTIR. Due to the high scattering loss of soil at high frequencies, various liquids were tested to determine potential candidates for index matching liquids to fill in the air gaps around the soil producing higher transmission. The liquids measured were WD-40, Nujol mineral oil, vegetable oil, extra virgin olive oil, canola oil, Fluorolube, and silicone oil for these index matching experiments from 90-600 GHz - using the VNA from 90-140 GHz and the FTIR from 120-600 GHz. The FL sand soil samples were fully saturated with the index matching liquids and placed into the sample cells. Transmission spectra were taken for these index matching liquids mixed with the Florida sand from 90-600 GHz using the VNA and FTIR systems.

Transmission Results

Transmittance spectra of the 12 NRCS soil samples for the range 90-1500 GHz are shown in Figure 4 & Figure 5. Each soil sample was measured from 90-140 GHz with the VNA and from 120-1500 GHz with the FTIR. The transmittance spectra from the VNA and FTIR systems were combined together to show the full 90-1500 GHz range with an overlap from 120-140 GHz. The absolute transmittance levels measured by the two instruments generally agree within 7.5% in this overlap range. The high frequency range is dominated by a roll-off due to scattering. The characteristic cutoff wavelength is similar to the characteristic particle size, as determined using an optical microscope. For instance, the surface samples of Figure 4 tend to zero transmittance for frequencies in the range 900-1200 GHz, which corresponds to wavelengths in the range 333-250 μm. This correlates well with the 250 μm maximum particle size obtained by sieving. Soil transmittance is seen to increase at lower frequencies because decreased scattering allows more signal to be collected by the bolometer (Figure 2). This occurs when the wavelength is longer than the particle size. At the low frequency end of the measured band (90 GHz), the transmittance ranges from 0.2 to 0.9.

The subsurface specimens tend to have a lower cutoff frequency and smaller transmittance than the corresponding surface samples. This may be due to small differences in the particle size distribution but it may also be due to the difference in chemical composition. We note that [35] near surface soils tend to be leached of soluble or quickly altered minerals. Surface soils are rich

in insoluble quartz, clay minerals, and iron oxide alteration products, but they still are poor in calcium carbonate.

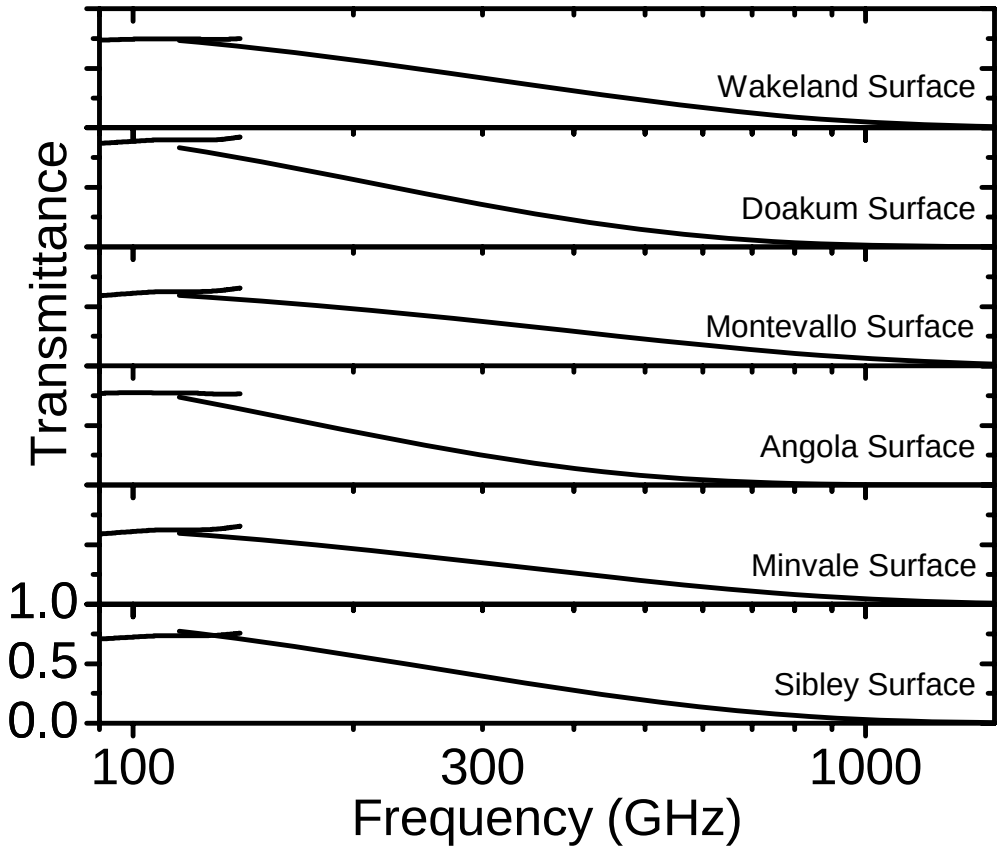

Figure 4: Transmittance spectra for 1 mm thick surface soil samples using a VNA from 90-140 GHz and a FTIR from 120-1500GHz.

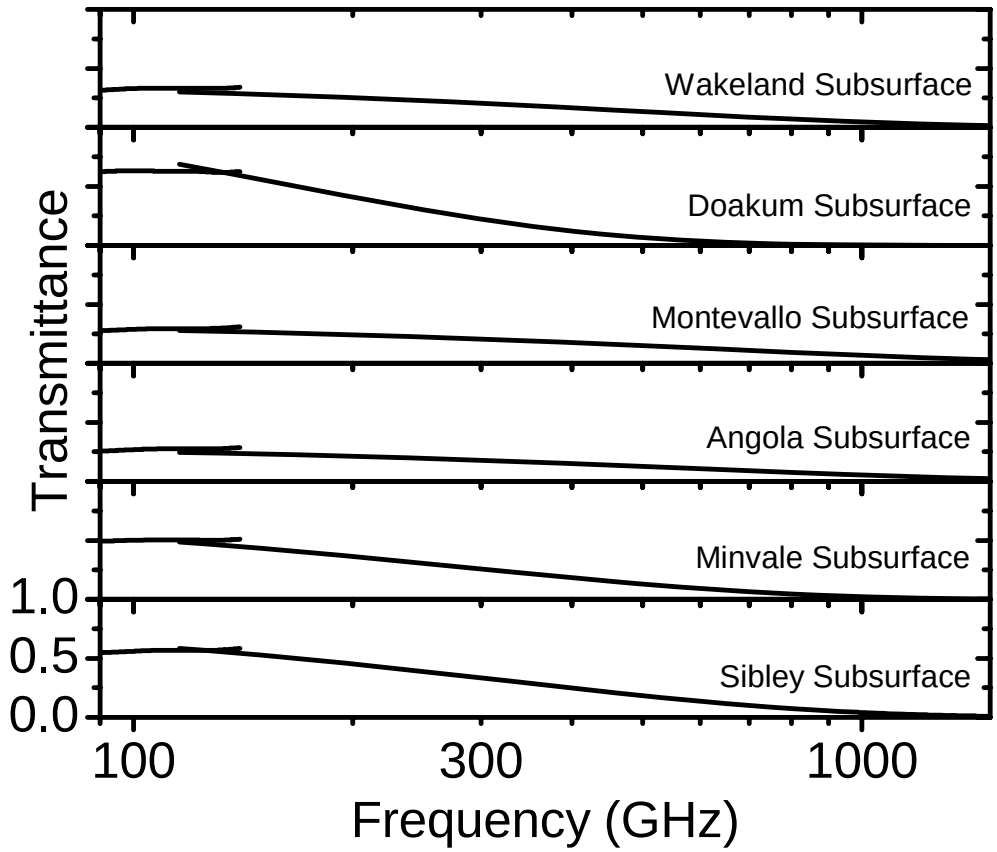

Figure 5: Transmittance spectra for 1 mm thick subsurface soil samples using a VNA from 90-140 GHz and a FTIR from 120-1500GHz.

Transmittance spectra in the 90-140 GHz range for NVESD samples Loam, Virginia Clay, Bank Run Gravel, Crusher Run Gravel, are presented in Figure 6 through Figure 9 respectively. The sieved samples all have transmittance in the range 30% to 60%, which is higher than the non-sieved samples by ~1-2 orders of magnitude. The coarse after-sieving remainder has transmittance even lower, by at least an order of magnitude. These results show that large particle sizes in the range 0.5 mm to ~cm cause strong scattering of millimeter waves (2-3 mm

wavelength). This observation is in agreement with that already made for the NRCS samples, namely that transmittance is high when the wavelength exceeds the soil particle size.

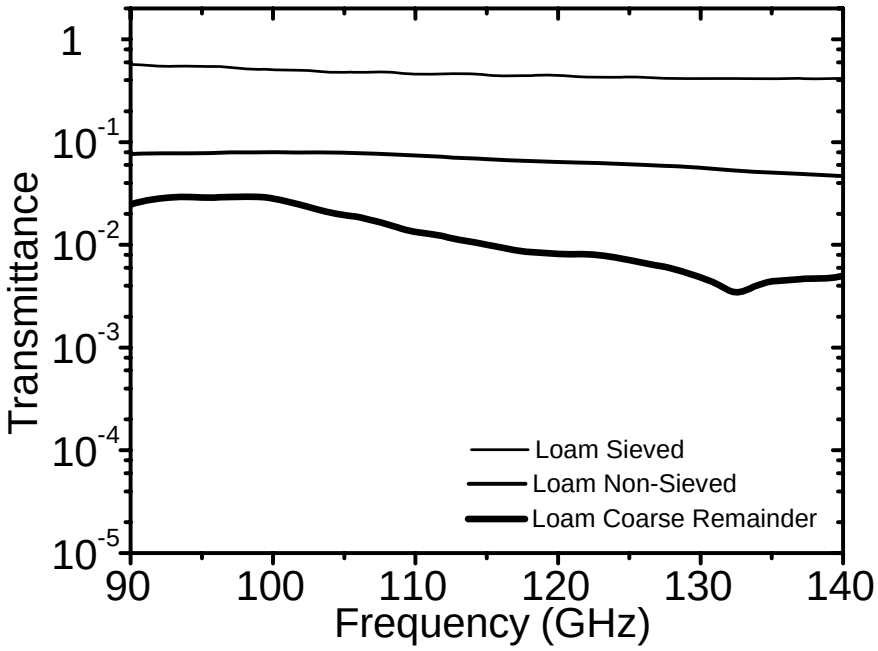

Figure 6: Transmittance spectra for 2.2 cm thick Loam soil samples.

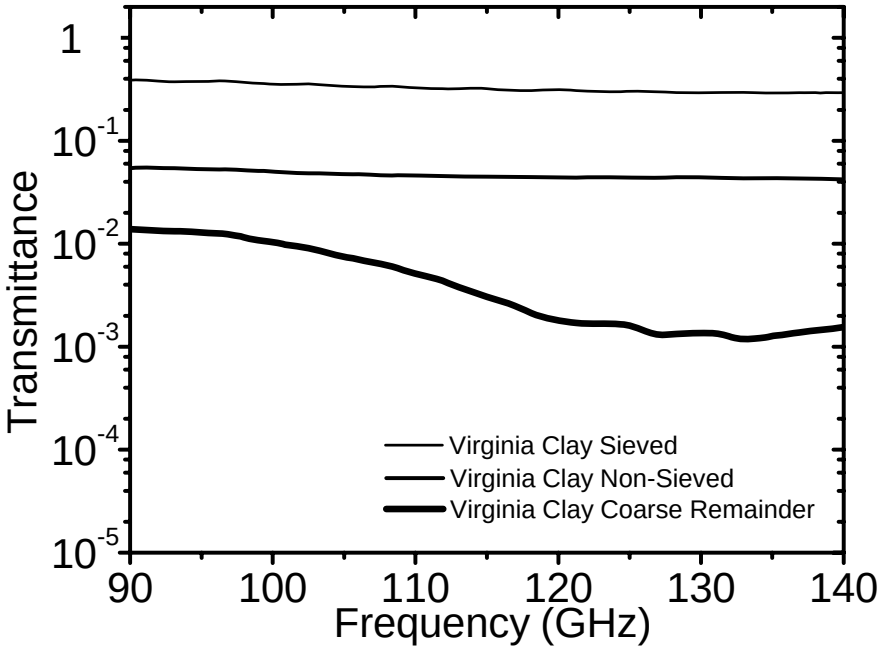

Figure 7: Transmittance spectra for 2.2 cm thick Virginia Clay soil samples.

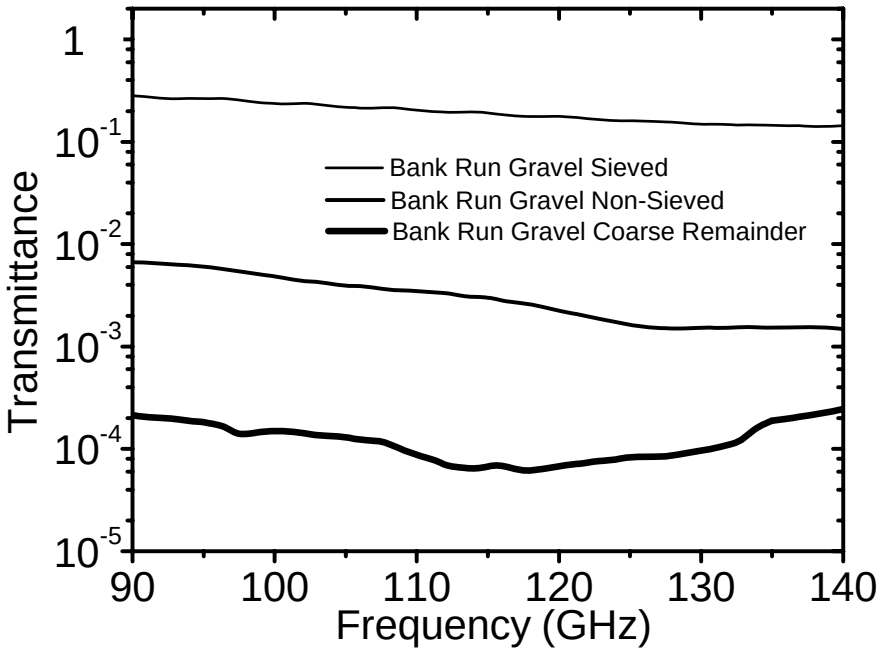

Figure 8: Transmittance spectra for 2.2 cm thick Bank Run Gravel soil samples.

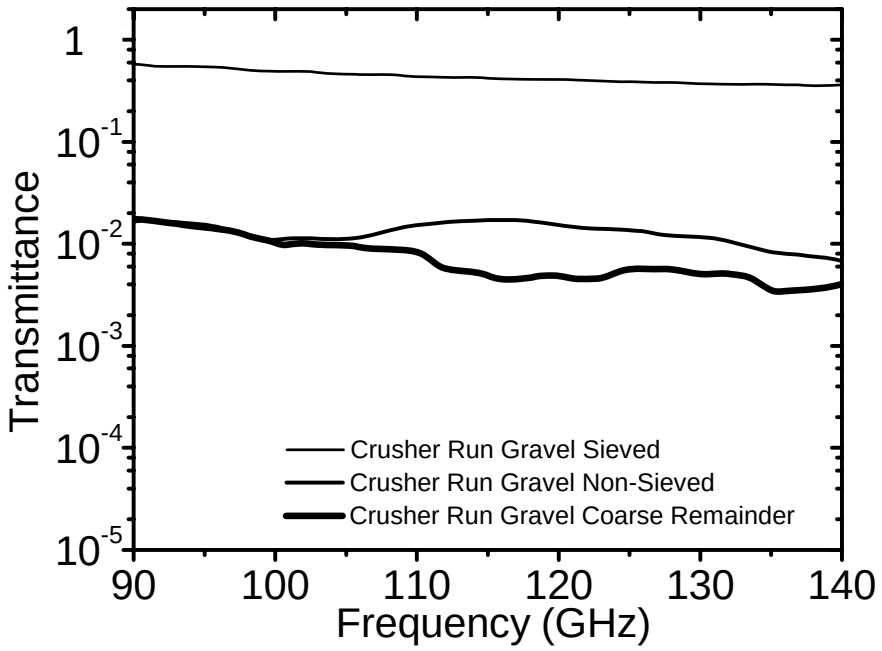

Figure 9: Transmittance spectra for 2.2 cm thick Crusher Run Gravel soil samples.

Figure 10 presents spectra of the White Beach Sand sample. Sand tends naturally to have a uniform particle size distribution. When isolated, the coarse remainder from the sample has transmittance of 45-65%; however the abundance of coarse material in the non-sieved sample is insufficient to lower that samples transmittance much below 90%. We note that the 2-3 mm wavelengths are significantly greater than the particle size in this case, in agreement with our previous observations.

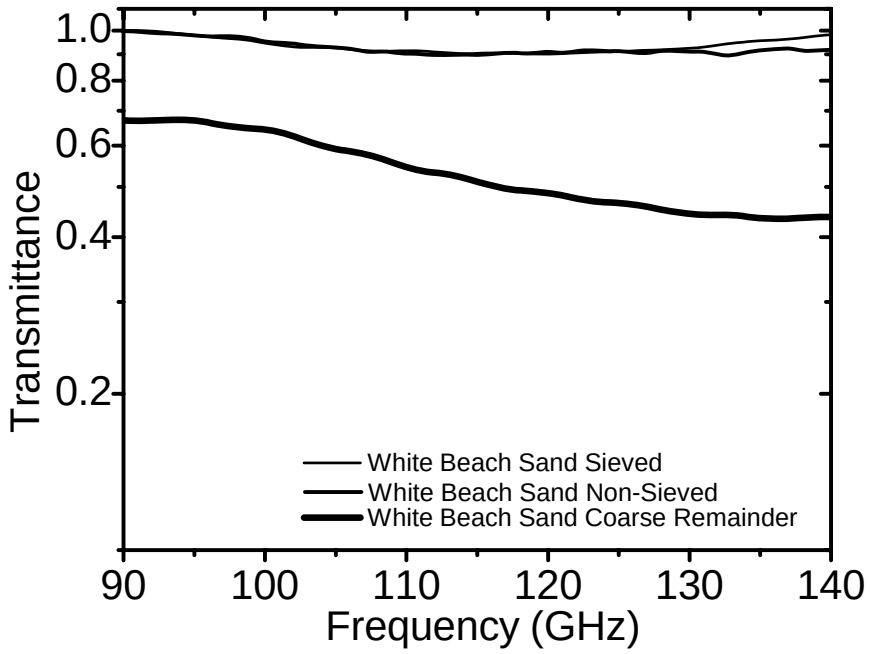

Figure 10: Transmittance spectra for 2.2 cm thick White Beach Sand soil samples.

Figure 11 presents mmW spectra for the magnetite sample. The results here do not follow the trend of transmittance vs. particle size noted earlier. Non-sieved, sieved, and coarse remainder all have transmittance below 0.01%. The latter two segregated samples both have higher transmittance than the non-sieved sample. The magnetite sample morphology was very different from that of the other NVESD samples. It contained a light colored sandy component of uniform sub-mm size distribution and a dark magnetic component that tended to stick together in clumps. The non-sieved sample contained few large particles; the fraction that passed through the mesh openings during sieving contained both the light and dark components.

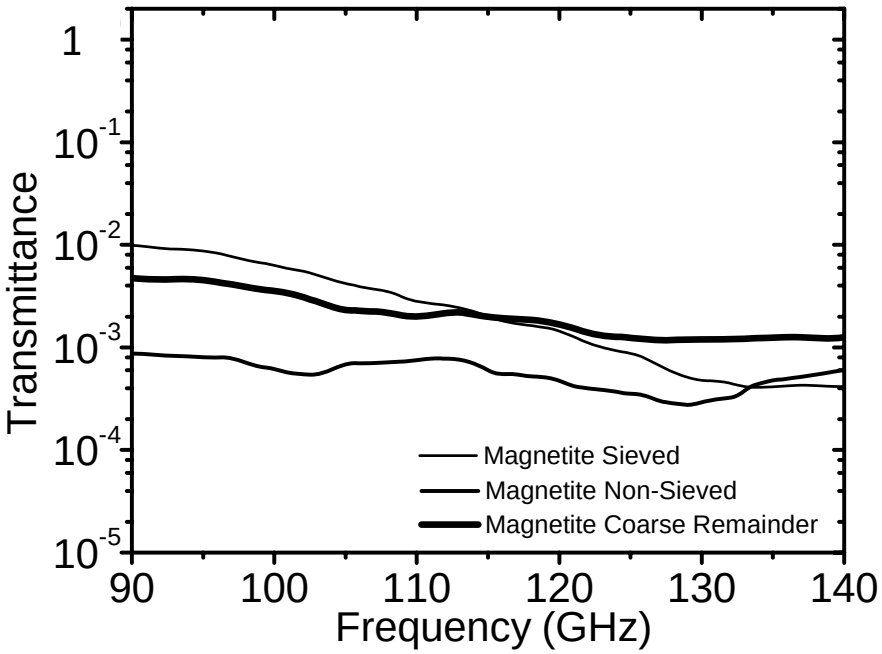

Figure 11: Transmittance spectra for 2.2 cm thick Magnetite soil samples.

The transmittance of some organic materials in the 90-140 GHz frequency range is presented in Figure 12. Organic matter is a strong source of attenuation possibly because of effective scattering by relatively large particle sizes. A spectrum of water is also presented in Figure 12, and water is found to be a strong attenuator, which explains the relative transmittance of dry and wet sod samples. The dry sod has a slightly higher transmittance than the wet sod. Note that both wet and dry sod samples have lower transmittance than plain water, so that scattering by inhomogenities in the organic samples is apparently more important than absorption by moisture.

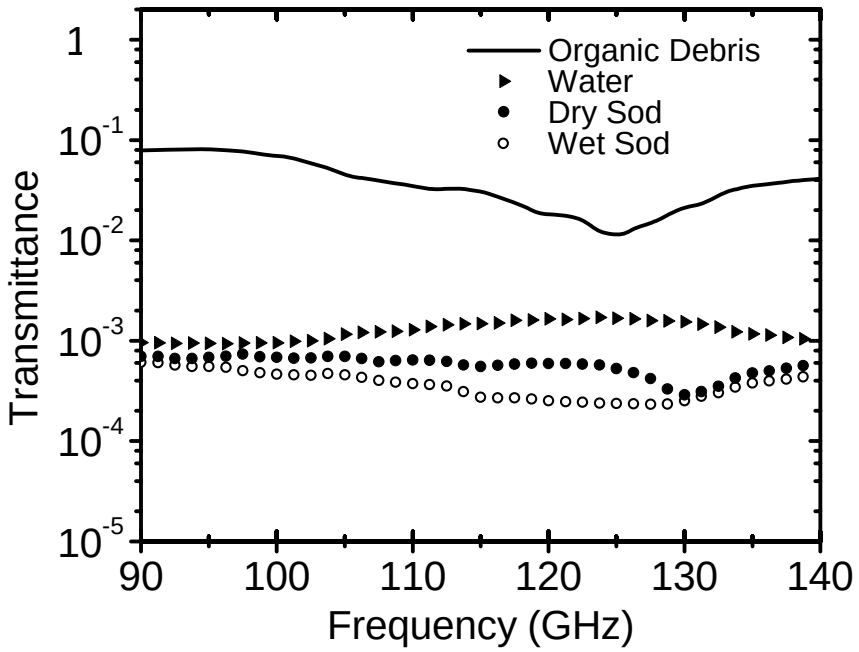

Figure 12: Transmittance spectra for 2.2 cm thick organic samples.

Transmittance spectra of the Florida sand sample for the range 90-1500 GHz is shown in Figure 13. The transmittance spectra from the VNA and FTIR systems were combined together to show the full 90-1500 GHz range with an overlap from 120-140 GHz. The high frequency range is dominated by a roll-off due to scattering. The characteristic cutoff wavelength is similar to the characteristic particle size, as determined using an optical microscope. For instance, the soil sample tends to zero transmittance for frequencies in the range 1000-1500 GHz, which corresponds to wavelengths in the range 300-200 μm. This correlates well with the 250 μm particle size measured using an optical microscope.

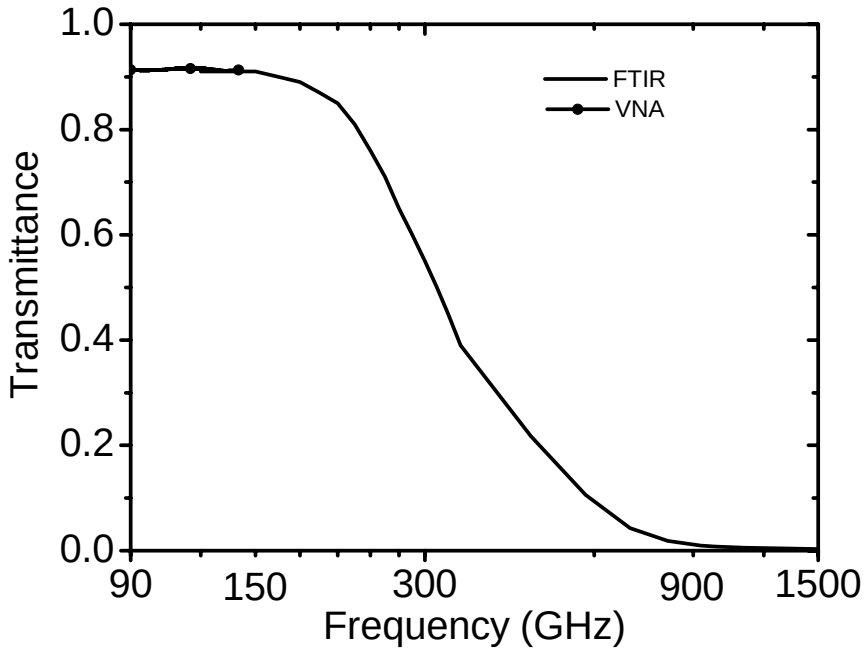

Figure 13: Transmittance spectrum of 3 mm of FL Sand using a VNA from 90-140 GHz and a FTIR from 120-1500 GHz.

Index Matching Liquids

Transmittance spectra of some liquid samples over the range 90-600 GHz is shown in Figure 14. The transmittance spectra from the VNA and FTIR systems were combined together to show the full 90-600 GHz range with an overlap from 120-140 GHz. The maximum transmittances of the potential index matching liquids have a range from 0.75 to almost 1. The path length through the sample is 1 mm. Some of the liquids have good transmittance and hence are potential candidates for index matching.

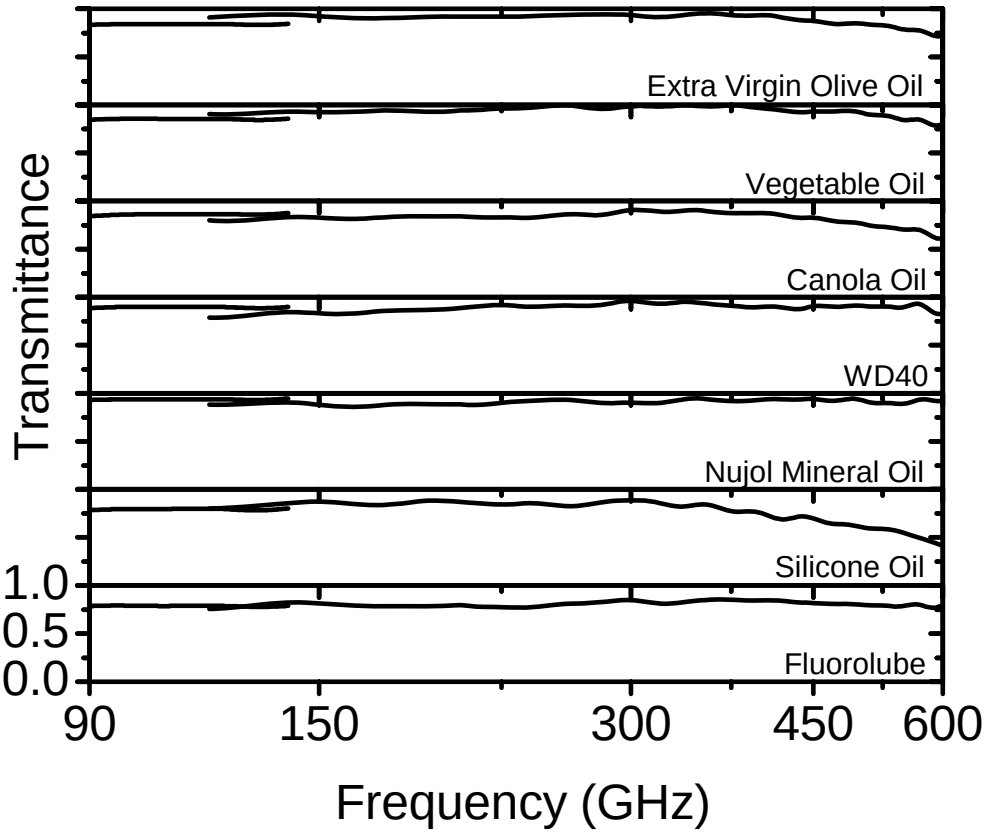

Figure 14: Transmittance spectra of 1 mm path length of potential index matching liquids in the 90-140 GHz range using a VNA and in the 120-600 GHz range using a FTIR.

Several of the liquids were used to saturate one of the soil samples (Florida Sand) for the purpose of index matching. Figure 15 shows the transmittance spectra from 90-600 GHz of the saturated soil compared to the transmittance of the dry soil (gray curve). The transmittance spectra from the VNA and FTIR systems were combined together to show the full 90-600 GHz range with an overlap from 120-140 GHz. The Fluorolube sample was not used for index matching due to the high viscosity of the liquid and its inability to seep into the soil.

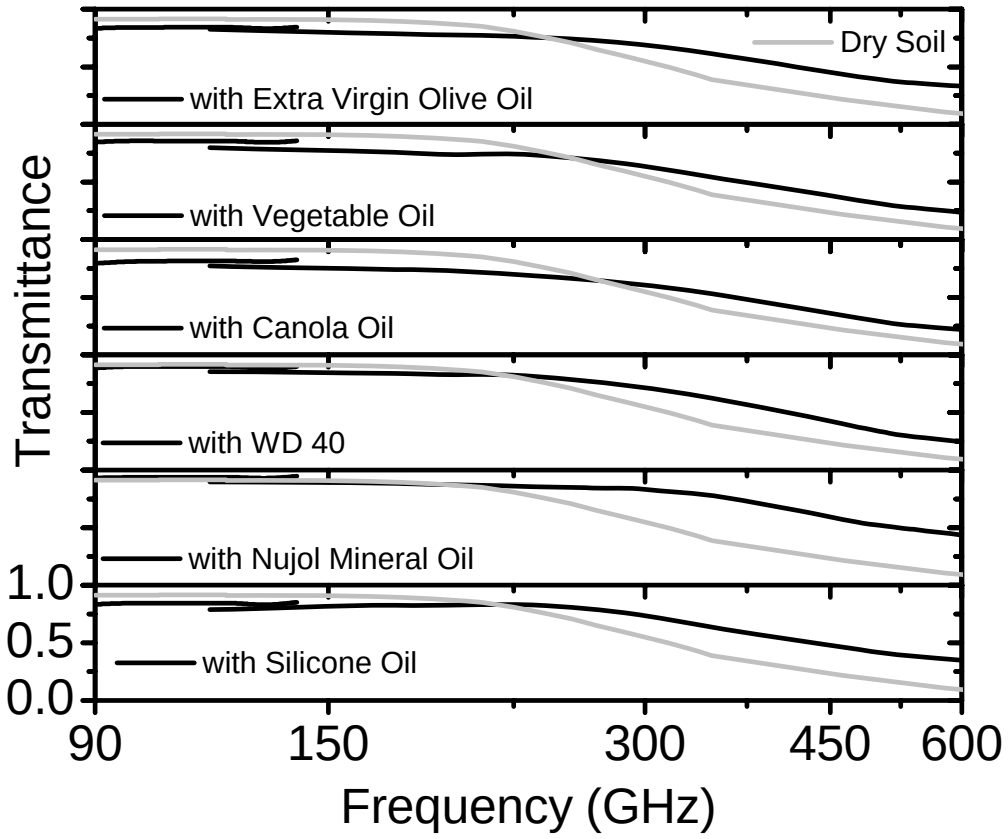

Figure 15: Transmittance spectra of 1 mm path length of several index matching liquids mixed with the FL sand soil sample in the 90-140 GHz range using the VNA and in the 120-600 GHz range using the FTIR.

At high frequencies, the addition of index matching fluid reduces scattering and increases transmission. Even though index matching has increased transmission, there is still a roll-off at high frequency. This is because the liquids studied are not exact matches to the index of the particles (n_{quartz} ~ 2.113 [36] and n_{oil} ~ 1.4679 [37] at 900 GHz). Proper index matching could potentially push the roll-off frequency higher, extending the useful transmission range further into THz, but many of the liquids available that could provide a perfect index match are highly toxic and would not be safe to mix with the soil.

Soil Scattering

Theory

As the electromagnetic radiation travels through the soil, energy is transmitted, absorbed, and scattered. To quantify the attenuation due to scattering [38], a basic approach is taken. The incident signal with power per unit area encounters a volume of scatterers characterized by a radius, a, and a number per unit volume, N_s. The incident power, P_I will come across $N_s\ dL$ scatterers per unit area over a path length dL. The transmitted power is defined as,

$$P = P_I - dP \tag{1}$$

where dP is the power lost per unit area by the scatters in the path length dL. The soil particles are assumed to be spherical and having a scattering cross sectional area, A_s. The scattered power is expressed as

$$dP = N_s \cdot A_s \cdot P_I \cdot dL \tag{2}$$

which means the power will decline exponentially as the length through the material increases. Giving the differential equation

$$\frac{dP}{P} = d\ln P = -N_s \cdot A_s \cdot dL \tag{3}$$

with the solution

$$P = P_I \cdot e^{-N_s \cdot A_s \cdot L} = P_I \cdot e^{-\alpha_{sct} \cdot L} \tag{4}$$

where α_{sct} is the power scattering attenuation coefficient.

The cross sectional area using the Rayleigh approximation [39] is given as

$$A_s = \frac{8\pi}{3}\left(\frac{2\pi m_{med}\nu}{c}\right)^4 a^6\left(\frac{m_s^2-1}{m_s^2+2}\right)^2 \tag{5}$$

where ν is the frequency, c is the speed of light, a is the particle radius, and $m_s=n_{sph}/n_{med}$ is the ratio of the refractive index of the spherical particle (n_{sph}) to that of the surrounding medium (n_{med}). The values for the number of particles per unit volume and particle size were determined by fitting the experimental data to the model using N_s and a as variables. An initial guess is calculated to facilitate a practical fit. An estimate for the number of particles per unit volume is determined using density packing values from sphere packing. The highest density, the ratio of the volume of all of the spheres to the volume of the container, that can be achieved is 0.7405 using hexagonal close packing [40]. However, soil particles poured into a sample holder would probably have a packing density close to the tetrahedral lattice (0.3401) [40]. The number of particles per unit volume is determined as

$$N_s = \frac{\rho}{V_{sph}} \tag{6}$$

where ρ is the packing density and V_{sph} is the volume of the sphere. The estimated radius of the soil is determined using an optical microscope.

The total attenuation from the soil is a combination of the scattering attenuation α_{sct} plus the material absorption loss α_{abs}.

$$\alpha_{total} = \alpha_{sct} + \alpha_{abs} \tag{7}$$

Therefore, the total transmitted power is given as

$$P = P_I \cdot e^{-\alpha_{total} \cdot L} \tag{8}$$

Results

The theoretical model was applied to the Florida sand sample measured in Figure 13. The Florida sand sample consists mostly of quartz, which has an index of 2.113 and an absorption coefficient of 0.3 cm^{-1} at 900 GHz [36]. The initial value set for the particle sizes ($2a$) are roughly 250 μm as measured by an optical microscope. The path length (L) was 3 mm. A tetrahedral lattice packing density (ρ) was assumed of 0.3401 giving an initial N_s value of 4.15×10^{10} m^{-3}. The model was then fit to the measured data varying N_s and a. The results of the theoretical model compared to the measured data are shown in Figure 16.

The theoretical data shows good agreement to the measured data. The fit gives the radius value as 143 μm and the number of particles per unit volume as 4.305×10^9 m^{-3}, which are within the acceptable ranges. The model gives an R-squared value of 0.9898 to the experimental data. R-squared is the proportion of explained variation, measured between 0 and 1. The closer R-squared is to one, the greater the ability of the model to predict the experimental value. The low frequency portion of the curve (90-150 GHz) coincides well with the attenuation due to absorption. As the frequency increases, the attenuation due to scattering increases and the transmittance starts to decrease. The theoretical roll-off due to scattering has the same trend as the measured data, but the tail end of the roll-off has a slightly different slope. This could be due

to two factors. First, our theoretical model assumes spherical grains of sand composed of quartz. However, the grains of sand are not entirely spherical. Second, the actual soil also contains other small organic material of a different index of refraction along with the quartz sand. These factors will change the transmittance slightly. Regardless, the close agreement of our model to the experimental data shows that the high frequency losses are due to scattering from the soil grains.

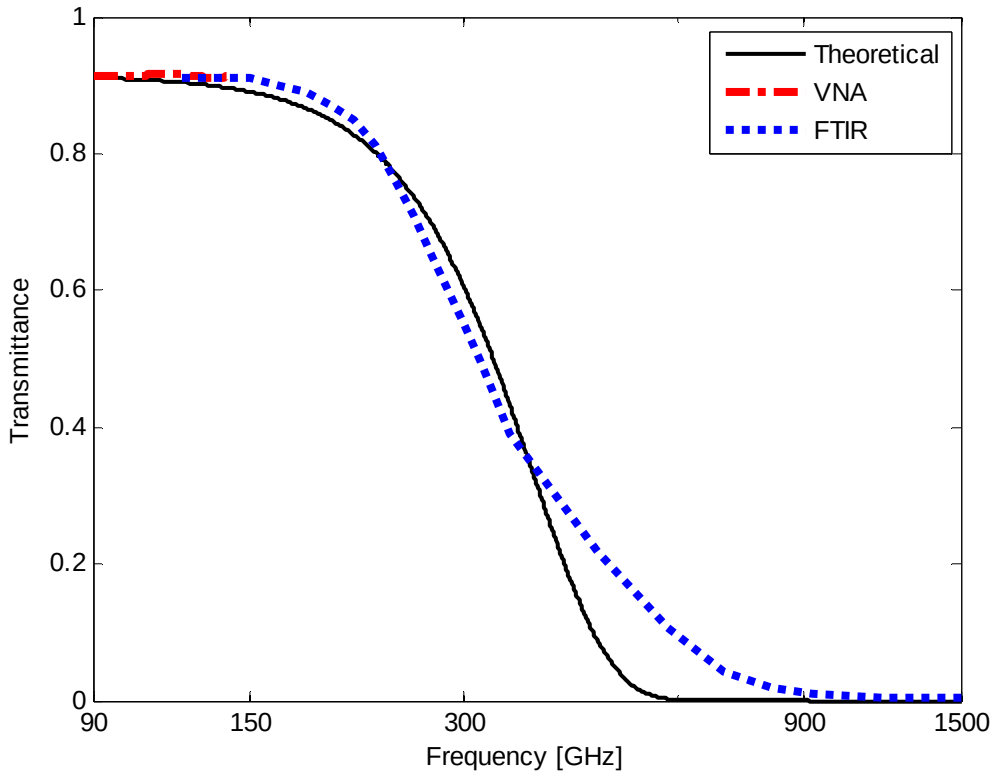

Figure 16: Theoretical and measured transmittance of 3 mm of FL Sand

The theoretical model can also be applied to the index matching liquids data by changing the n_{med} to the index of refraction of the liquid used. An absorption coefficient for the liquid is also

added to the model. The absorption coefficient α_{liq} is determined using the transmittance, T_s, and path length, L, data for the liquid by

$$\alpha_{liq} = \frac{-\ln(T_s)}{L}. \tag{9}$$

The results of the theoretical model of the Florida sand mixed with olive oil are shown in Figure 17. The model and the experimental data are in good agreement. The fit gives the radius value as 135 μm and the number of particles per unit volume as 5.505×10^9 m^{-3}, which are again within the acceptable ranges. The model gives an R-squared value of 0.9367 to the experimental data. The roll-off due to scattering occurs in the model at a similar frequency to the experimental data. The index matching of the soil does increase the transmittance at higher frequencies.

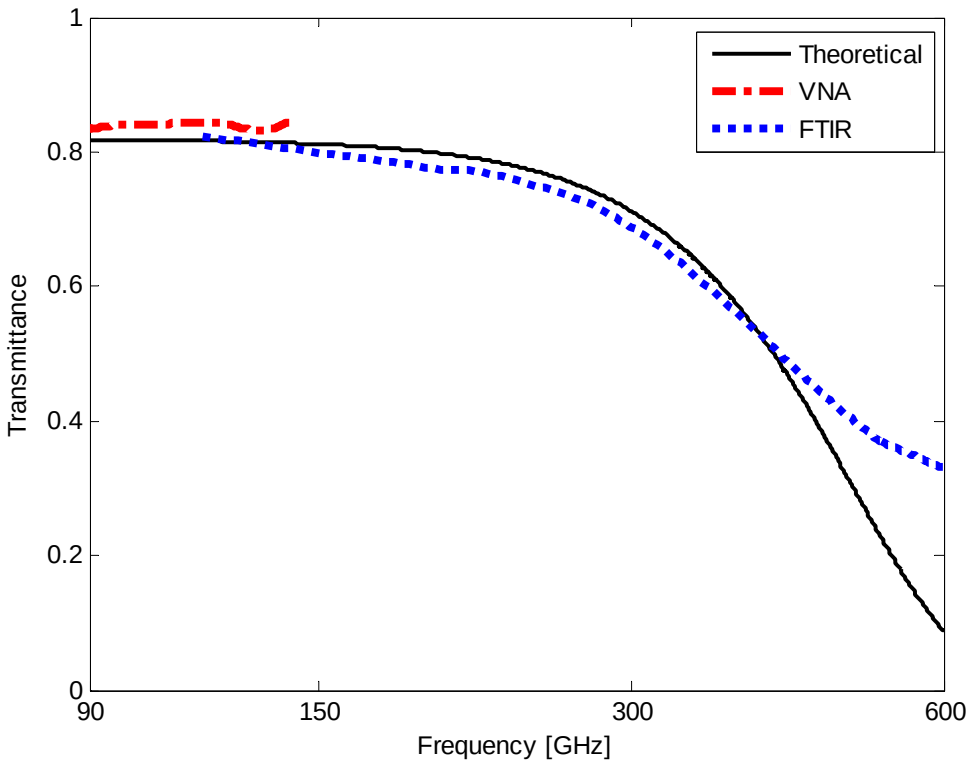

Figure 17: Theoretical and measured transmittance for Florida sand index matched with olive oil.

The use of higher index matching liquids can increase the transmittance through the soil to 1 THz. Figure 18 shows the theoretical transmittance through the soil as the index of refraction of the liquid increases from 1.4 to 2.2 with similar absorption to olive oil. The 50% transmission level changes from 315 GHz for dry sand to 1000 GHz for sand mixed with index matching liquid with an index of 2.2. The increase in transmittance at the higher frequencies due to the index matching liquids would allow for higher resolution images to be taken without the loss of penetration depth.

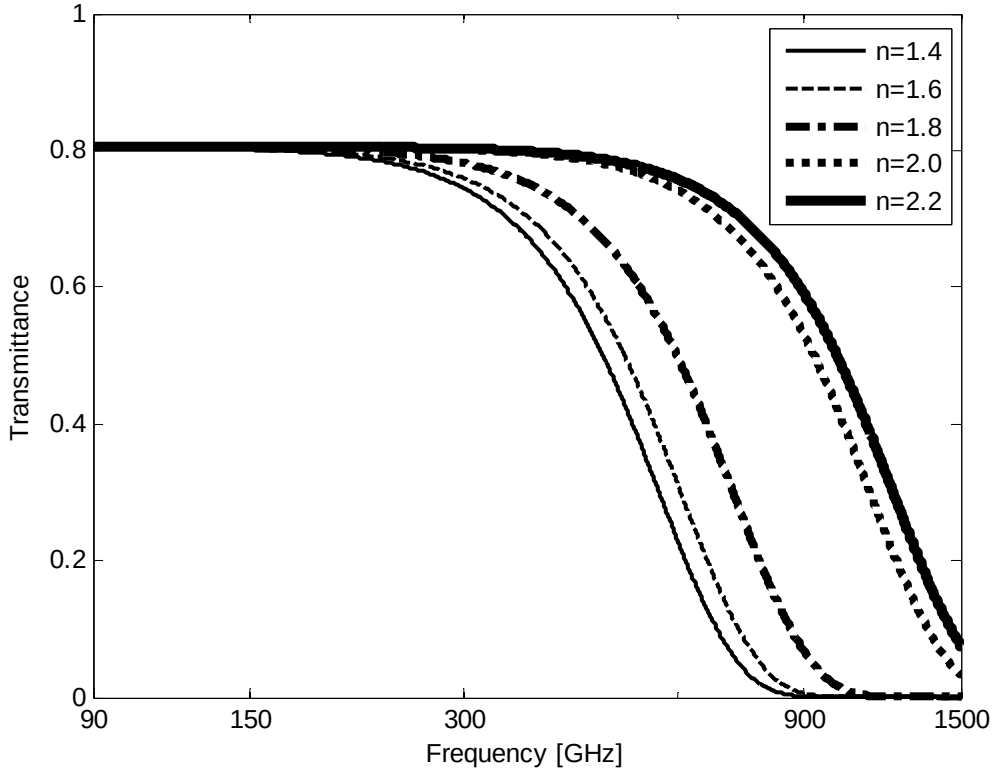

Figure 18: Theoretical transmittance of Florida sand mixed with index matching liquids from 1.4 to 2.2.

CHAPTER 3: MMW IMAGING SYSTEM FOR LANDMINE DETECTION

Introduction

Landmines inflict high costs on civilian populations decades after the military conflicts that prompted their deployment have ceased. The United Nations estimates that over 110 million active mines lie hidden beneath the ground of sixty-eight countries, killing or maiming 2000 people per month. Accidents occur on a rate of one for every 1000 to 2000 mines destroyed [41]. The threat to civilians remains and hinders economic and social recovery.

Anti-personnel mines can be buried just beneath the surface, whereas anti-tank mines are buried as deep as 40 cm. The landmines can be any shape and be made of many different materials including metal, plastic, rubber, or wood. There are a number of detection technologies applied for the remediation of minefields, such as inductance coils (metal detectors), magnetometers, ground-penetrating radar, infrared imaging, and explosives vapor sensors [42]. Metallic mines can be detected using many of the methods mentioned above. However, the increased use of plastic mines has made detection difficult. Inductance coils and magnetometers cannot detect mines with little or no metal content [43]. Ground-penetrating radar systems operate at long wavelengths [43] which give them high penetration through the soil but low spatial resolution increasing the false alarm rate compared to the mmW wavelengths. Thermal infrared imaging detection methods require multiple images to be taken 30 minutes apart to detect the landmines [44]. Explosive vapor sensors often provide poor localization capabilities and spatial resolution

[43]. A passive mmW landmine detection system has been demonstrated before [45], but depends on the effective sky temperature. An active mmW system [46] is potentially attractive in that, in an imaging mode, it can achieve good discrimination between anti-personnel mines that are primarily non-metallic, and the small metallic debris (shrapnel, cartridge cases, etc.) typical of minefield conditions.

Because of the shape and size discrimination inherent in an imaging system, the tradeoff between false alarm rate and miss rate is favorable for mmW wavelengths [45]. Ability to detect and image buried objects will depend on soil transmission and scattering. The previous chapter demonstrates that soils with particle sizes larger than the wavelength have low transmittance due to scattering [47]. Dry quartz sand has high transmission in the mmW range due to its fairly uniform particle size, which is smaller than the wavelength of light [47].

A hyperspectral 90-140 GHz mmW imaging system used to locate and identify landmines and other objects buried beneath sand of various depths and conditions is demonstrated. The information provided by the hyperspectral images is analyzed through a Principal Component Analysis (PCA) method. With this signal processing, valuable information is condensed into single images and the buried objects can be located and identified. The PCA method has been used before as a landmine detection signal processing technique in other wavelength regions improving the detection and classification rates while lowering the false-alarm rate [48-50]. We present the experimental set up for the 90-140 GHz mmW imaging system in this chapter.

Experimental Methods

An imaging system was developed for the mmW range using an Anritsu vector network analyzer (VNA) operating from 90-140 GHz. The VNA modules, equipped with 16 degree horn antennas, were mounted on a vertically oriented optical table, shown in Figure 19. The mmW radiation was focused using a HDPE lens onto the sample and then reflected back through another HDPE lens into the VNA receiver. Two motorized translation stages, with 200 mm maximum travel distance and 50 mm/s maximum velocity were mounted perpendicular to each other. The sample was attached to the stages using a long aluminum arm with the inset removed preventing the sample from being held over the highly reflective metal stages. The landmine was placed in a 20.3 cm × 20.3 cm × 9.5 cm container surrounded by soil. This container allows the landmine to be buried up to 5 cm deep and be placed anywhere within the 412 cm^2. A broadband convoluted foam millimeter wave absorber, ECCOSORB CV, was placed under the sample to eliminate back reflections from the optical table. A program was written in LABVIEW to capture a raster scan image (Figure 19 inset), containing 29 lines, of the landmine under the soil. At each position of the scan, the VNA measured the reflection from the landmine, from 90-140 GHz in 1 GHz steps.

The resulting data set is converted into a set of images (one for each mmW frequency used) by a MATLAB software program. In our case, the total number of frequencies is 51. The size of the images depends on the number of points taken in each scan and the distance between them. These sizes can be changed with the LABVIEW program.

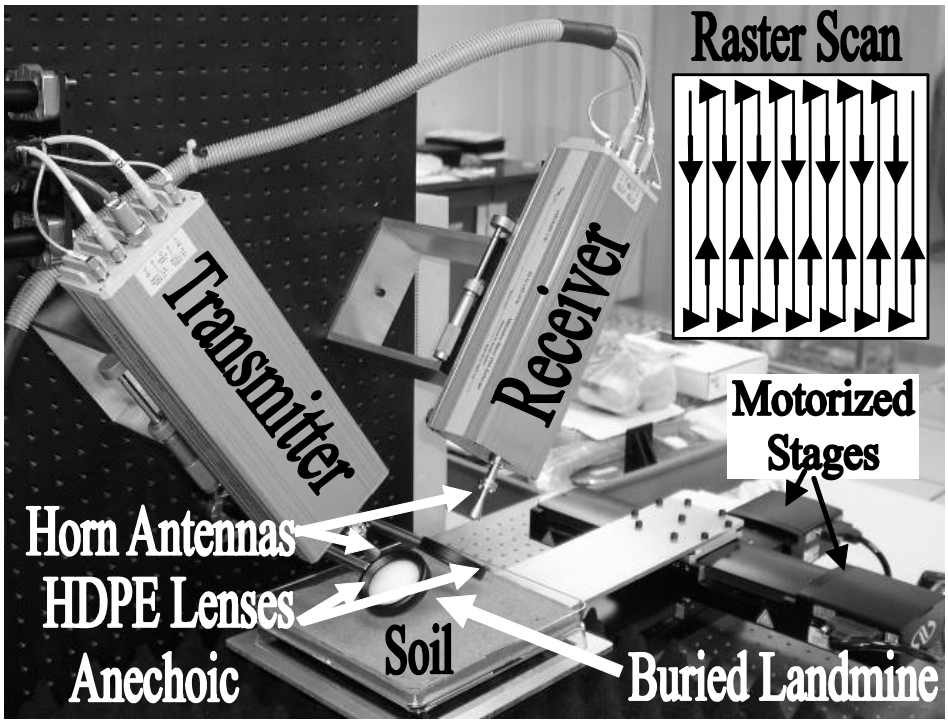

Figure 19: Photograph of the active hyperspectral mmW imaging system. (Inset) Schematic of the path for taking a raster scan image. The radiation coming from the transmitter, 90-140 GHz, is focused onto the sample using the HDPE lens and scattering radiation from the object is collected and focused on the receiver at each pixel of the raster scan.

Estimates of the size of the aberration blur produced by the mmW imaging system were determined and compared to the diffraction limited blur. The diffraction limited blur [51], β_{diff}, for the system is

$$\beta_{diff} = \frac{2.44\lambda}{D} radians \tag{10}$$

where λ is the wavelength and D is the diameter of the lens.

An estimate of the spherical aberration blur, β_{sph}, sagittal coma blur, β_{coma}, and astigmatism blur, β_{ast}, are [51]

$$\beta_{sph} = \frac{k}{(f/\#)^3} radians \tag{11}$$

$$\beta_{coma} = \frac{\theta}{16(n+2)(f/\#)^2} radians \tag{12}$$

$$\beta_{ast} = \frac{\theta^2}{2(f/\#)} radians \tag{13}$$

where k is 0.067 for the index of refraction, n, of the lens (n~1.5), $f/\# = f/D$, f is the focal length, and θ is the half field angle in radians.

The mmW imaging system can be equipped with a 60 mm, 100 mm, or 139.7 mm focal length lens, all with a diameter of 50.8 mm. For all three lenses, β_{diff} is 0.13 rad at the center wavelength of the system. The aberration blur for each lens is smaller than the diffraction blur. For f=60 mm, β_{sph}=0.04 rad, β_{coma}=0.005 rad, and β_{ast}=0.08 rad. For the f=100 mm lens, β_{sph}=0.009 rad, β_{coma}=0.001 rad, and β_{ast}=0.016 rad. For the f=139.7 mm lens, β_{sph}=0.003 rad, β_{coma}=0.0004 rad, and β_{ast}=0.006 rad. Therefore, the mmW imaging system is diffraction limited.

The objects imaged beneath the soil were two landmines and other minefield debris. The two landmines were the TS-50 (Figure 20 top left) and the M14 (Figure 20 bottom left). They are typically scatter laid by a helicopter or buried to a depth of 30 mm [52]. The TS-50 is a circular

plastic bodied mine with strengthening ribs. The TS-50 has a height of 45 mm, a diameter of 90 mm, and weighs 186 g. It contains a round metallic pressure plate on top of the mine. The TS-50 contains 50 g of T4 explosive and is waterproof and non-buoyant [52]. The TS-50 cannot be located using metal detectors under most field conditions and are highly resistant to blast overpressure clearance methods. The M14 landmine is a cylindrical bodied plastic mine with very low metal content. The M14 has a height of 40 mm, a diameter of 56 mm, and weighs 90 g. The M14 contains 29 g of Tetryl explosive [52]. The M14 is very difficult to locate using metal detectors under most field conditions and can be defeated using blast overpressure methods. The minefield debris consisted of a 20 mm OICW practice round, a 20 mm round from WWII, a 7.62 mm cartridge case, a 5.56 mm rose crimp cartridge case, a 5.56 mm standard cartridge case, and a fuse lighter with a metal key ring (Figure 20 right). The soil sample was quartz sand locally sourced at the University of Central Florida in Orlando, FL. The soil was dry and maintained in a laboratory environment at about 40% humidity.

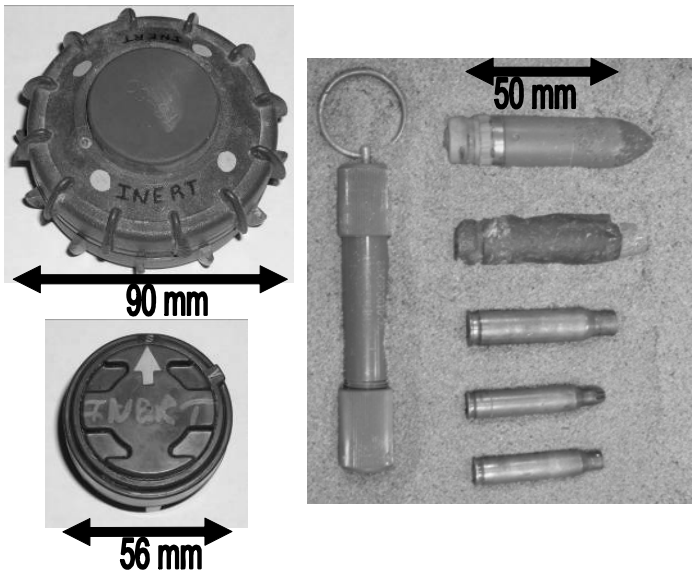

Figure 20: Photographs of the TS-50 landmine (top left), the M14 landmine (bottom left), and minefield debris (right) including from top down a 20 mm OICW practice round, a 20 mm WWII round, a 7.62 mm cartridge case, a 5.56 mm rose crimp cartridge case, a 5.56 mm standard cartridge case, and on left a fuse lighter with a metal key ring.

CHAPTER 4: SIGNAL PROCESSING

Principal Component Analysis

The initial data set is a collection of N images, each one corresponding to a mmW frequency. Figure 21 shows six of the 51 individual images, representing a different frequency, taken during a single scan. The information contained in each image about the object (TS-50 landmine, Figure 20 top left) is slightly different and you cannot distinguish whether the object is a landmine, rock, aluminum can, or some other minefield debris.

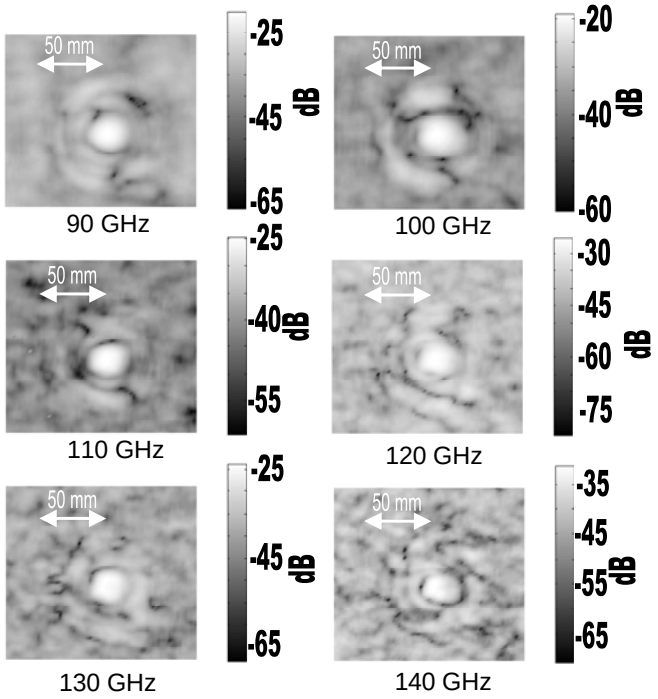

Figure 21: Six of the 51 single-frequency reflectance images taken from 90-140 GHz in 1 GHz steps of the TS-50 landmine with a 2 mm step size, buried 15 mm deep, and with a flat soil surface.

The information about the structure of the object is not concentrated around a single frequency but spread over the frequency spectrum. Therefore, it is necessary to employ a method that can combine the majority of the available information into a single image with a high signal to noise ratio.

For this purpose, we have used a Principal Component Analysis (PCA) method. PCA is a multivariate statistical method primarily developed to deal with a large ensemble of observations of *N* random variables [53]. In previous applications, the PCA method was adapted to the case of *N* images with *M* points or pixels [54]. In the case of the present work, the original data set is the collection of *N* images, parameterized by the frequency ν, $\{F(x,\nu)\}_{\nu=1,\ldots N}$ where *F* is a matrix containing all the images and *x* denotes the spatial coordinate along the scan path within the total of *M* points. The previous *N* images are each transformed to produce a mean of zero. In this framework, the *N* images are *N* random variables and the values of the pixels are "random observations". It is easy to calculate the covariance matrix between the *N* images [54]. In general, this matrix is strongly non-diagonal, which means there is a strong correlation between the images (see Figure 21). Principal components are a new set of variables (frames) that have no correlation between them. Moreover, the original frames can be seen as a linear combination of the principal components. The coefficients of these linear combinations are obtained through the diagonalization of the frame covariance matrix. This process gives you three outputs: the eigenvalues $\{\sigma_\alpha^2\}_{\alpha=1,\ldots,N}$, the eigenvectors $\{e_\alpha(\nu)\}_{\alpha=1,\ldots,N}$, and the principal components $\{Y_\alpha\}_{\alpha=1,\ldots,N}$, where α is an integer running from *1* to *N*.

To better illustrate the PCA method, a simple example will be given. We will start with three frames of 5 by 5 pixels and transform each frame to produce a mean of zero, shown in Figure 22.

$$A = \begin{bmatrix} -1.36 & -2.36 & -0.36 & -2.36 & -0.36 \\ -1.36 & 2.64 & 0.64 & 0.64 & -1.36 \\ -2.36 & 1.64 & 6.64 & 3.64 & -1.36 \\ -2.36 & 2.64 & 0.64 & 1.64 & -0.36 \\ -1.36 & -0.36 & -2.36 & 0.64 & -1.36 \end{bmatrix}$$

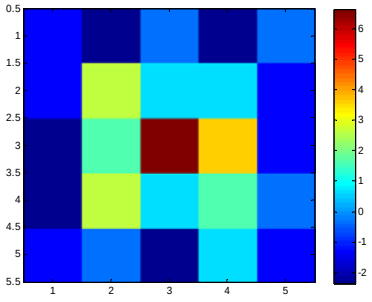

$$B = \begin{bmatrix} -2.28 & -1.28 & -2.28 & -2.28 & -0.28 \\ -0.28 & 3.72 & 1.72 & 2.72 & -2.28 \\ -1.28 & 0.72 & 6.72 & 3.72 & -1.28 \\ -2.28 & 0.72 & 2.72 & 1.72 & -1.28 \\ -1.28 & -0.28 & -2.28 & -1.28 & -2.28 \end{bmatrix}$$

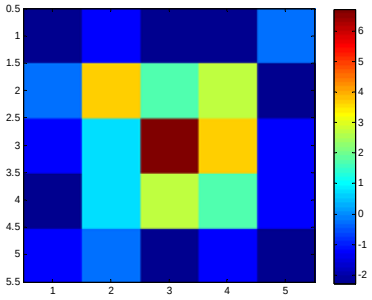

$$C = \begin{bmatrix} -2.24 & -0.24 & -1.24 & -2.24 & -1.24 \\ -0.24 & 1.76 & -0.24 & 1.76 & -0.24 \\ -2.24 & 2.76 & 5.76 & 3.76 & -2.24 \\ -0.24 & 0.76 & 2.76 & 0.76 & -1.24 \\ -1.24 & -2.24 & -2.24 & -0.24 & -0.24 \end{bmatrix}$$

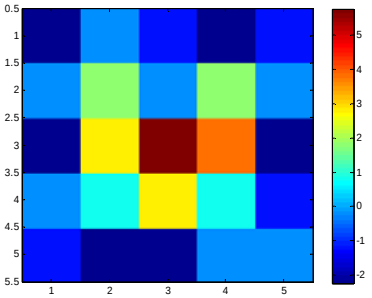

Figure 22: PCA example showing three frames transformed to produce a mean of zero.

We then put the three frames together in one 25 by 3 matrix, where each column represents the pixels of the frame.

$$Data = \begin{bmatrix} -1.36 & -2.28 & -2.24 \\ -1.36 & -0.28 & -0.24 \\ -2.36 & -1.28 & -2.24 \\ -2.36 & -2.28 & -0.24 \\ -1.36 & -1.28 & -1.24 \\ -2.36 & -1.28 & -0.24 \\ 2.64 & 3.72 & 1.76 \\ 1.64 & 0.72 & 2.76 \\ 2.64 & 0.72 & 0.76 \\ -0.36 & -0.28 & -2.24 \\ -0.36 & -2.28 & -1.24 \\ 0.64 & 1.72 & -0.24 \\ 6.64 & 6.72 & 5.76 \\ 0.64 & 2.72 & 2.76 \\ -2.36 & -2.28 & -2.24 \\ -2.36 & -2.28 & -2.24 \\ 0.64 & 2.72 & 1.76 \\ 3.64 & 3.72 & 3.76 \\ 1.64 & 1.72 & 0.76 \\ 0.64 & -1.28 & -0.24 \\ -0.36 & -0.28 & -1.24 \\ -1.36 & -2.28 & -0.24 \\ -1.36 & -1.28 & -2.24 \\ -0.36 & -1.28 & -1.24 \\ -1.36 & -2.28 & -0.24 \end{bmatrix} \quad (14)$$

We then take the covariance of the data matrix.

$$Covariance(Data) = \begin{bmatrix} \sigma_{11}^2 & \sigma_{12}^2 & \sigma_{13}^2 \\ \sigma_{21}^2 & \sigma_{22}^2 & \sigma_{23}^2 \\ \sigma_{31}^2 & \sigma_{32}^2 & \sigma_{33}^2 \end{bmatrix} = \begin{bmatrix} 4.9067 & 4.7700 & 3.9517 \\ 4.7700 & 5.8767 & 4.3883 \\ 3.9517 & 4.3883 & 4.4400 \end{bmatrix} \quad (15)$$

This matrix is non-diagonal, so we then diagonalize the covariance matrix. We first determine the eigenvalues and eigenvectors for the covariance matrix.

$$Eigenvalues = \begin{bmatrix} 13.8803 \\ 0.7464 \\ 0.5966 \end{bmatrix} \quad Eigenvectors = \begin{bmatrix} 0.5681 & -0.3959 & 0.7215 \\ 0.6293 & -0.3560 & -0.6908 \\ 0.5303 & 0.8465 & 0.0469 \end{bmatrix} \tag{16}$$

The diagonalized covariance matrix is found by multiplying the inverse of the Eigenvectors matrix by the Covariance matrix by the Eigenvectors matrix. The solution gives

$$\begin{bmatrix} 13.8803 & 0 & 0 \\ 0 & 0.7464 & 0 \\ 0 & 0 & 0.5966 \end{bmatrix} \tag{17}$$

which is diagonal. We then represent the data in the principal component space using the eigenvalues and eigenvectors, shown in Figure 23.

$$PC1 = \begin{bmatrix} -3.3954 & -2.2734 & -2.2970 & -3.9634 & -1.0383 \\ -1.0761 & 4.7742 & 1.3187 & 3.0087 & -2.3347 \\ -3.3341 & 2.8485 & 11.0557 & 6.4029 & -2.7660 \\ -2.9028 & 2.3559 & 3.5390 & 2.4171 & -1.6677 \\ -2.2357 & -1.5687 & -3.9634 & -0.5693 & -2.3347 \end{bmatrix}$$

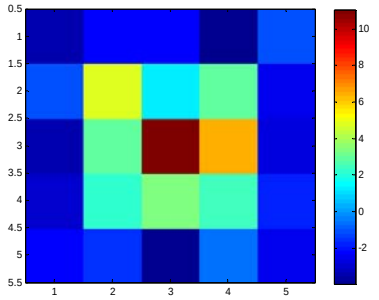

$$PC2 = \begin{bmatrix} -0.5461 & 1.1868 & -0.0955 & -0.1502 & -0.8075 \\ 0.4349 & -0.8796 & -1.0688 & 0.2682 & 1.1469 \\ -0.5062 & 1.4308 & -0.1451 & 0.4175 & -0.9021 \\ 1.5428 & -0.6581 & 1.1147 & -0.6182 & -0.4515 \\ -0.0556 & -1.6539 & -0.1502 & -0.0009 & 1.1469 \end{bmatrix}$$

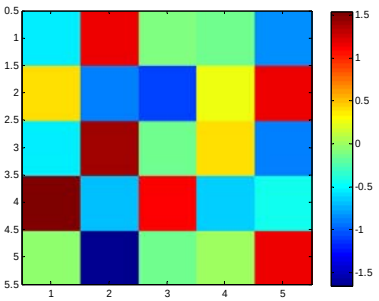

$$PC3 = \begin{bmatrix} 0.4887 & -0.8298 & 1.2571 & -0.2328 & -0.1245 \\ -0.7991 & -0.5824 & -0.7377 & -1.3347 & 0.5825 \\ -0.9236 & 0.8154 & 0.4189 & 0.2329 & -0.2021 \\ -0.1390 & 1.4431 & -1.2877 & 0.0307 & 0.5663 \\ -0.1552 & -0.1714 & -0.2328 & 1.3347 & 0.5825 \end{bmatrix}$$

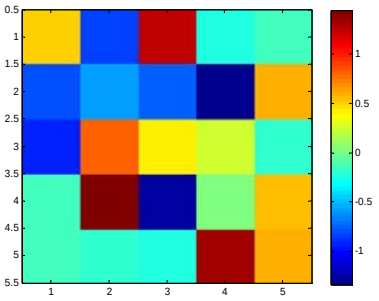

Figure 23: PCA example representing the data in the principal component space.

The principal components can be seen as the projections of the original zero mean images into a base produced by the eigenvectors. After the diagonalization, there is zero correlation between the principal components Y_α and they are calculated as linear combinations of the original images:

$$Y_\alpha(x) = \sum_{\nu=1}^{N} e_\alpha(\nu) F(x,\nu) \tag{18}$$

But, the original images can be expressed as linear combinations of the principal components too:

$$F(x,\nu) = \sum_{\alpha=1}^{N} e_\alpha(\nu) Y_\alpha(x) \tag{19}$$

Normally, the principal features of the data set are well represented by a few principal components [55]. In our case, the principal features of the landmine are well represented by only one principal component (Y_1 in Figure 24). This allows the main principal components to be selected and then to reconstruct the original images using only them, filtering out the higher components. This process is called rectification [54]. One important property of the principal components is that the factor $\sigma_\alpha^2 / \sum_{\alpha=1}^{N} \sigma_\alpha^2$ represents the portion of the total variance explained by each principal component. A statistical analysis of the principal component decomposition enables the classification and grouping of the eigenvalues and the corresponding eigenimages into processes. When a subset of eigenvalues, along with their uncertainty, can be consecutively indistinguishable, they belong to the same process. The uncertainty is produced by the finite size of data set and the high order cumulants of the underlying probability distribution [54]. The advantage of this approach is that it can be implemented automatically. A process is defined as a filtered set of frames generated by a subset of principal components. These processes could contain a single principal component or a high number of them. Based on previous applications of the method to different types of systems [56-58], different types of noise are associated with process containing a high number of principal components: they are so random that they need a high number of degrees of freedom to describe them. On the other hand, "signals" normally appear associated to processes with only one principal component or a small number of them.

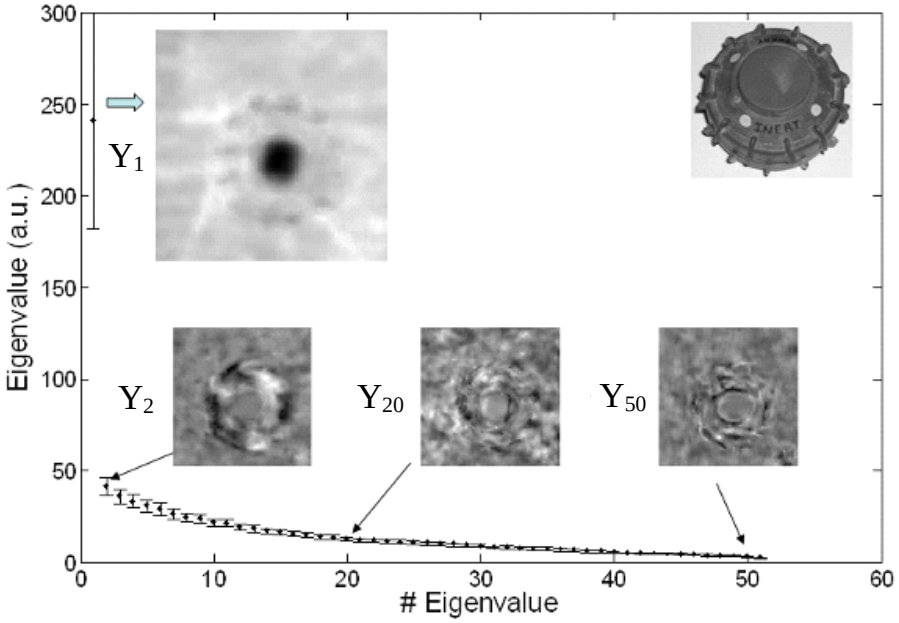

Figure 24: Application of the PCA to a set of 51 single frequency images of the TS-50 landmine. Only one relevant principal component (Y1) appears. Some of the higher components (Y2, Y20, and Y50) are represented.

We have applied the previously described method to the collection of images produced by the mmW imager. The different processes are identified by grouping the principal components that are consecutively indistinguishable together (in this case, Y_1 as its own process and Y_2 through Y_{51} as the second process shown in Figure 24). However, in later chapters the number of components contained in each grouping will differ. The two processes were determined by identifying the components that contain strong reflections from the media or object and grouping them into the lowest order components process while grouping the remaining consecutively indistinguishable components into the higher components process. An analysis over the rectified images for each process is performed. The outputs are related to physical characteristics of the

sample objects. The PCA method is applied to objects behind barriers and the results are described in the following chapters.

CHAPTER 5: LANDMINES AND UXO

TS-50 Landmine

Figure 24 shows the results of the PCA method for the set of 51 images some of which are presented in Figure 21. A relevant principal component clearly appears (Y_1) and this component resembles, with high accuracy, the shape of the object buried beneath the sand. The higher principal components are grouped together in a single process, providing useful information about the structure (flat or curved) and composition (metal or plastic) of the object which will be discussed below. Figure 25 represents the total amount of variance explained by each principal component. The first principal component only represents about 27% of the total variance.

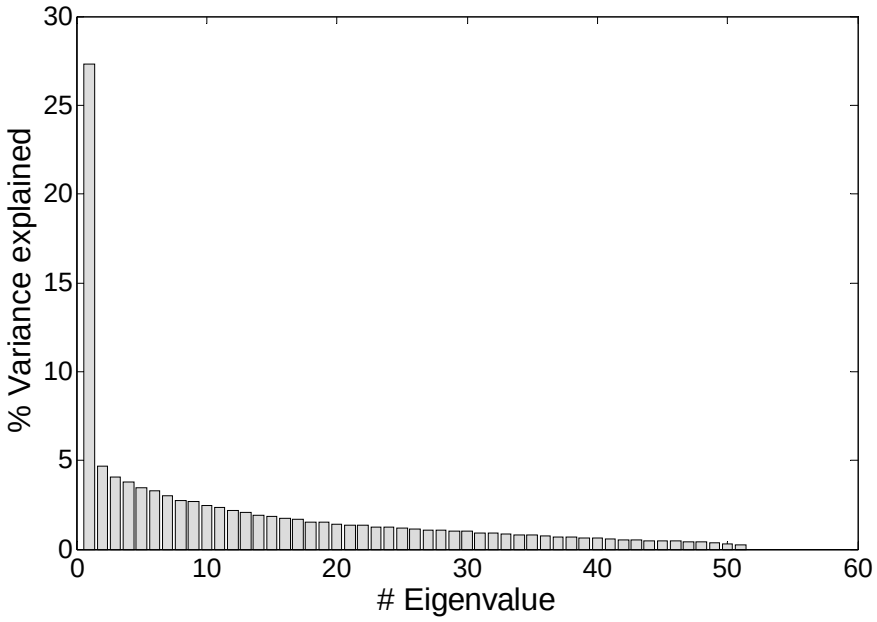

Figure 25: Percentage of variance explained by the principal components of Figure 24.

Two different sub-data sets were constructed: the first one coming from the rectification using only the first principal component and the second from the rectification using the higher components. For each data set, the mean value and the standard deviation of each pixel is calculated and three images are constructed: the mean value (signal), the standard deviation (STD) and the ratio of them (signal-to-noise ratio-SNR). The results are shown in Figure 26. The first principal component reconstructs the original shape of the object with high accuracy and high signal-to-noise ratio (typically 6 to 18). The threshold value of the signal to noise ratio for which the target is detectable half the time was determined experimentally in [59] to be between 2 to 3. The metal inside of the mine is clearly seen in the signal, meaning that the metal reflection drives it. However, reflections from the plastic body of the mine showing the structure of the strengthening ribs are seen. We also reconstruct the data using the remaining components (higher components) and perform the same analysis as before obtaining the signal, STD, and SNR. In the reconstruction with the higher components, the signal is weaker, but the standard deviation is high. The difference in the structure and material of the background and object is responsible for this behavior. The plastic part of the object is curved and the reflection changes with the angle, while the background is random. Also, the reflection from the plastic varies at different frequencies which will be represented by the higher order components. This is the reason the STD of the higher order components is greater than the STD of the first principal component. The main difference is that while a strong signal is produced mainly by metal components of the object, the structure in the higher components is mainly driven by the structure of the plastic material.

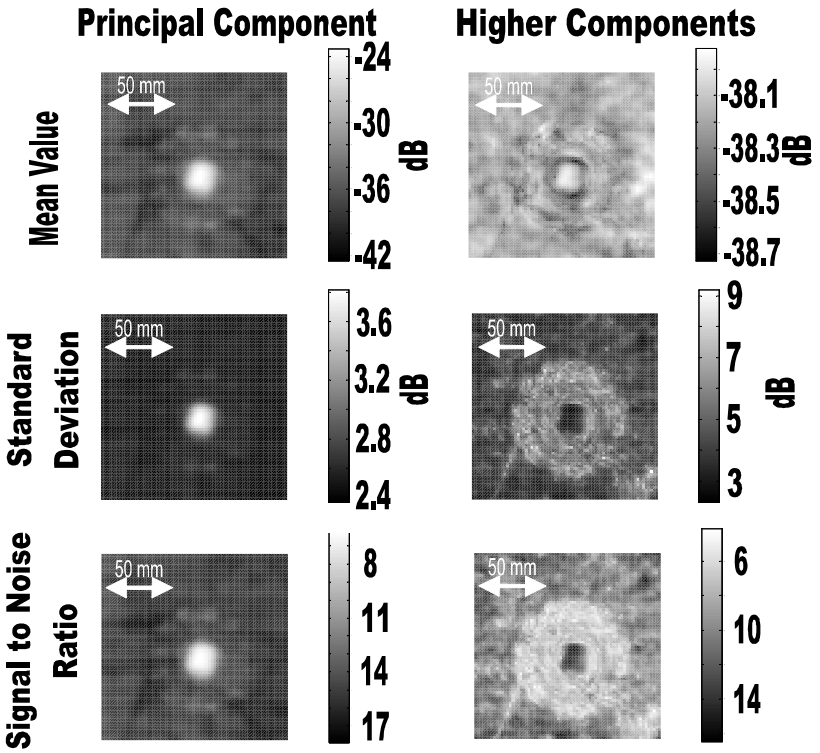

Figure 26: Images of the mean value, standard deviation and signal-to-noise ratio for the rectified images of Figure 20 with the first principal component (left) and the higher components (right) of a TS-50 landmine at 2 mm step size, 15 mm deep, and with a flat soil surface.

M14 Landmine and UXO

Antipersonnel mines very widely in size, shape, and material content depending on their intended use and burial location. The PCA method was applied to other landmines and minefield debris. The M14 landmine has a different size and shape compared with the TS-50 as well as a much smaller metal content. Images were taken for the M14 landmine with a 2 mm step size, buried 15 mm deep, and with a flat soil surface. As with the previous mine, the PCA method allows the structure and composition of the mine to be identified. The results are given in Figure 27. The unique structure of the top cap of the mine can be identified from the principal

component images. The higher component images show the plastic composition of the landmine. The percentage of variance explained by the first principal component is similar to the previous case.

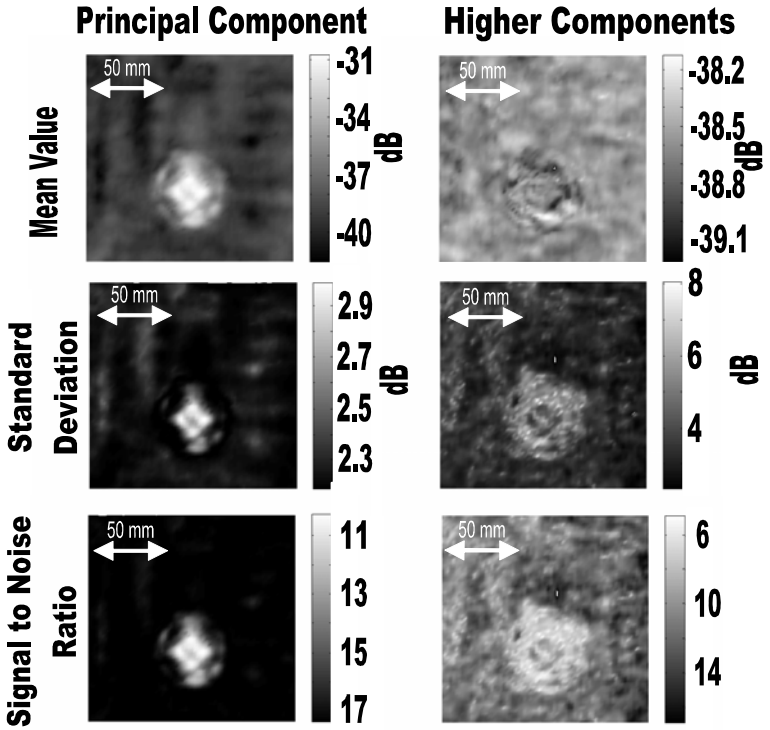

Figure 27: Images of the mean value, standard deviation and signal-to-noise ratio for the rectified images of an M14 landmine with the first principal component (left) and the higher components (right) at 2 mm step size, 15 mm deep, and with a flat soil surface.

Figure 28 shows the results of the analysis for a collection of bullet cartridges and other types of minefield debris. In this case, the object is not visible in the first principal component, but in the STD of the reconstruction with the higher components. The curvature of the objects introduces deviations in the reflection coefficients. In the previous images, the metal was large and planar compared to the wavelength, which produce strong reflections. In this case the dimensions of

the metal parts are small or comparable to the wavelength, producing small backscattering. The objects are curved and the reflection changes with the angle introducing a high STD. The PCA method can even distinguish between the objects with such small fluctuations allowing the minefield debris to be located and identified.

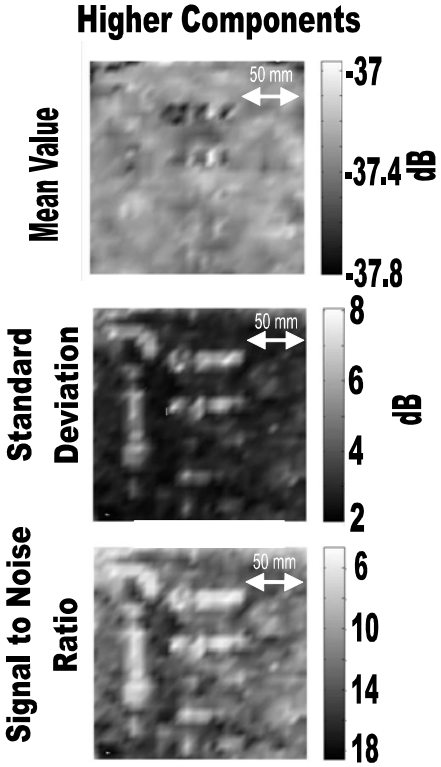

Figure 28: Images of the mean value, standard deviation and signal-to-noise ratio for the rectified images of the minefield debris with the higher components at 2 mm step size, 15 mm deep, and with a flat soil surface. The principal component rectified images did not show any features of the objects.

Resolution, Depth, and Soil Surface

The influences of other physical characteristics related to mine detection were explored. These factors include image resolution, depth of the object, and the condition of the soil surface. For

this study the TS-50 landmine analyzed earlier in this chapter was selected. In all cases the level of the first principal components is between 25%-30% of the total data-set variance.

Figure 29 shows the images of the TS-50 landmine when the resolution of the scan is 5 mm steps with a depth of 15 mm and the soil surface flat. This figure can be compared to Figure 26 (2 mm steps, 15 mm depth, and flat soil surface). The added resolution from a step size of 5 mm to 2 mm does not change the overall image significantly.

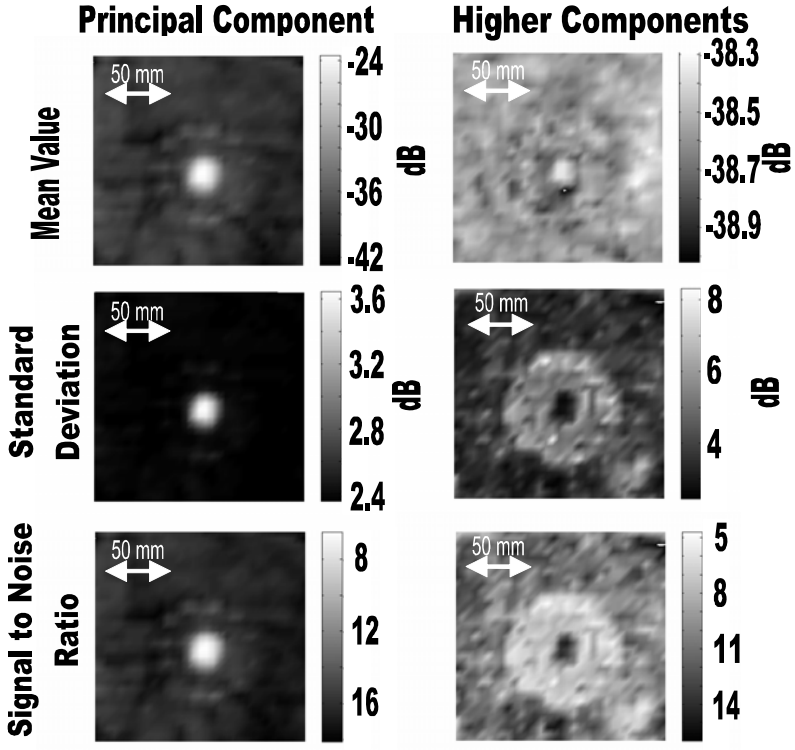

Figure 29: Change in resolution: Images of the mean value, standard deviation and signal-to-noise ratio for the rectified images of a TS-50 landmine with the first principal component (left) and the higher components (right) at 5 mm step size, 15 mm deep, and with a flat soil surface.

The 2 mm step size over samples the image without adding useful information while adding time to complete the scan. The spot size of the imaging system is about 6 mm, therefore, it is

sufficient to use a 5 mm step size while taking images, since our system is not a sub-diffraction limited/super resolution process.

Images of the TS-50 landmine buried at a depth of 50 mm with 5 mm steps and a flat soil surface is shown in Figure 30. This figure can be compared to Figure 29 (5 mm step size, 15 mm depth, and flat soil surface). Changing the depth affects the images in two ways. First, the radiation has to travel a longer distance in the random soil, increasing the effects of scattering which decreases the reflected signal from the object. Second, the uncertainties related to the beam focus are increased causing a blur over the object. However, the PCA method can extract information from the first principal component and higher components locating and identifying the landmine. Due to the depth of the landmine compared to the size of the container and the orientation of the VNA modules, the edges of the container can be seen in Figure 30.

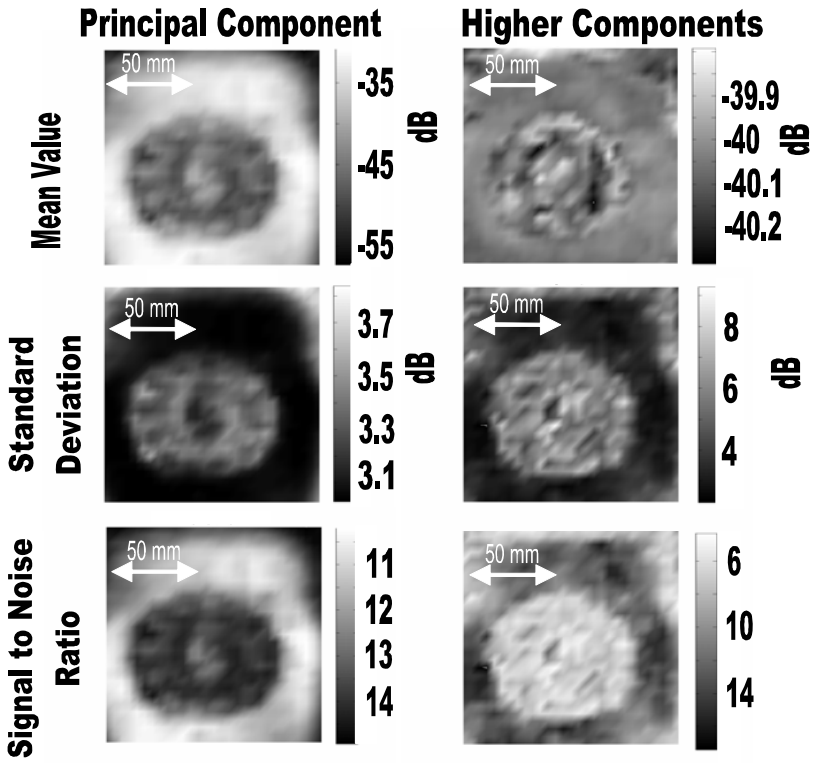

Figure 30: Change in depth: Images of the mean value, standard deviation and signal-to-noise ratio for the rectified images of a TS-50 landmine with the first principal component (left) and the higher components (right) at 5 mm step size, 50 mm deep, and with a flat soil surface.

Figure 31 shows the images of the TS-50 landmine with a 2 mm step size at a depth of 15 mm with a disturbed soil surface. This figure can be compared to Figure 26 (2 mm step size, 15 mm depth, and a flat soil surface). The images of the flat soil surface and the disturbed soil surface show a comparison between an ideal smooth surface and a real world type of situation where the surface above the mine is disturbed. The disturbed surface introduces a blur in the image and increases the effects of scattering while largely destroying the useful information in the higher components. The landmine is detected and identified in spite of the disturbed surface, degrading only the higher components information about the plastic in the mine. It is important to note that in both cases the maximum signal level, standard deviation, and signal to noise ratio are similar.

This supports the idea that disturbed surface soil can be modeled as a blur or scattering imposed over the image.

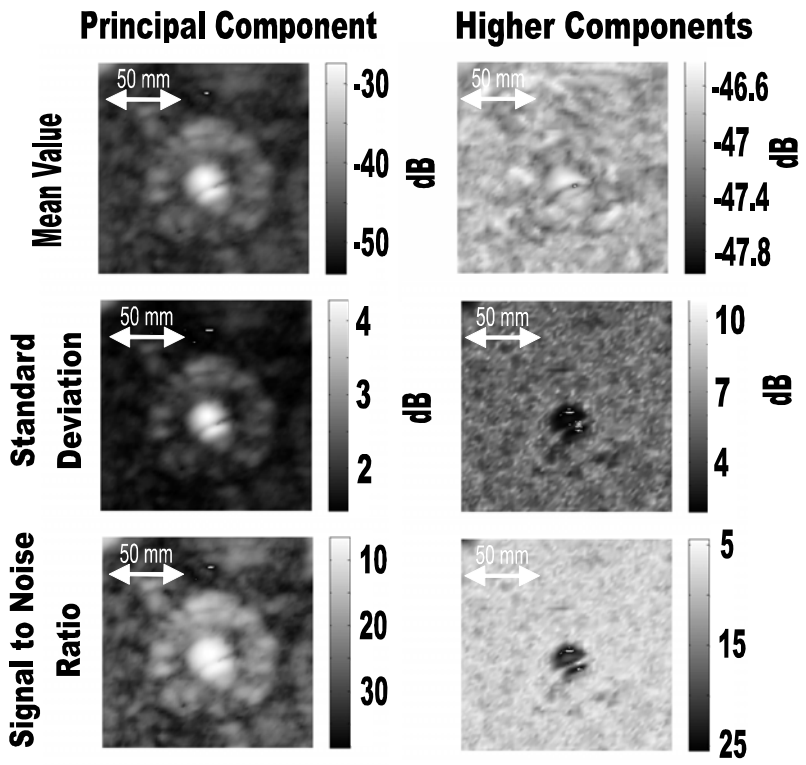

Figure 31: Change in soil surface: Images of the mean value, standard deviation and signal-to-noise ratio for the rectified images of a TS-50 landmine with the first principal component (left) and the higher components (right) at 2 mm step size, 15 mm deep, and with a disturbed soil surface.

CHAPTER 6: MARS ROCK IMAGING

Introduction

The detection of rocks beneath the loose soil on Mars is important and will allow vehicles such as the Mars rover to safely navigate around areas where the soft soil can potentially trap the vehicle for many weeks. In June 2005, the Mars rover Opportunity sunk deep into the Martian soil and was trapped for about 5 weeks before working its way free [60-61]. Again in June 2006, the back two tires of the Mars rover Opportunity became stuck in the loose soil for over a week [62-63]. Avoiding these traps will save time, resources, and possibly the vehicle. The ability to detect buried rocks will depend on soil transmission and scattering. Soils with particle sizes larger than the wavelength have low transmittance due to scattering [64]. A hyperspectral millimeter wave (mmW) imaging system used to penetrate the simulated Martian soil and detect the rock underneath is demonstrated. The mmW imager operates from 90-140 GHz. This mmW imager system has been previously demonstrated to detect buried plastic landmines [65]. The information provided by the hyperspectral images is analyzed through a principal component analysis (PCA) image processing method. With this procedure, structural information about the object is condensed into single images and the buried object can be located. There is no material difference between the soil and the rock producing a difficult detection scenario. The difference in the density of the rock compared to the soil is determined using the PCA method. We present the sample preparation, experimental set up for the mmW imaging system, the signal processing method used, and imaging results of the buried rocks.

Sample Preparation

To simulate the soil and rocks found on Mars, a bag of lava rocks (Red Volcanic Moon Rocks®) was procured commercially. The larger lava rocks were set aside to be used as Mars rock samples (Figure 32 left). The remaining rocks were hand crushed using an aluminum pipe and a piston-like handle into lava sand (Figure 32 right). The pulverized sand was sieved, removing all particles larger than 1 mm, giving particle sizes similar to those found in other Mars test beds [66]. Most of the particles were a fine dust, but some were as big as 1 mm. The soil and the rocks were then baked in an oven at 275 degrees Fahrenheit for over 24 hours to remove moisture.

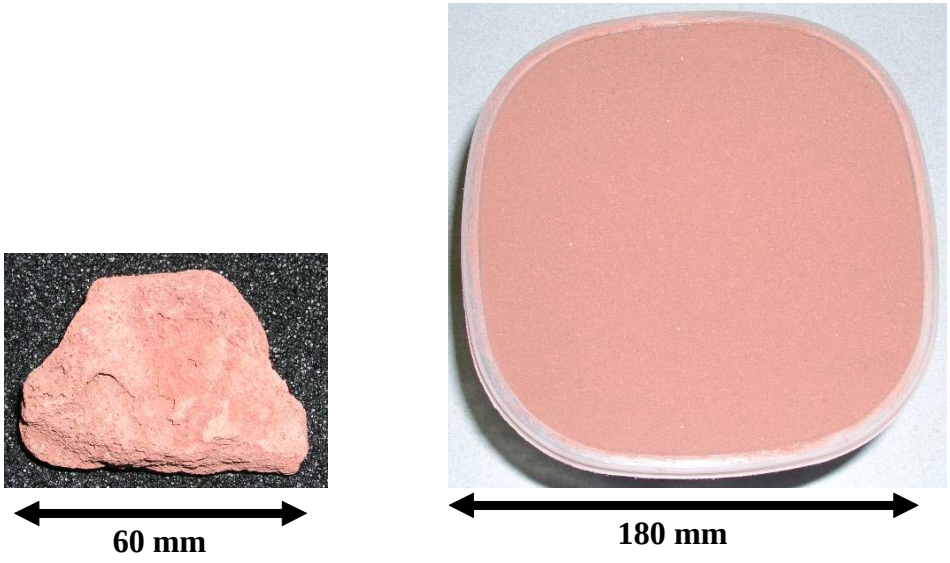

Figure 32: Photographs of the lava rock with a height of 45 mm and a length of 60 mm (left) and lava sand (right) used in the imaging measurements.

Imaging Setup

The mmW imaging system uses an Anritsu vector network analyzer (VNA) operating from 90-140 GHz as the source and detector. The power emitted from the VNA ranges from 0.2 mW to 2 mW throughout the 90-140 GHz band. The imaging setup is similar to the one described in chapter 3 with a few improvements for Mars imaging, shown in Figure 33, right. HDPE lenses were fabricated with a focal length of 139.7 mm for deeper measurements. Manual translation stages were added to the VNA modules to allow adjustment of the imager height. The Mars rock was placed in a larger 18 cm × 18 cm × 22 cm container surrounded by the simulated Martian soil.

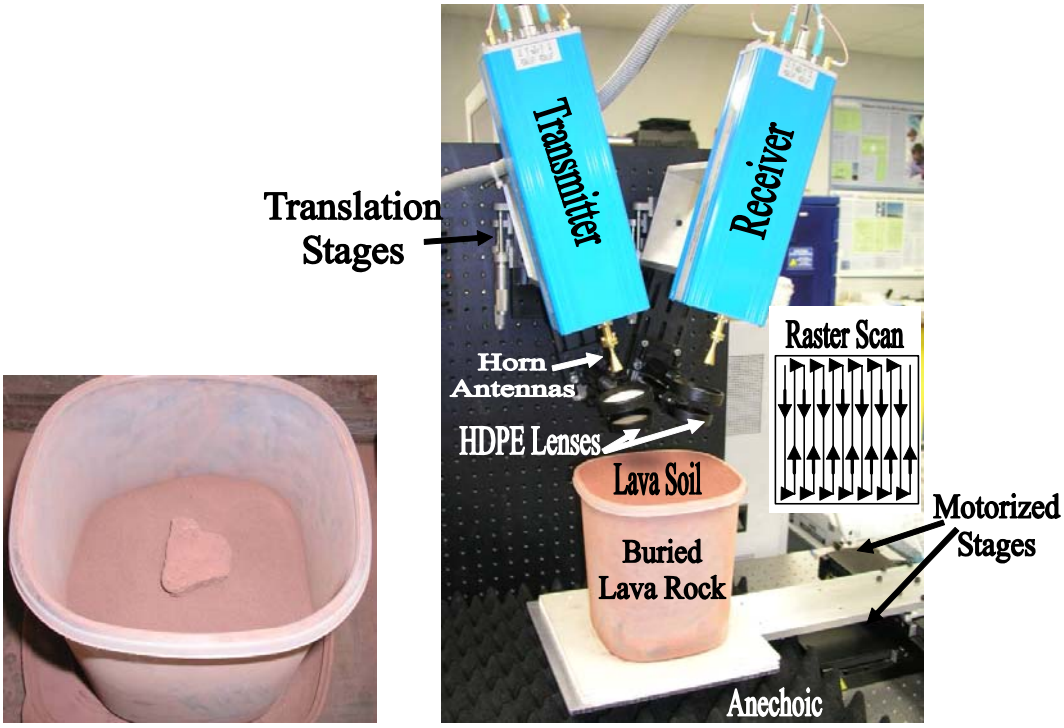

Figure 33: (Left) Photograph of the lava rock before being covered by lava sand. (Right) Photograph of the active hyperspectral mmW imaging system. (Inset) Schematic of the path for taking a raster scan image.

A broadband convoluted foam millimeter wave absorber, ECCOSORB CV, was placed under the sample to eliminate back reflections from the optical table. A program was written in LABVIEW to capture a raster scan image (Figure 33 inset), containing either 29 (Figure 36 through Figure 40) or 37 (Figure 34, Figure 35, and Figure 41) lines, of the lava rock under the soil. At each position of the scan, the VNA measured the reflected power, spectrally resolved from 90-140 GHz in 1 GHz steps. The images taken were 180 mm × 180 mm (Figure 34, Figure 35, and Figure 41) or 140 mm × 140 mm (Figure 36 through Figure 40) with a 5 mm step size.

Figure 34 shows the application of the PCA to a set of 51 single frequency images of the lava rock. The components are grouped into two processes: the lowest order component process and the higher components process. The lowest order component process is dominated by the reflection from the soil surface. The standard deviation image of this component process has very little contrast and the lava rock can not be seen. The reflections from the lava rock are small compared to the lowest order component but can be seen in the higher components process using the PCA method. The higher components process is used in the detection of the lava rock in the results to follow.

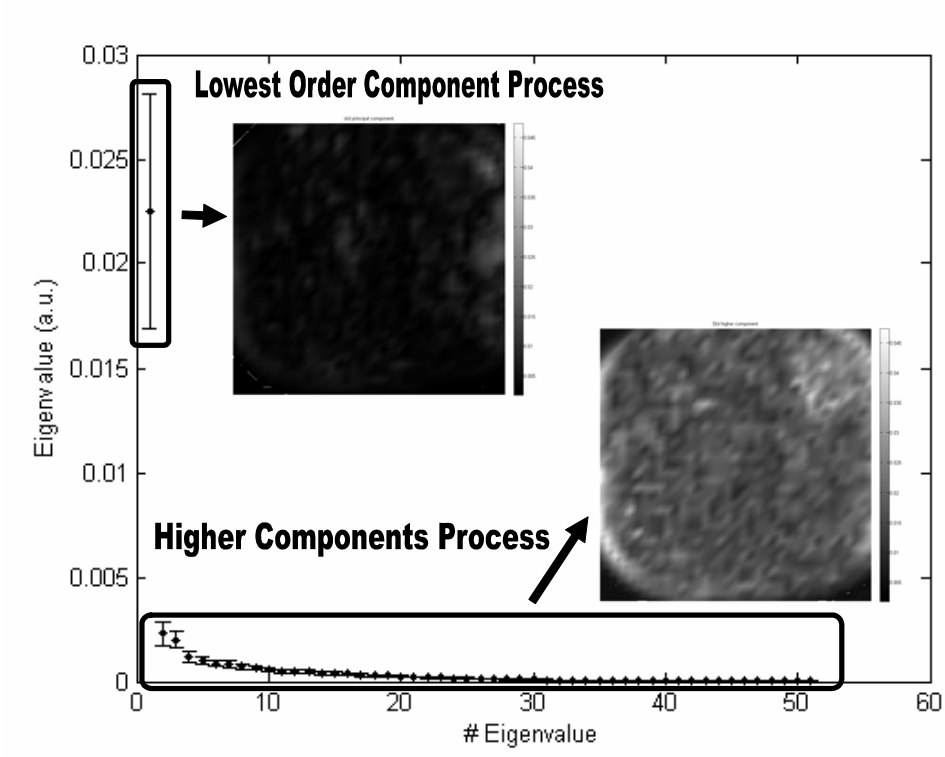

Figure 34: Application of the PCA to a set of 51 single frequency images of the lava rock buried in the upper right corner. The components are grouped into 2 processes. The buried lava rock is detected using the higher components process.

Results

The images from the mmW imaging system show the lava rock buried in lava sand at various depths. The rocks were buried at depths of 5 mm (0.2”), 15 mm (0.6”), 25 mm (1”), 38 mm (1.5”), 50 mm (2”), 64 mm (2.5), and 76 mm (3”).

In Figure 35, the lava rock buried 5 mm deep can be seen in the upper right hand corner of the standard deviation image of the higher components. Even though the rock is not placed in the center of the box, the rock is easily located.

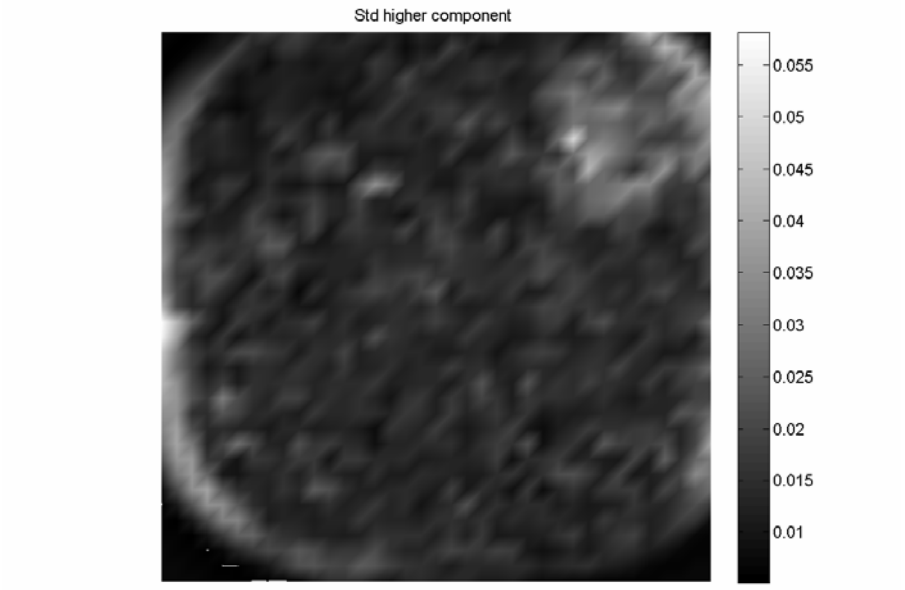

Figure 35: Standard deviation image of the lava rock (upper right corner) buried 5 mm deep in lava sand. The image is 180 mm x 180 mm with a step size of 5 mm.

Figure 36 shows the lava rock buried 15 mm beneath the lava soil. The rock is detected in the lower middle portion of the standard deviation image of the higher components.

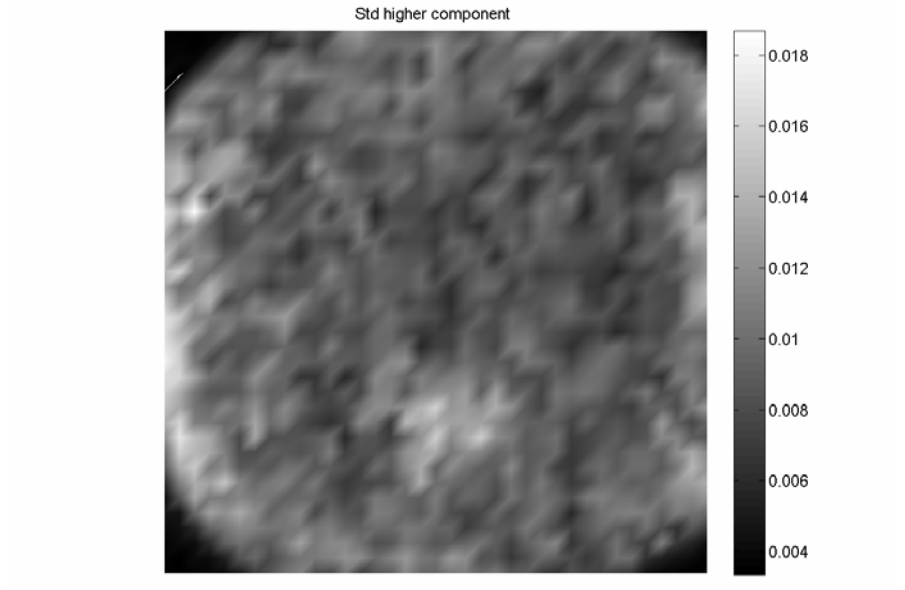

Figure 36: Standard deviation image of the lava rock (lower center) buried 15 mm deep in lava sand. The image is 180 mm x 180 mm with a step size of 5 mm.

In Figure 37, the rock is buried 25 mm deep. To prevent large reflections from the side walls due to the angle of incidence of the imager and the limited size of the sample box, only the region of interest was imaged. The rock is detected in the middle of the image.

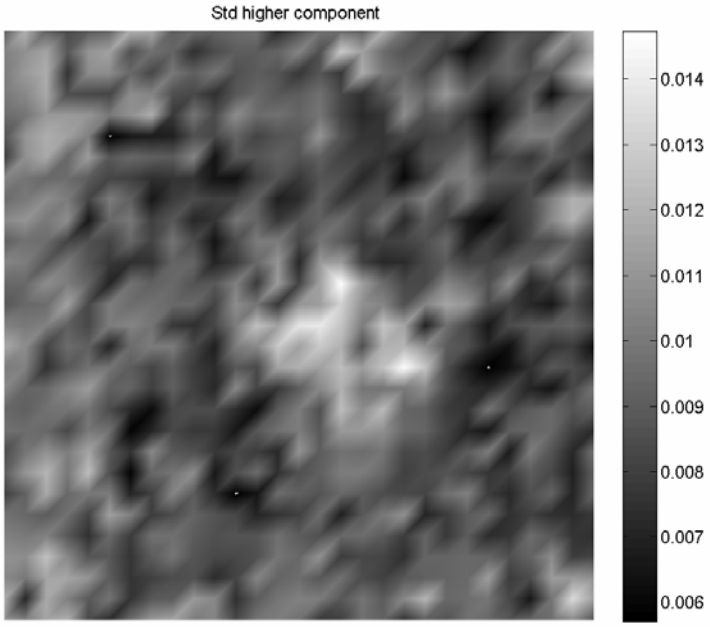

Figure 37: Standard deviation image of the lava rock (center) buried 25 mm deep in lava sand. The image is 140 mm x 140 mm with a step size of 5 mm.

Buried 38 mm deep, the rock is still detected in the middle of the standard deviation image of the higher components, shown in Figure 38.

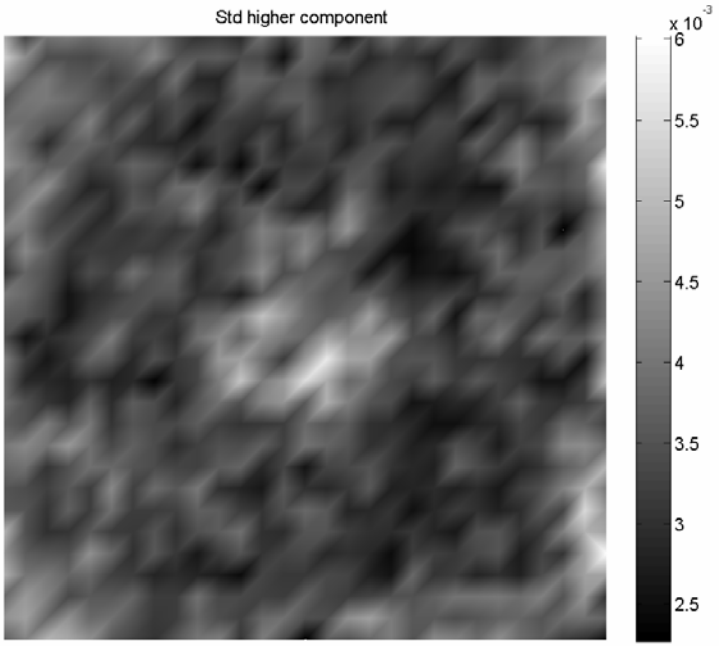

Figure 38: Standard deviation image of the lava rock (center) buried 38 mm deep in lava sand. The image is 140 mm x 140 mm with a step size of 5 mm.

Figure 39 shows the lava rock buried 50 mm beneath the lava soil. Losses due to scattering from the granular nature of the background soil are starting to appear, but the rock is still detected in the middle of the image.

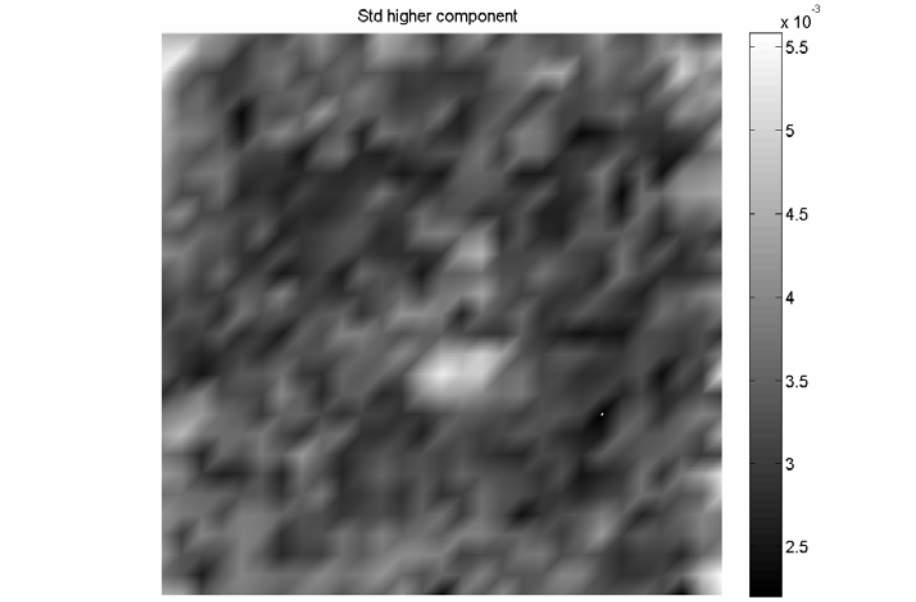

Figure 39: Standard deviation image of the lava rock (center) buried 50 mm deep in lava sand. The image is 140 mm x 140 mm with a step size of 5 mm.

At 64 mm beneath the lava soil, the image of the lava rock is degraded further by scattering but can still be detected in the middle of the images, shown in Figure 40.

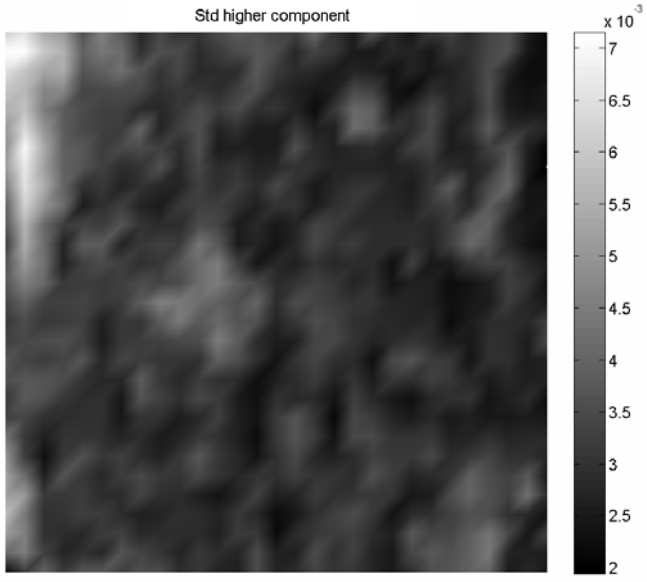

Figure 40: Standard deviation image of the lava rock (left center) buried 64 mm deep in lava sand. The image is 140 mm x 140 mm with a step size of 5 mm.

Figure 41 shows the lava rock buried 76 mm beneath the lava soil. The rock can barely be distinguished from the surrounding soil. The reflected signal from the rock has the same magnitude as random reflections from the surrounding soil.

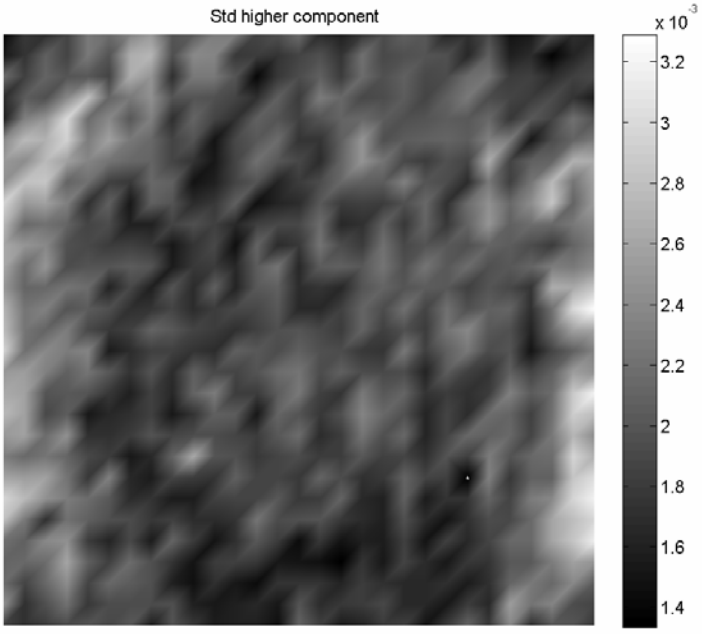

Figure 41: Standard deviation image of the lava rock (lower center) buried 76 mm deep in lava sand. The image is 140 mm x 140 mm with a step size of 5 mm.

Multiple scans were taken of the 15 mm deep lava rock buried in lava sand, stepping the height of the imager 5 mm increment from the sample. Figure 42 shows the multiple images of the lava rock at different heights. The lava rock can be seen coming into focus as the focal plane reaches the height of the rock. As the plane passes the top of the rock, the image of the rock disappears.

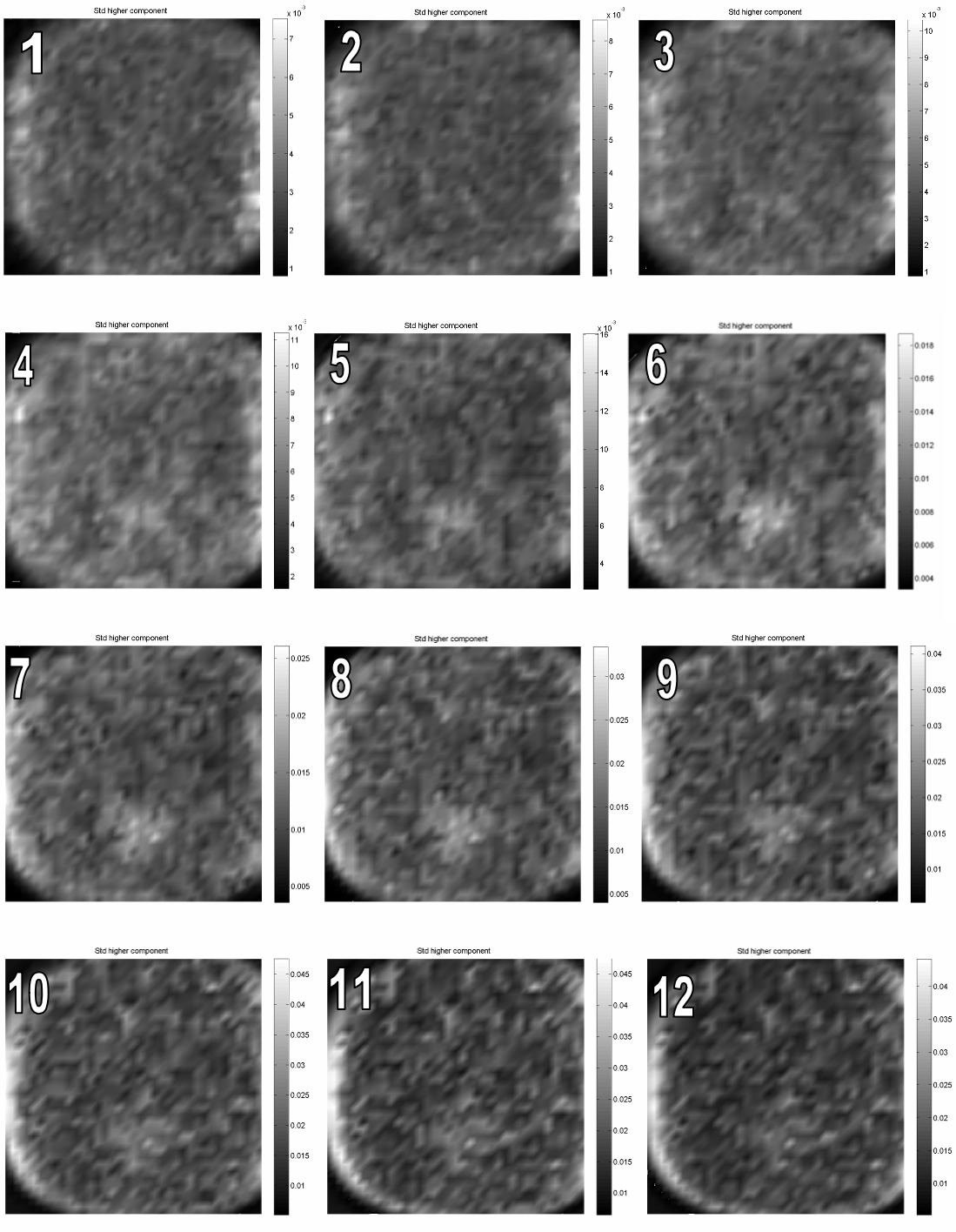

Figure 42: Multiple scans of a lava rock buried 15 mm deep as the height changes in 5 mm steps. Frame 1 was taken furthest away from the sample with frame 12 just above the surface. The lava rock comes into focus and then disappears as the height changes.

The depth of focus of the mmW imaging system can be determined and compared to the images presented in Figure 42. A schematic of the depth of focus, $\delta z'$, of the lens is shown in Figure 43. The diffraction limited spot size of the lens is given as *d* and the image of the lens is at the focus *f*. The object can be placed anywhere within the distance $\delta z'$ without loss to image clarity. Similar triangles give [67],

$$\frac{D/2}{f} = \frac{d/2}{\delta z'/2} \tag{20}$$

where *D* is the diameter of the lens. The depth of focus is given as,

$$\delta z' = \frac{2df}{D} \tag{21}$$

where the diffraction limited spot size is

$$d = \frac{2.44\lambda f}{D} \tag{22}$$

Therefore,

$$\delta z' = \frac{4.88\lambda f^2}{D^2} \tag{23}$$

where λ is the wavelength.

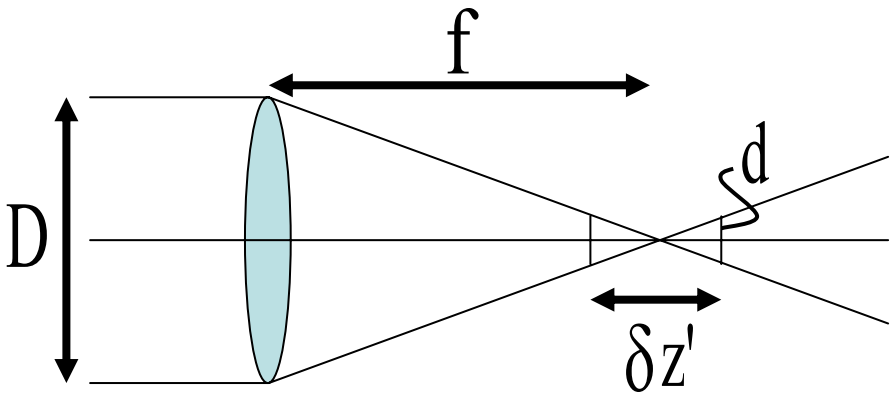

Figure 43: Depth of Focus Schematic

The depth of focus for the 90-140 GHz range is 63 mm to 40 mm for a focal length of 100 mm and a lens diameter of 50.8 mm. Since all of the frequencies are present in the images, the average depth of focus is 51.5 mm for the range. Figure 42 experimentally shows the depth of focus of the lava rock. The lava rock starts to appear in frame 3 and disappears again in frame 11. Since each frame was taken in 5 mm vertical increments, the experimental depth of focus is 40 mm ± 10 mm. This result compares well with the predicted value.

Discussion

A 90-140 GHz mmW imaging system was used to detect lava rock buried beneath lava sand at various depths, simulating the soil and rocks found on Mars. The principal component analysis method was applied to the 51 frames to help locate the lava rock beneath the soil. The rock was located in the standard deviation image up to 76 mm beneath the surface. After 76 mm, the rock could not be distinguished from its surroundings. An increase in power would be needed to further penetrate this depth of sand. Also, the diffraction limited spot size of a 50.8 mm (2”) diameter lens with a focal length of 139.7 mm (5.5”) is large compared to the size of the rock under test decreasing the chance of detection. With increased power and aperture size, the detection of larger lava rocks beneath lava soil at greater depths is promising in the 90-140 GHz range.

CHAPTER 7: IMAGING THROUGH DRYWALL

Introduction

Imaging through barriers will allow an object to be located and identified before breaching the barrier. The previous chapters have discussed imaging through soil which is just one type of barrier that mmW radiation can penetrate. Drywall or sheetrock is made up of gypsum plaster encased in heavy paper. Drywall is commonly used as interior walls or ceilings within the United States. Imaging through the walls will allow a potential threat to be located, identified, and assessed before entering a room. Imaging inside of the drywalls will also allow for the detection of electrical wires, water pipes, gas pipes, and support structures without breaching the barrier. Police can use mmW imaging to locate illegal drugs and weapon caches hidden inside of the walls. During a fire or natural disaster, rescue workers will be able to search an entire house without entering every room using a mmW imager through the drywall. A mmW imaging system can also inspect sealed packages and envelopes for suspicious content. Millimeter wave images were taken of objects behind drywall and analyzed using the PCA method. The drywall thickness threshold and standoff distance were investigated. This chapter presents mmW images of objects behind barriers of different thickness and standoff distance.

Drywall Imaging Setup

The mmW imaging setup is similar to the setup discussed in the previous chapters except only one transmit/receiver module is used, shown in Figure 44. The reflected signal is measured by the same transmit module. This allows the radiation to propagate perpendicular to the sample

instead of at an angle. Two sheets of drywall separated by a wood box frame were fabricated for the imaging measurements. The thickness of one drywall sheet was 12.7 mm. Samples were placed inside of the drywall box and a raster scanned image was taken from 90-140 GHz in 1 GHz steps. The samples were made of metal, plastic, and rubber material. These samples include a metal handgun, scissors, shears, box cutter, toy gun, kitchen knife, and calculator.

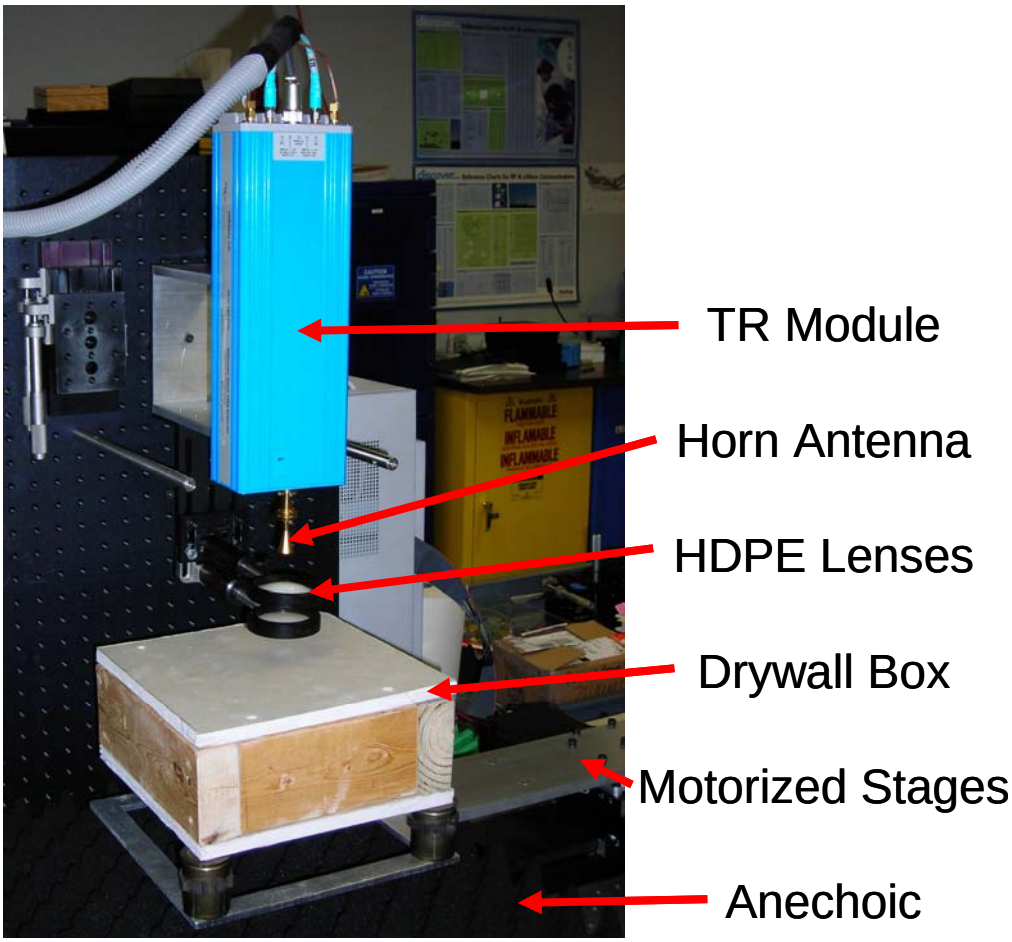

Figure 44: Picture of the drywall imaging set up

Results

Figure 45 shows six of the 51 images of a metal handgun taken from 90-140 GHz in 1 GHz steps. Strong vertical bands from etalon resonance of the drywall can be seen. The image of the handgun is present in each frame but the structure of the gun is not clear.

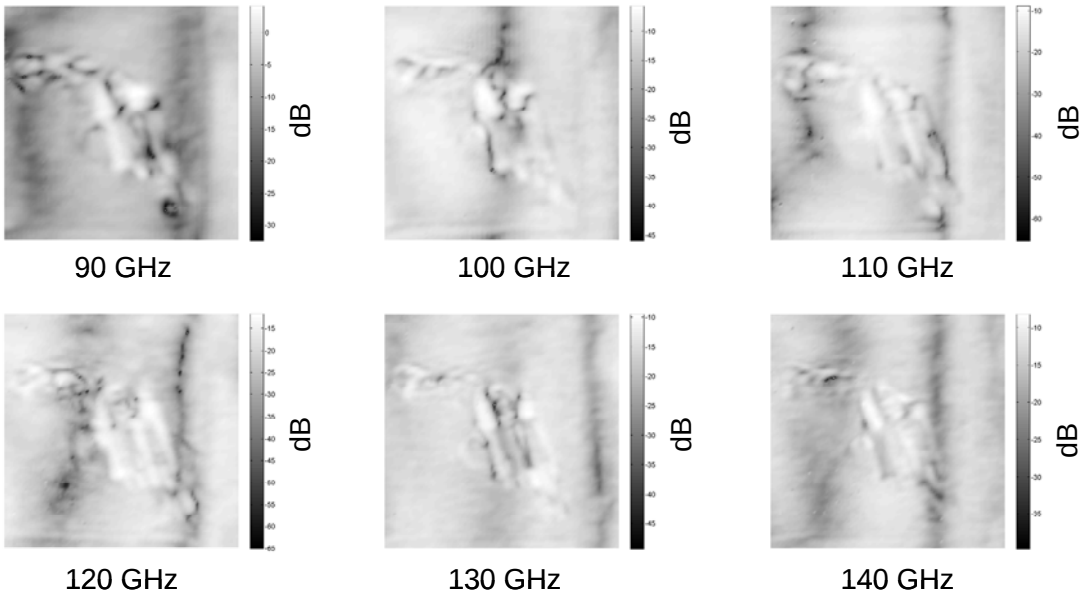

Figure 45: Six of the 51 single-frequency reflectance images taken from 90-140 GHz in 1 GHz steps of a metal pistol 8.5 cm beneath one sheet of drywall.

The PCA method is applied to the 51 images of the handgun, shown in Figure 46. The components are again grouped into two processes: the lowest order components process (the first three components) and the higher components process (the remaining components). The two processes were determined by identifying the components that contain strong reflections from the drywall and grouping them into the lowest order components process while grouping the remaining components into the higher components process. The lowest order components

process is dominated by the reflection from the drywall. The handgun can be seen in the lowest order components, but a clearer image can be obtained by eliminating the components with the strong reflection from the drywall. The reflections from the handgun are clearly seen in the higher components process using the PCA method. The higher components process is used in the detection of objects behind drywall in the results to follow.

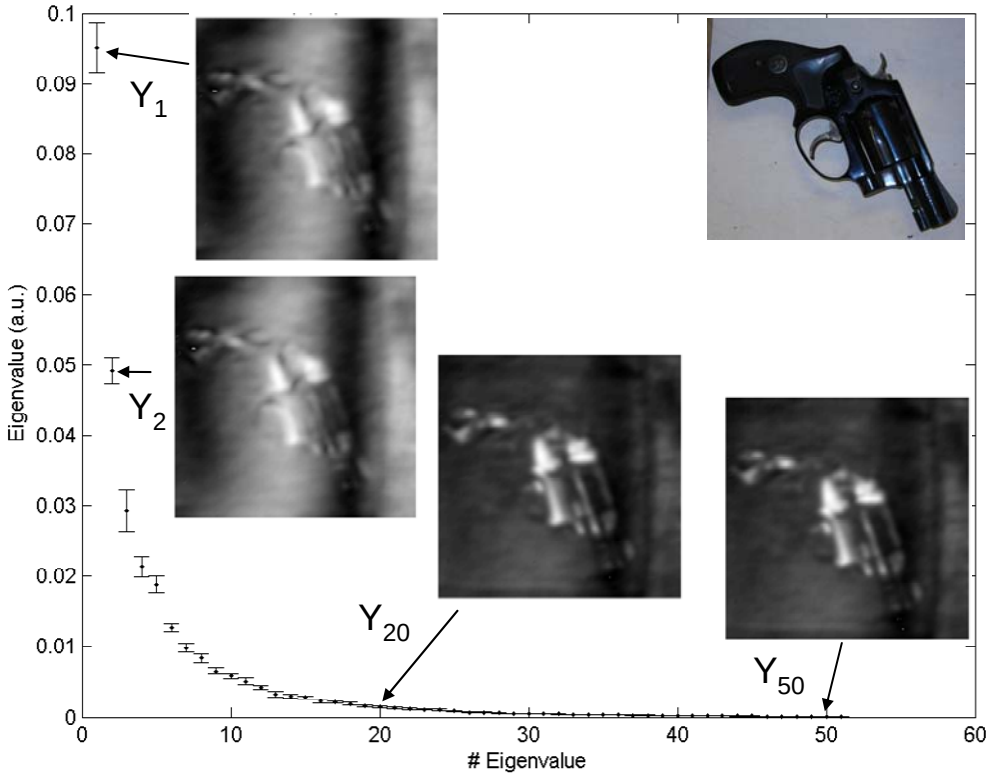

Figure 46: The PCA method applied to a metal pistol imaged 5.8 cm behind one sheet of drywall.

A higher component process image of scissors with a plastic handle located 8 cm behind one sheet of drywall is shown in Figure 47. The scissors are clearly seen including detail of the

blades and the screw connecting the two blades together. The plastic handle is present in the image but with a lower contrast to the background.

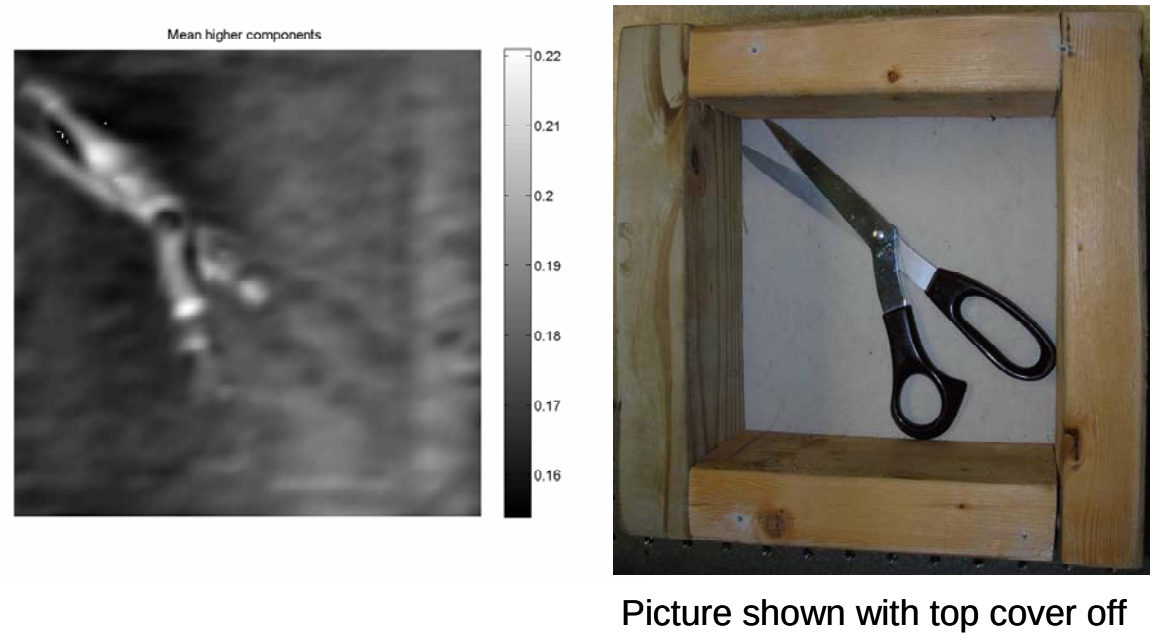

Figure 47: A pair of scissors imaged 8 cm behind one sheet of drywall, mmW higher component process image (left) and photograph (right).

Figure 48 shows the mmW higher component process image of a pair of shears located 7.1 cm behind one sheet of drywall. All portions of the shears are identifiable in the image, except the small metallic spring in the middle. This image also shows which part of the handle contains metal beneath the plastic. Again the plastic handle can be seen at a lower contrast than the metal portions.

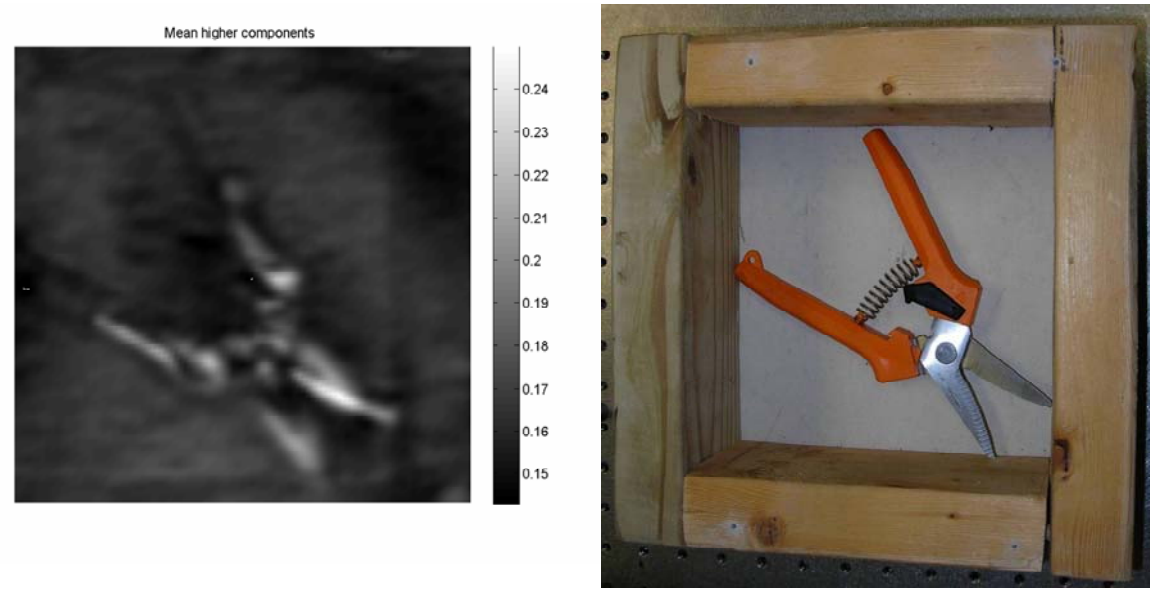

Figure 48: A pair of shears imaged 7.1 cm behind one sheet of drywall, mmW higher component process image (left) and photograph (right).

A higher component process image of a metal box cutter located 7.2 cm behind one sheet of drywall is shown in Figure 49. Made entirely of metal, the box cutter is clearly seen including the blade.

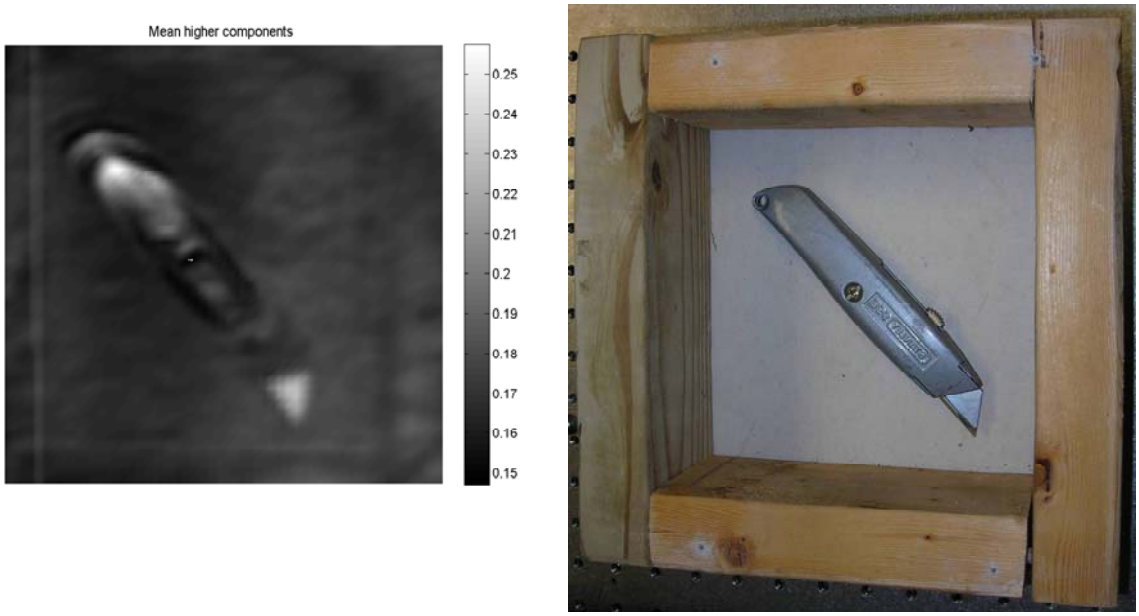

Figure 49: A box cutter imaged 7.2 cm behind one sheet of drywall, mmW higher component process image (left) and photograph (right).

A higher component process image of a plastic toy gun located 6 cm behind one sheet of drywall is shown in Figure 50. Even though the toy gun contains very little metallic material, the plastic can be seen clearly in the image. The plastic portions of the scissors and shears were harder to see due to the low contrast compared to the metal. However, images of plastic material not compared to the contrast of metal are clearer.

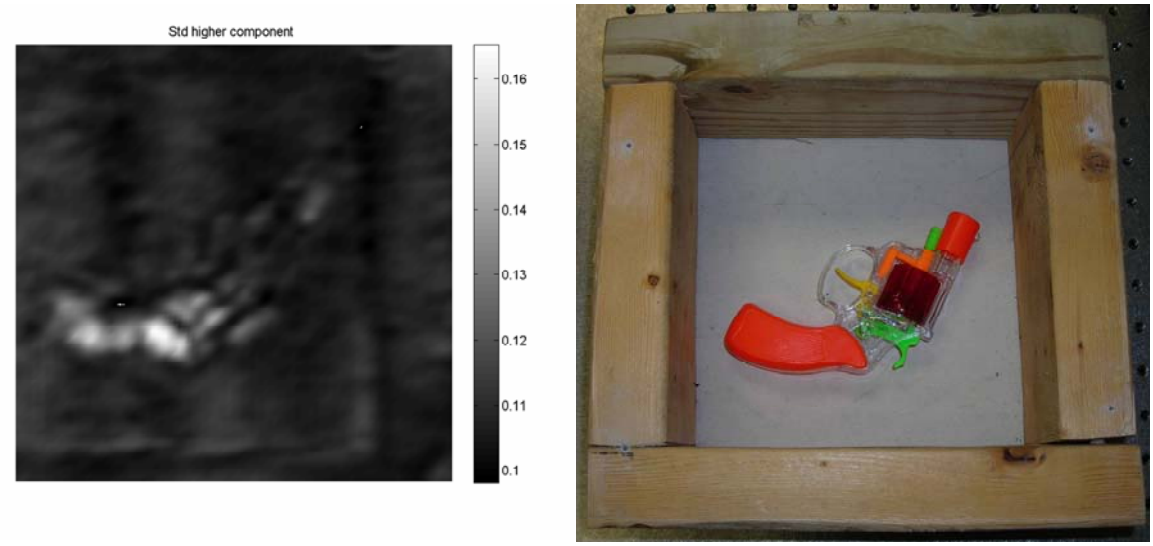

Figure 50: A plastic toy gun imaged 6 cm behind one sheet of drywall, mmW higher component process image (left) and photograph (right).

Figure 51 shows the higher component process image of a kitchen knife located 7.3 cm behind one sheet of drywall. The kitchen knife is clearly identified in the image. The portion of the metal that reaches into the plastic handle is seen. The plastic handle is again seen at a lower contrast.

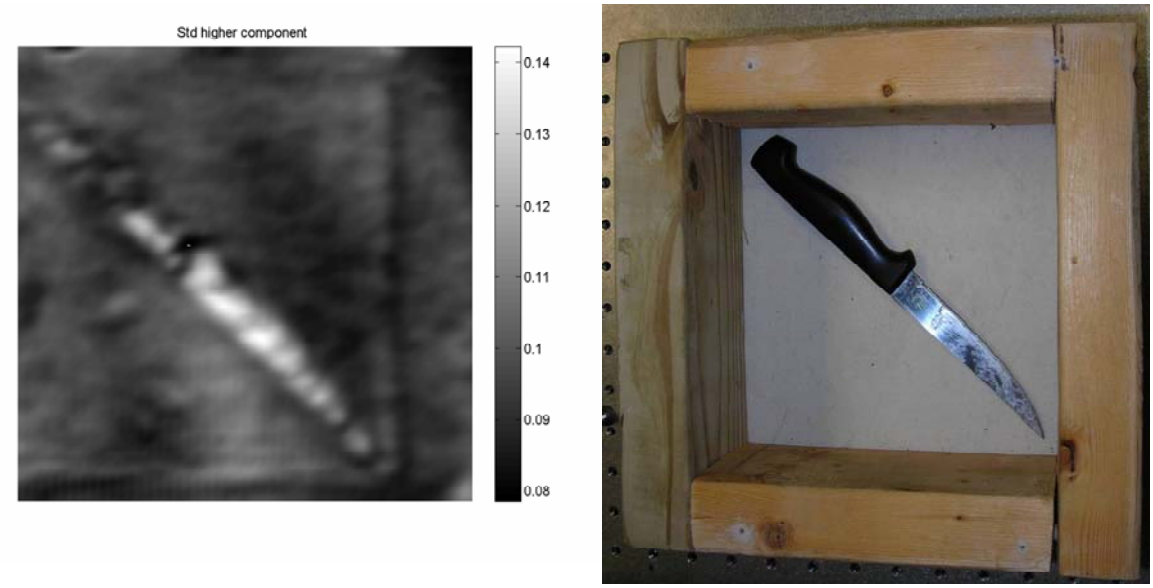

Figure 51: A kitchen knife imaged 7.3 cm behind one sheet of drywall, mmW higher component process image (left) and photograph (right).

A higher component process image of a plastic calculator with rubber numbers located 7.9 cm behind one sheet of drywall is shown in Figure 52. The plastic casing, rubber number keys, and the display panel are all identifiable in the image. The variety of materials reflect a different percentage of the mmW radiation, allowing like materials to be identified (the keys are brighter than the display which is brighter than the casing).

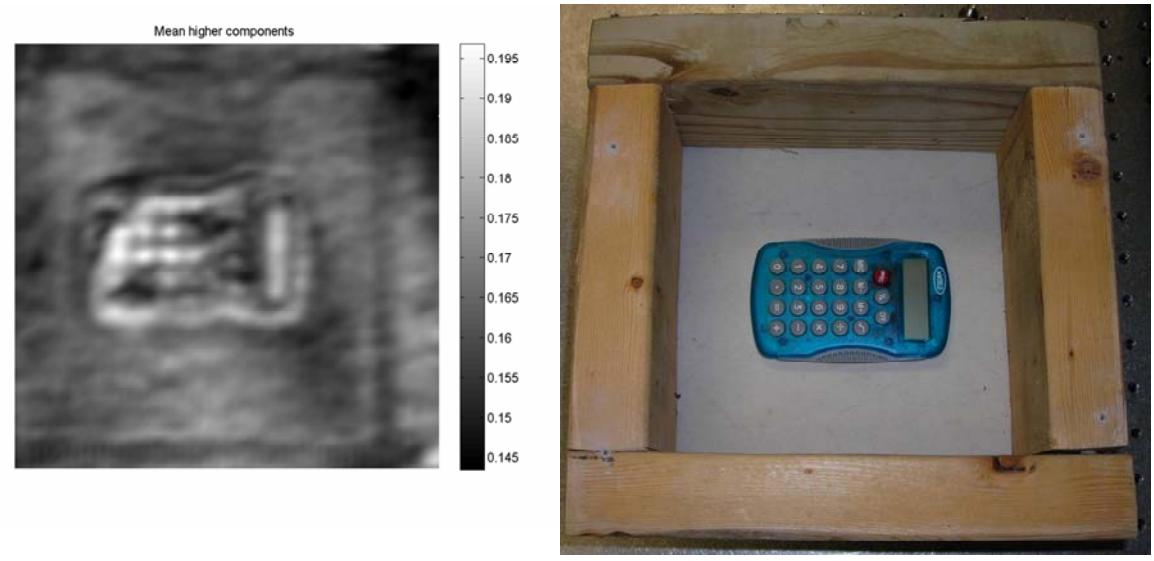

Figure 52: A calculator imaged 7.9 cm behind one sheet of drywall, mmW higher component process image (left) and photograph (right).

Figure 53 shows the mmW higher component process image of a metal handgun located 5.8 cm behind one sheet of drywall. The handgun is easily identified behind the drywall. Details in the image regarding the barrel, handle, trigger, and cylinder could allow the classification of the gun to be determined.

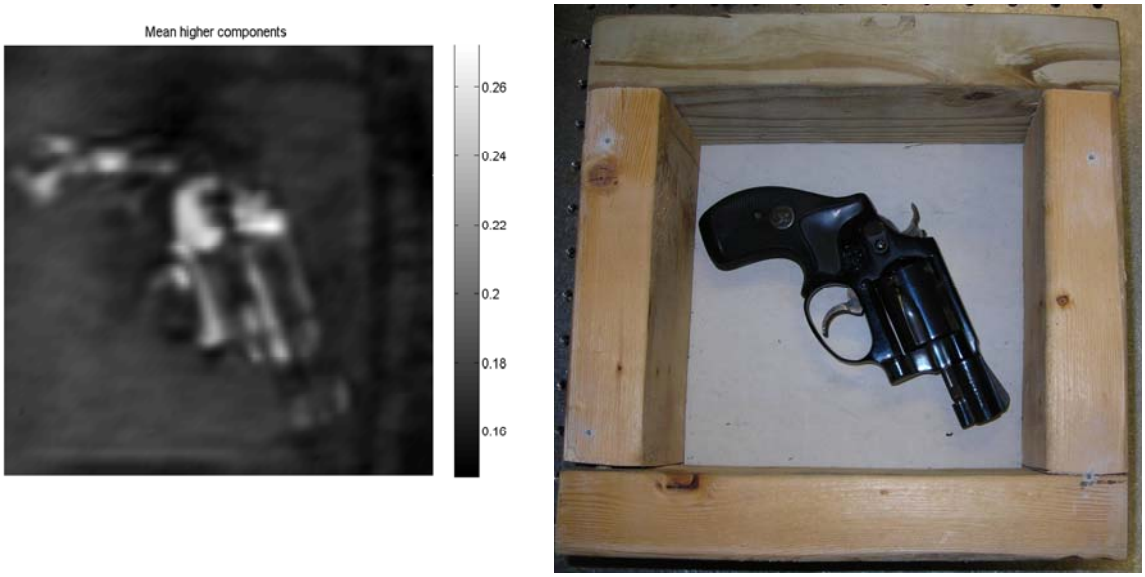

Figure 53: A metal pistol imaged 5.8 cm behind one sheet of drywall, mmW higher component process image (left) and photograph (right).

Imaging objects inside of a wall and imaging objects behind a wall create different challenges. Figure 54 shows the higher component process image of the metal handgun 30 cm behind the drywall. The handgun is detected and located behind the drywall. The image contains considerably less detail than in Figure 53. This is due to the Rayleigh criterion of resolution. The minimum resolvable separation between two points, δ, is given as

$$\delta = 1.22 \frac{\lambda d_i}{D_{exit}} \tag{24}$$

where λ is the wavelength, d_i is the image distance, and D_{exit} is the diameter of the exit pupil. The minimum resolvable separation for the setup used in Figure 53 with an image distance of 100 mm and an exit pupil diameter of 50.8 mm is between 8.0 mm (λ=3.33 mm) and 5.1 mm (λ=2.14 mm). Changing the image distance to 30 cm, as in Figure 54, the minimum resolvable

separation is between 24.0 mm (λ=3.33 mm) and 15.4 mm (λ=2.14 mm). This causes the small features of the handgun to not be resolved in the image. The resolution of the image located 300 mm from the lens would equal the resolution of the image located 100 mm from the lens by increasing the size of the lens (exit pupil) to 152.4 mm (3 times larger).

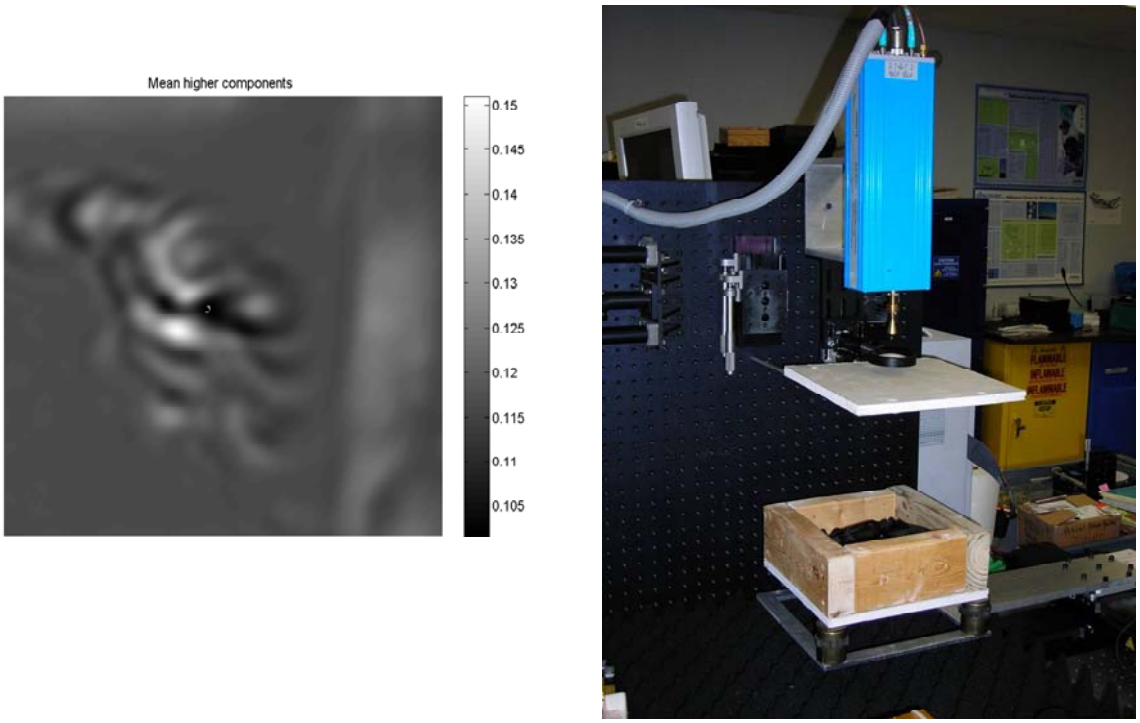

Figure 54: Metal pistol 30 cm behind drywall, mmW higher component process image (left) and photograph of setup (right).

Multiple images were taken of the metal handgun located beneath 1, 2, and 3 sheets of drywall, corresponding to 12.7 mm (0.5”), 25.4 mm (1”), and 38.1 mm (1.5”) thick and analyzed using the PCA method. These higher component process images are shown in Figure 55. The mmW signal gets attenuated further as each layer of drywall is added. The higher component process image of the handgun located behind 38.1 mm of drywall shows little detail of the handgun, but

the object is still detected and located. An increase of power would allow for a higher penetration depth to be obtained through the drywall.

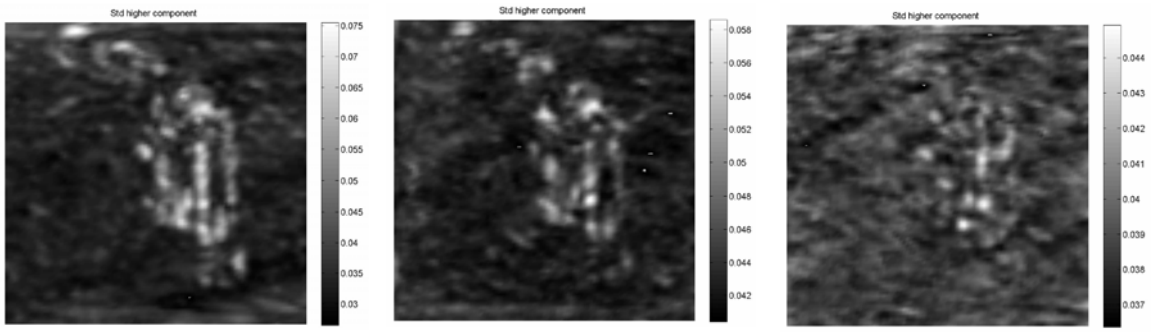

Figure 55: mmW higher component process image of a handgun located behind 12.7 mm, 25.4 mm, and 38.1 mm of drywall.

A mmW imager would also be useful if the contents of a box or envelope are needed without opening them. Figure 56 shows the mmW lowest order components process image of a kitchen knife located inside of a Jiffylite envelope. This envelope contains a bubble wrap lining. The knife is clearly seen through the packing material. The plastic handle is also seen in the image.

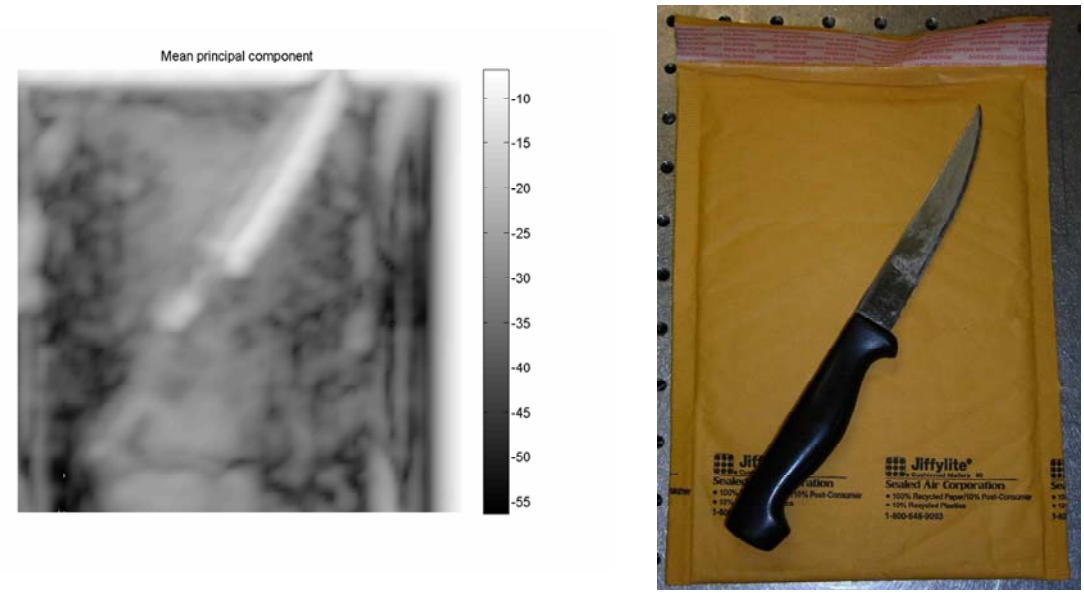

Figure 56: Kitchen knife inside of an envelope, mmW lowest order components process image (left) and photograph (right).

Discussion

A 90-140 GHz mmW imaging system was used to detect and identify objects located behind drywall and packing envelopes. The principal component analysis method was applied to the 51 frames to help locate the objects beneath the drywall. Objects made of metal, plastic, and rubber were located in the images. The handgun was detected 30 cm behind a sheet of drywall. As the thickness of the drywall increased, the return from the handgun decreased. The handgun could still be detected through three layers of drywall. An increase in power would be needed to further penetrate this depth of drywall. With increased power and aperture size, the detection of objects behind barriers is promising in the 90-140 GHz range.

CHAPTER 8: COMPACT MMW IMAGING SYSTEM

The previous chapters have shown many ways that a mmW imaging system can be utilized for different applications. Many of these applications require the system to be portable. The important factors when designing a compact system are size, weight, and power. The compact system is equipped with three Gunn oscillators with voltage regulators, a power supply, an electromechanical switch, a horn antenna, and a waveguide detector, shown in Figure 57.

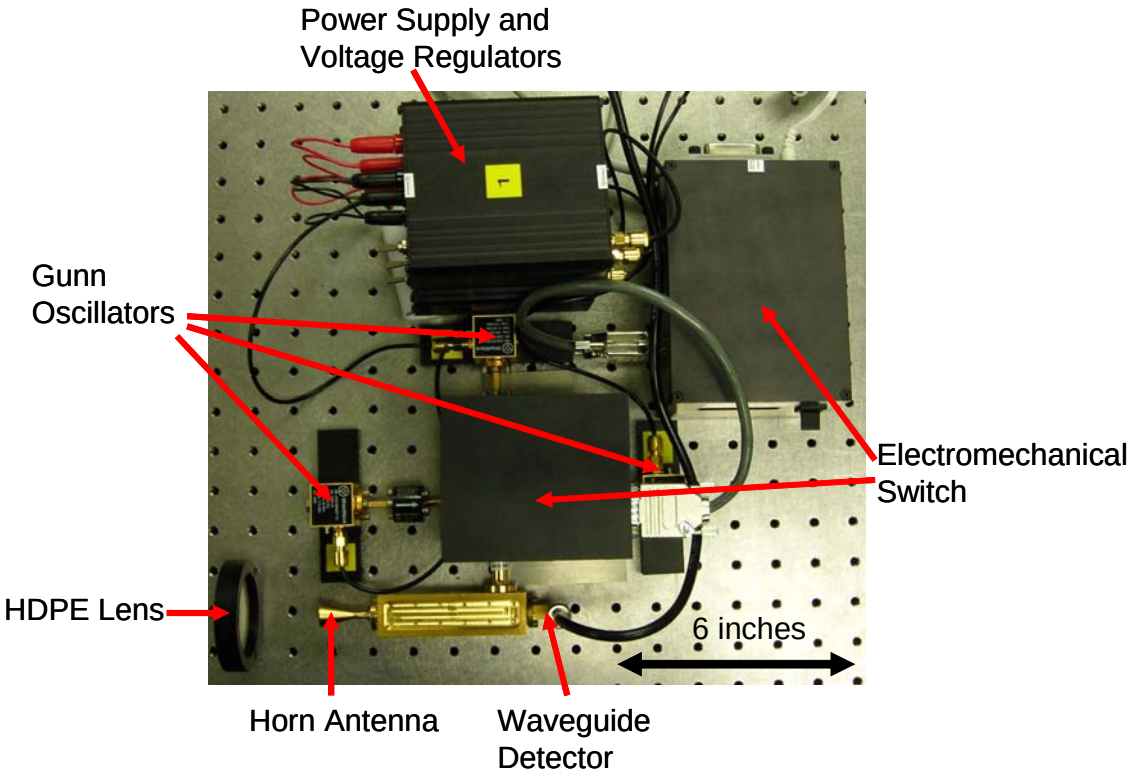

Figure 57: Compact mmW imaging System

This system is much smaller and lighter than the VNA system. Spread out on the optical bench the compact system only takes up about one square foot. Once the system is fitted into a box the

dimensions should decrease further. The frequencies of the Gunn oscillators are 94 GHz, 100 GHz, and 140 GHz. The 94 GHz and 140 GHz sources fall into the high transmission windows in the mmW range, shown in Figure 1 of the first chapter. The choice of three frequencies allows the weight to remain low while still providing multiple images for the PCA method to be applied. The Gunn oscillators have an output power around 50 mW which is much higher than the 2.5 mW output power of the VNA. The three frequencies are alternated using an electromechanical switch. The entire system operates off of a 12 V, 1 A power supply. A scanning system is needed in conjunction with the compact system, since translation stages are not practical for field work. A scanning lens is being developed for the system, shown in Figure 58. The scan lens will consist of a HDPE lens and two mirrors attached to galvanometers.

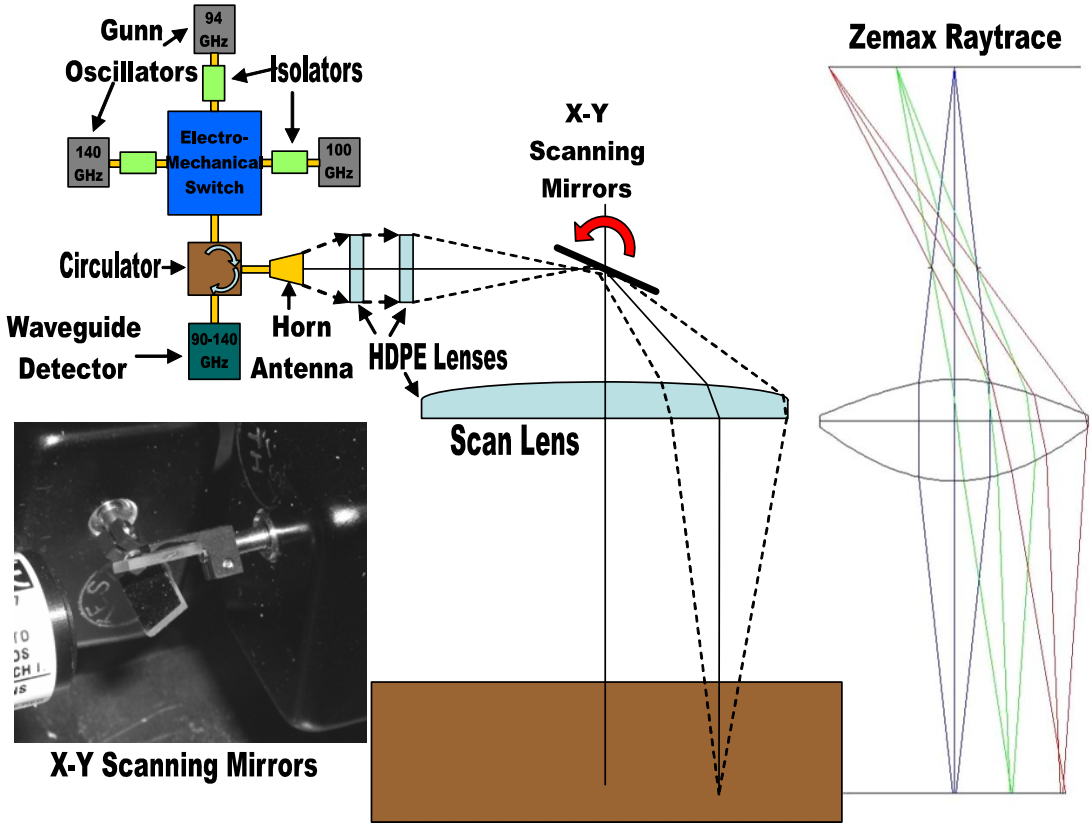

Figure 58: Schematic of the compact system equipped with the scan lens. The X-Y scanning mirrors will scan the radiation across the lens to capture a frame. Photograph of the X-Y scanning mirrors (bottom left). Zemax raytrace of the HDPE lens (right).

The mirrors will scan the beam through the larger HDPE focusing lens instead of the entire system moving in a raster scan pattern. This will produce faster images using the compact system. The HDPE scan lens will be 305 mm in diameter to provide a large scan area for the 127 mm diameter raster beam. The lens will be 50 mm thick at the center. The focal length of the lens will be 600 mm. The scan lens would have a diffraction blur of 0.058 rad, which is far greater than the aberration blur from spherical aberration (0.0006 rad), sagittal coma (0.00008 rad), and astigmatism (0.0012 rad).

The compact system is smaller, lighter, and consumes less power than our VNA mmW imager. The portability of the system will allow for faster on-site mmW images to be taken through soil, drywall, or other materials.

CHAPTER 9: FAR-INFRARED BRAGG MIRROR DESIGN

Introduction

There is a high need for the development of far-infrared sources and components in order to produce far-infrared systems. With far-infrared sources and components, potential applications such as concealed weapon detection, wireless communication, medical imaging, landmine detection, earth remote sensing, satellite based astronomy, biological and chemical weapon detection, explosive detection, night vision, and composite inspection can be realized.

In the visible and near IR, high reflectivity mirrors are fabricated from multiple dielectric layers, typically formed from glassy materials such as SiO_2, TiO_2, ZrO_2, and ThF_4. However, such materials, and most other glasses and polymers, will not work in the far-IR due to high absorption loss. Moreover, homogeneous metal films that are thick enough to provide high reflectivity have loss due to free carrier absorption, which increases as the square of the wavelength.

This chapter describes high-reflectivity mirrors formed from alternating layers of silicon separated by empty gaps [68]. Silicon has high far-IR transparency in the region 10-1000 μm, except in relatively narrow bands where phonon absorption occurs. Intracavity laser absorption measurements, with up to 3 cm of silicon placed inside the cavity of a p-Ge laser at 4 K operating temperature, show negligible effect on the laser thresholds at ~100 μm wavelengths

[69]. Since gain of the p-Ge laser is usually less than ~0.1 cm^{-1} [70], while active crystal lengths are usually several cm, the absorption coefficient of the passive Si crystal at cryogenic temperatures is therefore much less than 0.1 cm^{-1}. At room temperature, Si phonon absorption amounts to approximately 0.01 cm^{-1} at wavelengths longer than 50 μm [71]. Free carrier absorption losses for intrinsic Si at room temperature are also about 0.01 cm^{-1} [71]. Both types of absorption are strongly reduced when the Si crystal is cooled to liquid helium temperatures.

Because of the large difference in index of refraction between silicon (3.384) and vacuum, air, or helium (1), just three periods in the multi-layer Bragg mirror produce 99.9% reflectivity. The principle was independently suggested and tested recently [72], although accurate measurement of the achieved reflectivity was lacking. This chapter presents results of a test using a three-period Si-gap stack as a cavity mirror for the far-infrared p-Ge laser and a one or two period Si-gap stack as mirrors in a scanning Fabry-Perot filter using a THz gas laser at 134.00 μm. The low gain of this laser medium (0.01-0.1 cm^{-1}) puts high demands on mirror reflectivity. By comparing observed laser thresholds with that obtained using a traditional mirror, a qualitative indication of achieved mirror reflectivity is determined. Also, the finesse of the scanning Fabry-Perot filter equipped with the multilayer Bragg mirrors gives the measured mirror reflectivity.

Theoretical Considerations

Multi-layer Bragg mirrors are assembled by stacking alternating thin films of different refractive index and appropriate thickness. The reflectivity, *R*, of the Bragg mirror is determined from the standard matrix formulation of the boundary conditions at the film interfaces found from Maxwell's equations [73]. The amplitude of the reflection coefficient, *r*, of the Bragg mirror is given as,

$$r = \frac{\eta_m \vec{E}_m - \vec{H}_m}{\eta_m \vec{E}_m + \vec{H}_m} \tag{25}$$

where

$$\begin{pmatrix} \vec{E}_m \\ \vec{H}_m \end{pmatrix} = \vec{M} \begin{pmatrix} 1 \\ \eta_s \end{pmatrix} \tag{26}$$

$\vec{E}_m$ is the electric vector, $\vec{H}_m$ is the magnetic vector, η_m is the effective refractive index of the incident medium, η_s is the refractive index of the medium behind the mirror, and $\vec{M}$ is the product matrix of *q* layers given by

$$\vec{M} = \vec{M}_q \vec{M}_{q-1} \cdots \vec{M}_j \cdots \vec{M}_2 \vec{M}_1 \tag{27}$$

where $\vec{M}_j$ represents the *j*th layer of the Bragg mirror given by

$$\vec{M}_j = \begin{pmatrix} m_{11} & im_{12} \\ im_{21} & m_{22} \end{pmatrix} = \begin{pmatrix} \cos\delta_j & \frac{i}{\eta_j}\sin\delta_j \\ i\eta_j \sin\delta_j & \cos\delta_j \end{pmatrix} \tag{28}$$

where

$$\delta_j = \frac{2\pi}{\lambda}\left(n_j d_j \cos\theta_j\right) \tag{29}$$

and where λ is the wavelength of the light and $n_j d_j \cos\theta_j$ is the optical thickness of the j^{th} layer for the angle of refraction θ_j. If the light waves are at normal incidence, then $\theta_j = 0$. In this case, $\eta_j = n_j - ik_j$ where n_j is the index of refraction of the medium and k_j is the extinction coefficient of the medium.

The reflectivity, *R*, is then given as

$$R = |r|^2 \tag{30}$$

A complex index of refraction is assumed. The real part of the refractive index of silicon at 4 K and 100 μm wavelength [36] is 3.384. The extinction coefficient of Si was taken to be 2.5 x 10^{-5} based on an upper bound estimate of 0.01 cm^{-1} for the absorption coefficient [71]. The refractive index of vacuum is unity.

A preliminary multi-layer mirror was designed to serve as a cavity mirror for the p-Ge laser. The wavelength for peak *R* was chosen to be 110.5 μm, which corresponds to a region of relatively high transmission in the water vapor spectrum [74]. This mirror is composed of just 3 periods of silicon and vacuum gaps (Figure 59). The thickness of each layer is a multiple of the quarter wavelength of the light ($\lambda/4$) in the material. The Si layer thickness is 24.5 μm and the gap thickness is 27.6 μm. In the calculations, the incident medium was taken to be Ge (index of

refraction of 3.925 at 4 K and 100 μm wavelength [36]) and the medium behind the mirror is vacuum. Small 27.6 μm pieces of Si used as spacers determine the air layer thickness and ensure parallelism. The calculated reflectivity of the mirror is plotted vs. wavelength in Figure 59 over the operating range of the p-Ge laser. The maximum reflectivity for the three-period Bragg mirror is over 99.9%. Adding a fourth period increases the reflectivity to 99.99%.

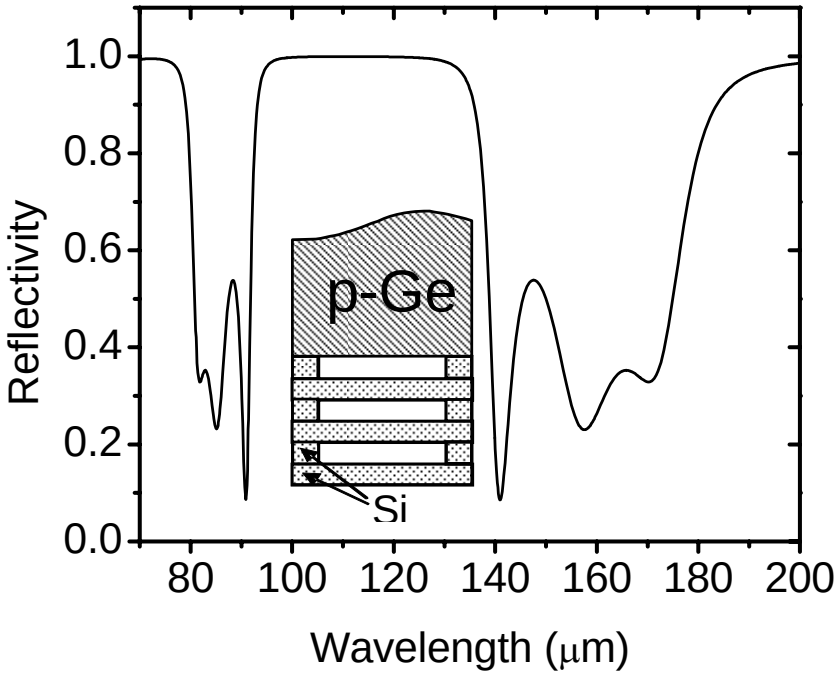

Figure 59: Reflectivity (solid curve) of a three-period Bragg mirror in the emission wavelength range of the p-Ge laser with a Si layer thickness of 24.5 μm and a gap layer thickness of 27.6 μm. A maximum reflectivity of 99.93% is achieved. (Inset) Schematic drawing of the 3 period Bragg mirror based on silicon/vacuum layers attached to the end face of a active p-Ge laser crystal.

The tolerance on absolute thickness specified by the manufacturer of the Si etalons used in the experiments (see below) is ± 3 μm. Figure 60 presents the calculated central reflection peak for various combinations of the silicon and gap thicknesses that have been changed by ± 3 μm from

the original design. The band of high reflectivity shifts by up to 20 μm as a result of these changes. Changing the thickness of the silicon has a larger effect than changing the gap thickness because the wavelength in the semiconductor is much smaller.

Figure 60 also presents a vertically expanded view of the central reflection peaks. Changing the gap and Si thickness simultaneously by 3 μm maintains the peak *R* at the level 99.93%, but shifts the peak by 13 μm. The worst R-value is still at the level 99.91%. The peak R-value changes by less than 0.023%. As noted, varying the Si thickness has larger effect on wavelength position and R-value than does varying the gap thickness.

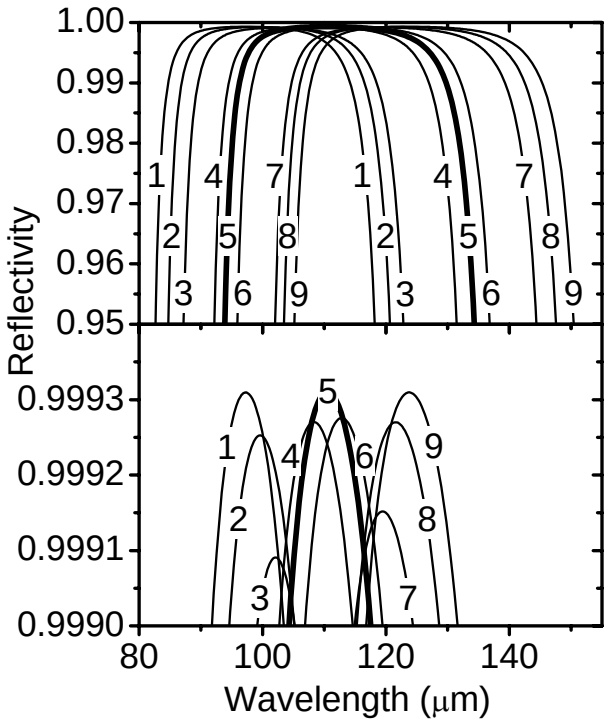

Figure 60: Central high reflectivity band for a three-period Bragg mirror in the emission wavelength range of the p-Ge laser. The (Gap, Si) thicknesses in μm are as follows (1) (24.6, 21.5); (2) (27.6, 21.5); (3) (30.6, 21.5); (4) (24.6, 24.5); (5) (27.6, 24.5) (6) (30.6, 24.5); (7) (24.6, 27.5); (8) (27.6, 27.5); (9) (30.6, 27.5).

Because extremely thin silicon etalons are expensive, fragile, and difficult to manipulate, there is reason to consider the consequences using thicker stock. The calculated maximum reflectivity of a 3-period Bragg mirror constructed with a gap thickness of 25 μm and the Si layer thickness between 10 and 100 μm thick is shown in Figure 61 (bottom, solid curve). A consequence of increasing the etalon thickness is that the band with high reflectivity becomes narrower. Figure 61 (bottom, dashed curve) shows that the full width at half maximum (FWHM) of the broadest high-reflectivity band, for the 3-period Bragg mirror constructed with the 25 μm gap thickness, tends to decrease as the Si layer thickness is increased. Even for quite thick Si, the FWHM remains ~30 μm wide, which suggests that the corresponding mirror would still be useful in applications requiring broad wavelength tuning. The number of bands with reflectivity above 95% in the 70-200 μm wavelength range increases from 1 (see Figure 59) to 7 as the thickness of each Si layer increases from 10 to 100 μm. The center wavelengths of the bands with maximum R-value above 95% are shown in Figure 61 as the Si layer thickness is increased in steps of 1 μm. The band with highest R-value is represented as a solid symbol. As the Si layer thickness is increased, the highest R-value does not remain with the same band as it shifts to longer wavelength, but rather jumps to the next band emerging from the low wavelength border into the considered range. The band with highest R-value tends to be the one with its center closest to 100 μm wavelength, for which the 25 μm gap is one-quarter wavelength.

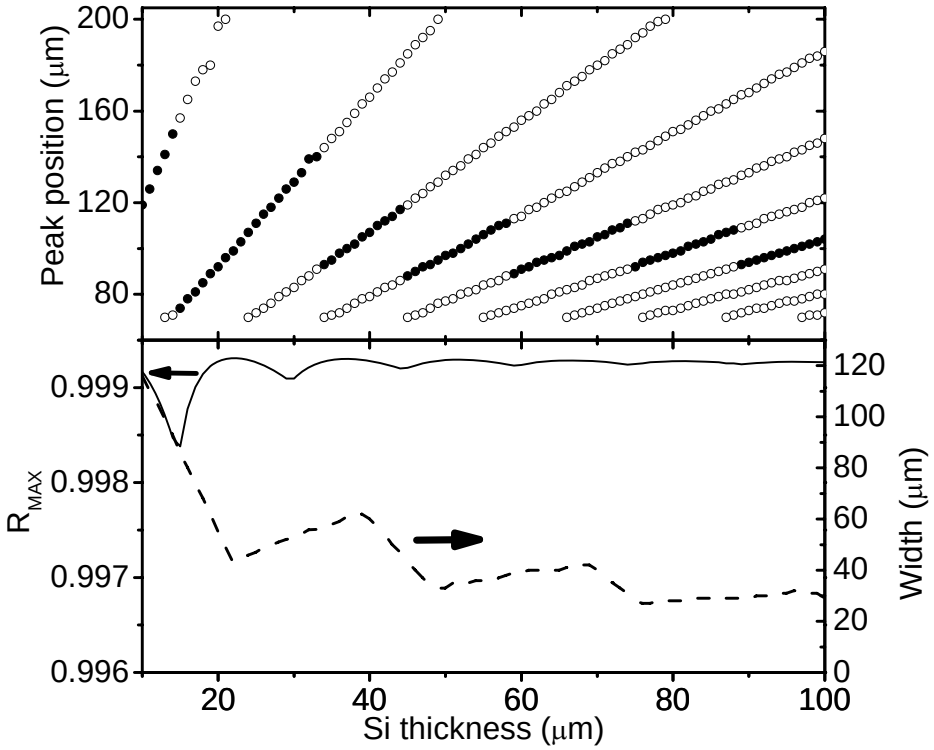

Figure 61: (Top) Center wavelengths of bands with peak reflectivity above 95% for fixed 25 μm gap and variable Si thickness in three-layer Bragg mirror. Solid symbols indicate the band with highest reflectivity. (Bottom, solid curve) Maximum value of reflectivity. (Bottom, dashed curve) Full width at half maximum of the band with highest reflectivity.

Calculations were also made for a 3-period Bragg mirror constructed with a fixed 25 μm Si layer thickness and a gap thickness that varies over the range 10-100 μm. The calculated maximum reflectivity is plotted in Figure 62 (lower, solid curve) and its value exceeds 99.7% for most of the range of gap thickness considered. Figure 62 (lower, dashed curve) shows that the FWHM of the broadest high-reflectivity band remains at least 25 μm, so that quite crude mirror structures remain valuable for applications that require broad wavelength tuning. The number of bands with reflectivity above 95% within the 70-200 μm wavelength range does not exceed 3 over the range of gap thickness considered. Their positions with reflectivity above 95% are plotted in

Figure 62 (upper). The band with highest R-value is again represented by solid symbols. As the gap thickness is increased, the maximum R-value jumps between the different bands, and it does not stay centered near a single wavelength. Note, that high-R values are absent for wavelengths beyond 150 μm with this type of construction.

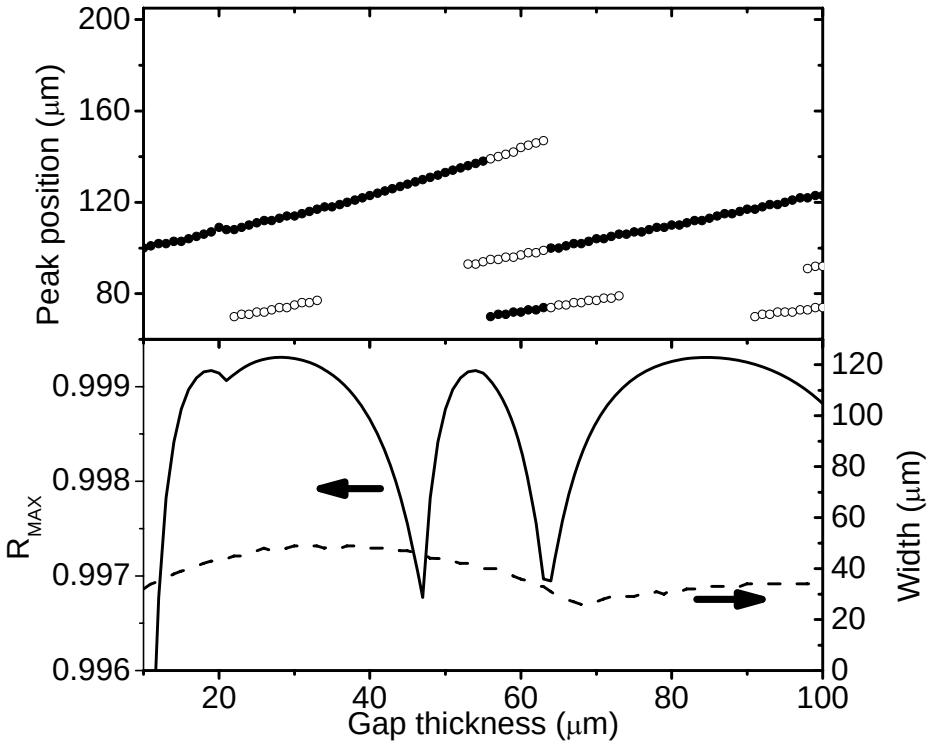

Figure 62: (Top) Center wavelength of bands with peak reflectivity above 95% for fixed Si layer thickness and variable gap thickness. Solid symbols indicate the band with highest reflectivity. (Bottom, solid curve) Maximum value of reflectivity. (Bottom, dashed curve) Full width at half maximum of the band with highest reflectivity.

It is more convenient and less expensive to construct Bragg mirrors of the type shown in Figure 59 if both the Si etalon and the gap (formed from Si spacers) are the same thickness. In this case, all required pieces, both etalons and spacers, may be cut from the same wafer. The maximum reflectivity for such 3-period Bragg mirrors is plotted vs. layer thickness in Figure 63 (lower,

solid curve). The reflectivity almost always exceeds 99.9%. A vertical line at 105 μm is drawn to indicate the thickness used in the experiments in the next section. The FWHM of the broadest high-reflectivity band in the 70-200 μm wavelength range, plotted in Figure 63 (lower, dashed curve), tends to decrease as the layer thickness increases. However, the width always exceeds ~15 μm showing that such mirrors remain useful for applications that require broad wavelength tuning. The number of bands with reflectivity above 95% increases as the layer thickness increases. The positions of bands with R-values above 95% are plotted in Figure 63 (upper). The band with largest R-value is again represented by solid symbols. The preceding calculations indicate that for use as a cavity mirror in a p-Ge laser, whose gain bandwidth spans the 70-200 μm wavelength range, precise tolerances for Si or gap thickness are not essential.

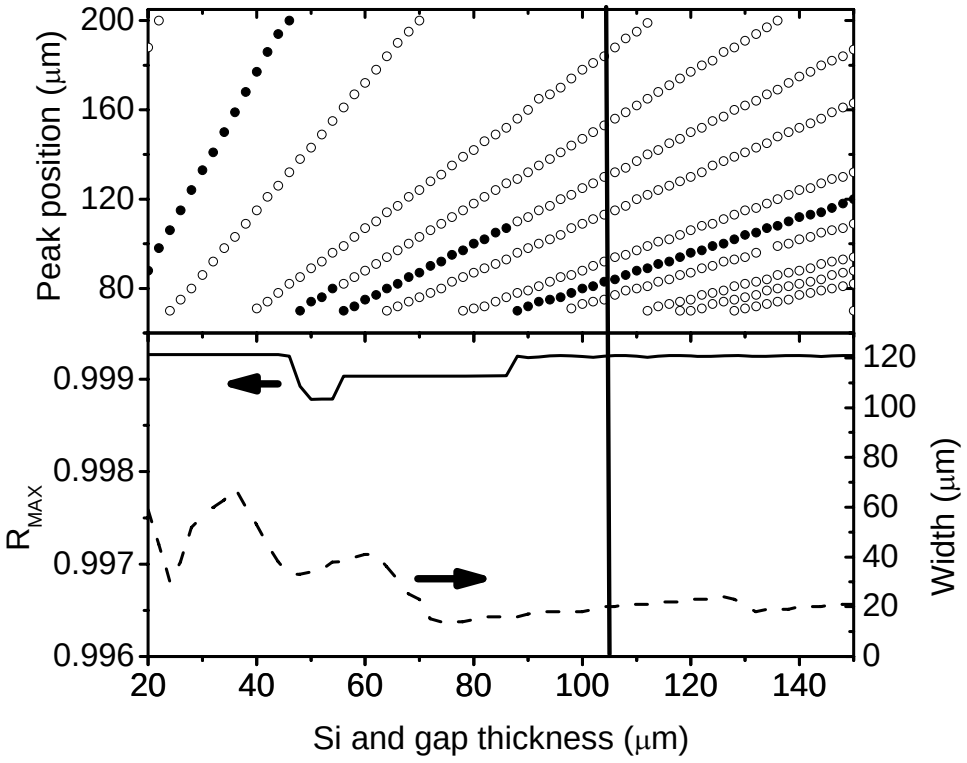

Figure 63: (Top) Center wavelength of bands with reflectivity above 95% vs. Si and gap thickness, which are the same. Solid symbols denote the band with the highest reflectivity. (Bottom, solid curve) Maximum value of reflectivity. (Bottom, dashed curve) Full width at half maximum for the band with highest reflectivity. The vertical line indicates the parameters for Bragg mirror B.

p-Ge Laser Bragg Mirror

Multi-layer mirrors were constructed for the p-Ge laser cavity. High purity silicon wafers were obtained from Valley Design. High resistivity, specified to exceed 4000 ohm-cm, was chosen in order to minimize free carrier absorption. Wafers were double side polished and parallel within 10 arc seconds, which is sufficient to prevent beam walk-off from the laser cavity during the 1 μs laser pulse. The specified silicon thickness was 24.5 ± 3 μm and the gap thickness was 27.6 ± 3

μm for Bragg mirror A. The parallel gaps are produced using small 27.6 μm pieces of silicon as spacers. Wafer thicknesses were measured using a precision dial indicator (Starrett F2730-0) to be 25 ± 1 μm for the Si layer and 29 ± 1 μm for the gap spacers. These measurements indicate that curve 5 of Figure 61 corresponds most closely to our actual experimental situation. Bragg mirror B is constructed using 105 ± 1 μm Si etalons for both the Si layers and the gap spacers, which corresponds to the configuration indicated by the vertical line in Figure 63.

The multi-layer mirrors are tested as cavity back mirrors for the p-Ge laser. The silicon pieces are stacked layer by layer onto the p-Ge crystal end face. After the six alternating layers are constructed, a brass washer is placed on top of Bragg mirror A with a rubber string attaching the whole structure in place on the crystal, shown in Figure 64. Bragg mirror B was stacked onto the p-Ge laser and held into place using a bronze spring. A $SrTiO_3$ mirror, smaller than the crystal end face to allow radiation output, is attached to the other end face of the crystal [68]. The active Ga-doped Ge (N_A~$7x10^{13}$ cm^{-3}) crystal has dimensions 35.20 mm × 4.75 mm × 6.75 mm for Bragg mirror A and 45.45 mm × 6.0 mm × 2.5 mm for Bragg mirror B. The crystal ends were polished flat and parallel within 30 arc seconds. The electric field was generated in the crystal by applying voltage using a thyratron pulser to ohmic contacts. The magnetic field was supplied by a superconducting solenoid. A liquid-helium cooled Ge:Ga photoconductor inside the cryostat detects the radiation.

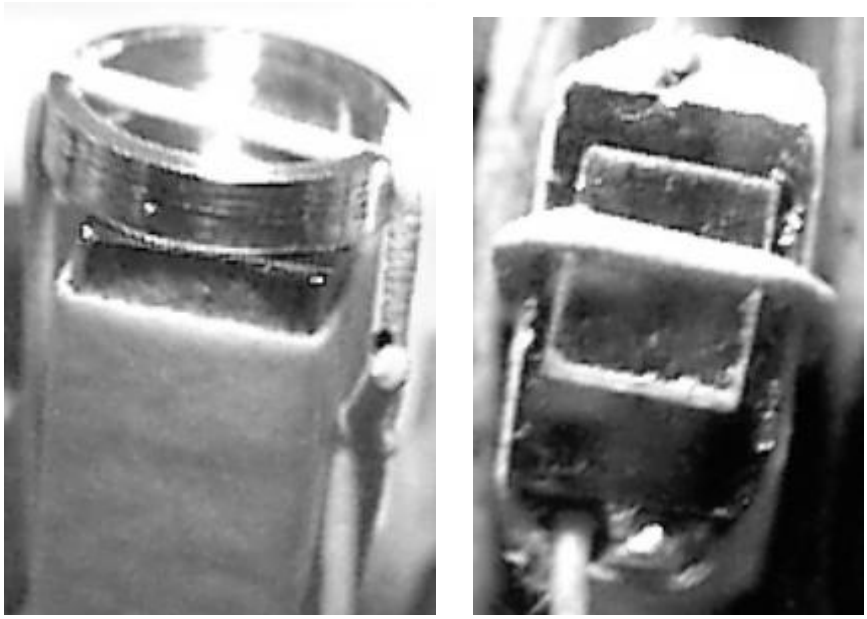

Figure 64: (left) Photograph of the Bragg mirror on the end of a p-Ge laser crystal held in place with a brass washer and a rubber string. Wires providing the electric field to the ohmic contacts are on the lateral sides of the crystal.

Lasing is observed using both mirrors A and B. The laser operation zones, i.e. the applied electric and magnetic fields for which the laser operates, were recorded for the different end mirrors. Figure 65 presents the laser operation zones using Bragg mirrors A and B in the space of applied **E** and **B** fields compared to that of a $SrTiO_3$ end mirror. The electric and magnetic field thresholds are higher for B than for A. Both mirrors have higher thresholds than found using a $SrTiO_3$ back mirror.

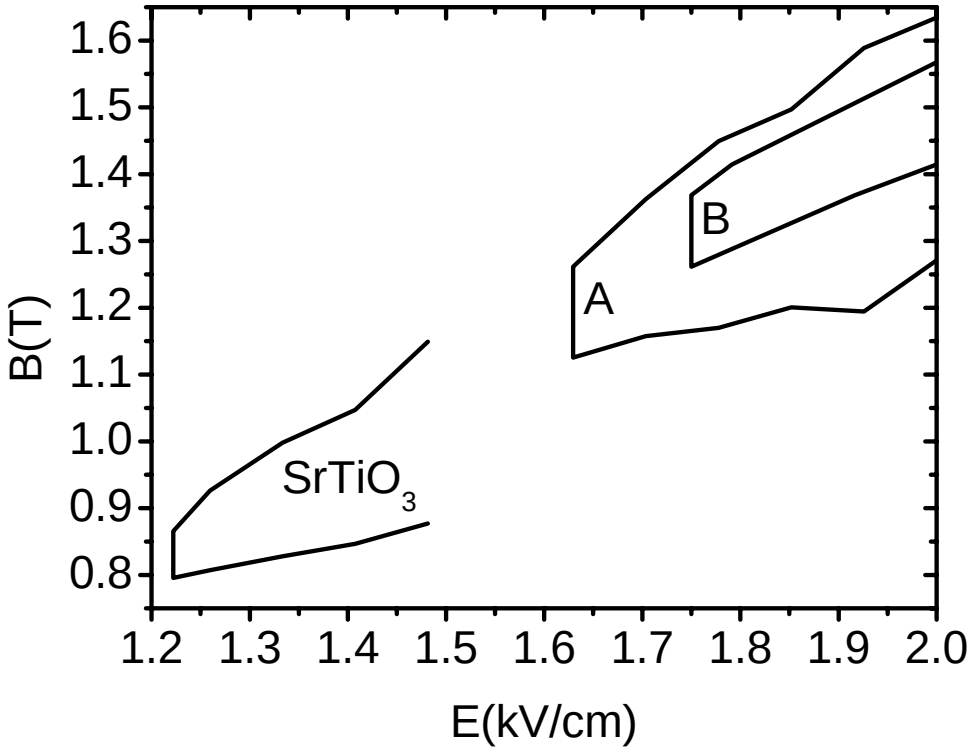

Figure 65: Comparison of the laser generation zones for the p-Ge laser using two different Bragg mirrors or $SrTiO_3$ mirror. Bragg mirror A is constructed with 29 μm gap layer thickness and 25 μm Si layer thickness. Bragg mirror B is constructed with 105 μm Si and gap layer thickness.

p-Ge Laser Bragg Mirror Reflectivity

Figure 65 is an experimental demonstration that a Si/gap multi-layer Bragg mirror has sufficient reflection for use with the low gain, far-infrared p-Ge laser. The mirror reflectivity R must satisfy the condition

$$R \geq e^{-2\alpha L_{Ge}}, \tag{31}$$

where α is the gain and L_{Ge} is the length of the Ge laser cavity. Using 0.01 cm^{-1} as the value for the gain of a p-Ge laser and 3.52 cm for the length of the laser crystal, the minimum reflectivity for a laser mirror is $R_{min} \sim 93\%$. Output coupling losses require the reflectivity to be better than 93%. $SrTiO_3$ has a reflectivity of ~99% at 20 K in this wavelength region [21], though this R-value should increase as the mirror temperature decreases to 4 K. The higher thresholds for the Bragg mirrors therefore suggest that their reflectivity is somewhat lower than 99%. Hence, while these experiments bracket the reflectivity of the Bragg mirror in the range 93-99%, they fail to definitely comfirm the predicted 99.9% value. Bragg mirror B has a higher threshold than mirror A, in agreement with calculations (Figure 60 and Figure 63) which suggest narrower bands of high reflectivity for the thicker layered structure. Nevertheless, the laser operation using Bragg mirror B shows that a highly reflective mirror can be constructed using layers of equal thickness that are much larger than a quarter wavelength.

As an explanation for the high thresholds using the Bragg mirrors despite their high calculated reflectivity, we note that the brass washer and Si spacers for the stack overlap portions of the active-crystal end face that might support laser modes. Such regions of the mirror lack the calculated high reflectivity. A more monolithic construction could be made by wet chemical etching to produce the gaps [22], eliminating the need for the small silicon spacers. Nevertheless, the preliminary experiments described here demonstrate that mirrors of sufficient reflectivity for use in the cavity of the low-gain p-Ge laser can be made with just a few layers of Si separated by empty gaps. Furthermore, high design precision does not appear to be critical.

Scanning Fabry-Perot Filter

A Fabry-Perot scanning spectrometer is an extremely narrow-band tunable filter. If the finesse is high, narrow band width can be achieved simultaneously with a high free spectral range, for chemical sensing and astrophysical spectroscopy applications. The foundation for a scanning Fabry-Perot spectrometer is the development of a scanning Fabry-Perot transmission filter. The following research was done in conjunction with the master's thesis work of Justin Cleary in the physics department at the University of Central Florida.

The scanning Fabry-Perot transmission filter [75] is composed of two parallel mirrors. One of the mirrors is fixed as the other moves on a motorized translation stage. In this work Bragg mirrors were used, and these were fabricated using Si wafers separated by small mylar pieces creating an air gap. The Si thickness was 10 μm and the air gap thickness was 50 μm. The Bragg stacks were attached on the outer edge using rubber cement. The two Bragg mirrors were aligned while observing transmittance resonances as the distance between the mirrors changed. The optical mounts were adjusted until the sharpness of the transmittance measurements was maximized. A coherent DEOS gas laser chopped at 20 Hz at the 134.00 μm laser line was used. The transmitted signal was detected using a Golay cell and a lock-in amplifier.

The finesse, *F*,of the Bragg mirrors is determined from the reflectivity, *R*, of the scanning Fabry-Perot transmission filter, according to

$$F = \frac{\pi\sqrt{R}}{1-R} \tag{32}$$

The cavity-Q (or resolving power $\frac{\lambda}{\Delta\lambda}$) is

$$Q = \frac{k(\lambda/2)}{\Delta d} = kF \tag{33}$$

where *k* is the resonance order, λ is the fixed wavelength, and Δd is the full-width at half-maximum of transmission maxima for the Fabry-Perot filter. The free spectral range is $\frac{\lambda}{k}$. Clearly, to achieve high free spectral range and Q simultaneously one needs high F, which requires high R.

Figure 66 presents experimental resonance data (solid curve) for a scanning Fabry-Perot cavity formed by a single Si layer. The finesse of the single period of Si is about 4. The predicted finesse is about a factor of 2 better than the experimental finesse, with a reflectivity of about 68%.

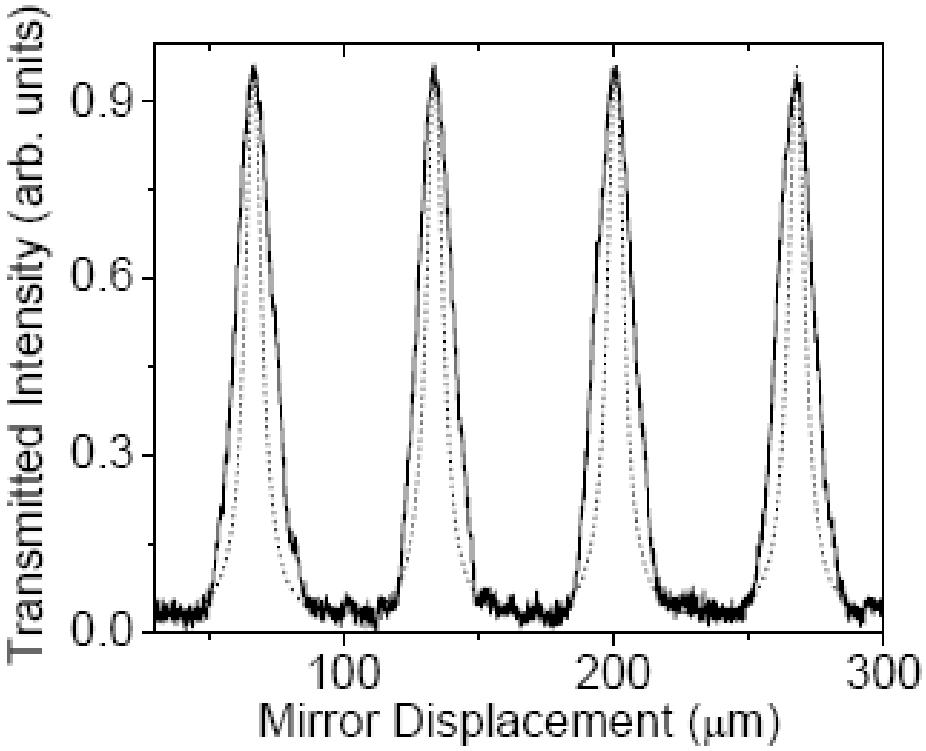

Figure 66: Experimental (solid) and theoretical (dotted) resonances for a single layer Bragg mirror scanning Fabry-Perot operating at 134.00 μm.

Figure 67 is experimental data obtained using two periods of the Si separated by the air gap. The addition of the second period increases the reflectivity of the Bragg mirrors. A sharpening of the resonances is seen compared to the one period mirror. The finesse of the two period Bragg mirror is about 6. The predicted finesse is about a factor of 14 better than the experimental finesse, with a reflectivity of about 96.3%. The disagreement between experiment and theory is due to technological factors such as poor alignment of the individual silicon layers within each Bragg mirror. These factors are discussed in detail in [76].

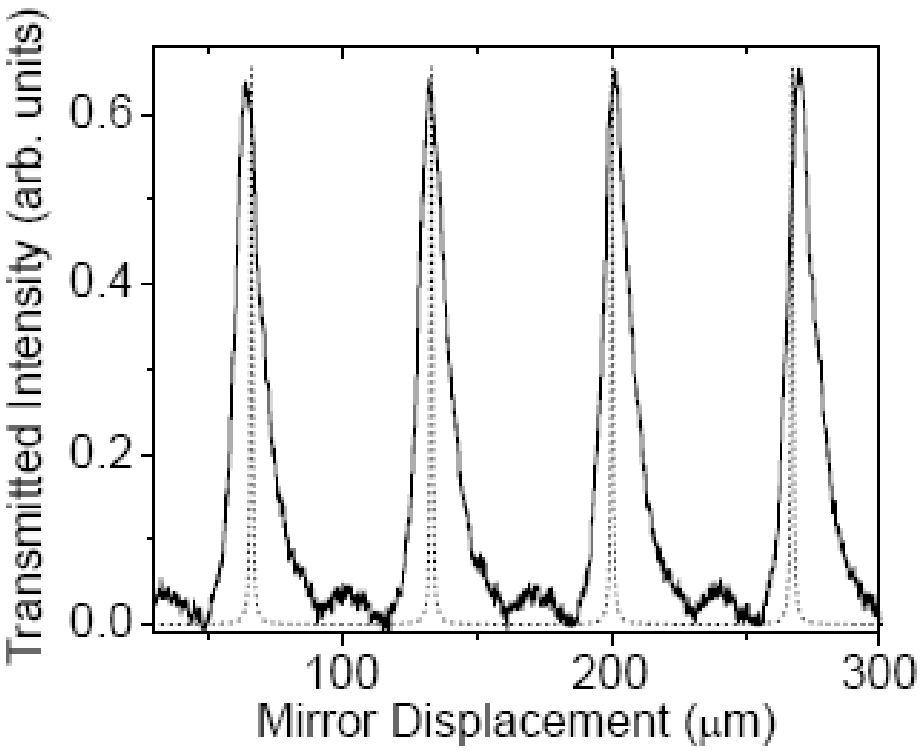

Figure 67: Experimental (solid) and theoretical (dotted) resonances for a two period Si Bragg mirror scanning Fabry-Perot operating at 134.00 μm.

The finesse of the Bragg mirrors increases as the number of periods increase, but the predicted finesse is well below the experimental results. Increasing the Bragg mirror to three periods should produce higher reflectivity mirrors. Again, a more monolithic construction could be made by wet chemical etching to produce the gaps [22], eliminating the need for the small spacers. This would reduce the inaccuracies in the construction of the Bragg mirrors, improving the finesse closer to the predicted value. Nevertheless, the experiments described here demonstrate that multi-layer mirrors of high reflectivity can be produced and measured in the THz spectral range.

CHAPTER 10: CONCLUSIONS

The far-infrared and mm-wave (75 μm to 10 mm) portions of the electromagnetic spectrum are fairly underdeveloped regions, lacking many useful sources, components, or proven applications. This dissertation research provided advancement in the development of sources, components, and systems in this region.

The transmission of many types of soil found throughout the world was measured over the 90-1500 GHz range. The high frequency range was dominated by a roll-off due to scattering, which correlates with particle size. The mmW range had high transmission for many of the studied soils. Organic materials and water were strong sources of attenuation. Saturation with index matching liquids reduces scattering and increases transmission at higher frequencies. A transparent low toxicity fluid with index of refraction closer to 2 would have great promise for use with terahertz imaging for mine detection.

A millimeter wave imaging system in the 90-140 GHz range was developed for the detection of plastic landmines, unexploded ordnance, objects behind barriers, and buried Mars rock. The final data set was a collection of mmW images at different frequencies. A signal processing method based on a Principal Component Analysis was applied to the images in order to separate different structures that help to identify the objects. The mmW imaging system and PCA method were successful as a means of locating and identifying the objects buried beneath the soil, drywall, and packing envelopes.

An increase in power would be needed to penetrate deeper into the soil and through thicker pieces of drywall. With increased power and aperture size, the detection of objects behind barriers is promising in the 90-140 GHz range.

A compact mmW imaging system was developed using three Gunn oscillators, a electromechanical switch, and a waveguide detector. The system is smaller, lighter, and consumes less power than our VNA mmW imager. A portable system will allow for faster on-site mmW images to be taken through soil, drywall, or other materials.

Finally, research was conducted on far-infrared sources and components. High-reflectivity far-infrared mirrors formed from thin silicon etalons separated by air gaps were developed as cavity mirrors for the p-Ge laser. The theoretical maximum reflectivity for the three-period Bragg mirror is over 99.9%. The multi-layer mirrors were tested as cavity back mirrors for the p-Ge laser. The reflectivity of the Bragg mirrors fall in the range 93-99%, probably below the predicted 99.9%. These mirrors could allow for narrow band selectivity of the broadband p-Ge source to be used in a far-infrared imaging system. In addition, the finesse of one and two period Bragg mirrors were measured using a scanning Fabry-Perot filter, THz gas laser, and a golay cell. The measured finesse was less than the theoretical predictions. However, the finesse increased as the number of Bragg periods increased as expected. Poor alignment of the alternating layers is probably responsible for the less than expected reflectivity. Three period Bragg mirrors used in a Fabry-Perot scanning spectrometer would serve as an extremely narrow-

band tunable filter, which simultaneously has a high free spectral range, for chemical sensing, earth remote sensing, and satellite far-infrared astronomy applications.

CHAPTER 11: FUTURE WORK

Future work on this project includes miniaturization of the mmW imaging system, in a form suitable for field testing. Also, an investigation of the transmission through alternate building materials needs to be conducted including plywood, house siding, tile, and insulation. This could increase the through barrier imaging capabilities of the system. Alternate signal processing techniques can be investigated to enhance the image quality. Finally, a spectrum of the p-Ge laser equipped with a Bragg mirror needs to be taken to determine the wavelength selection capabilities. Bragg mirrors with narrow high reflectivity bands can be developed for this purpose. Fabrication of the Bragg mirrors using wet chemical etching to produce the gaps, eliminating the need for the small spacers, should be done. This should reduce the losses caused by the current construction technique. Lastly, a far-infrared Fabry-Perot scanning spectrometer could be built using the high reflectivity Bragg mirrors.

LIST OF REFERENCES

1. J. Lesurf, “Sky Noise,” http://www.st-andrews.ac.uk/~jcgl/Scots_Guide/RadCom/part8/page3.html.
2. J. R. Pardo, J. Cernicharo, and E. Serabyn, “Atmospheric Transmission at Microwaves (ATM): An Improved Model for Millimeter/Submillimeter Applications” IEEE Trans. Antennas and Prop. **49** (12) 1683-1694 (2001).
3. A. F. Krupnov, M. Y. Tretyakov, V. V. Parshin, V. N. Shanin, and S. E. Myasnikova, “Modern Millimeter-Wave Resonator Spectroscopy of Broad Lines,” J. Mol. Spectr. **202**, 107-115 (2000).
4. M. Y. Tretakov, V. V. Parshin, M. A. Koshelev, A. P. Shkaev, A. F. Krupnov, “Extension of the range resonator scanning spectrometer into submillimeter band and some perspectives of its further developments,” J. Mol. Spectr. **238**, 91-97 (2006).
5. M. Y. Tretyakov, M. A. Koshelev, V. V. Dorovskikh, D. S. Makarov, P. W. Rosenkranz, “60-GHz oxygen band: precise broadening and central frequencies of fine-structure lines, absolute absorption profile at atmospheric pressure, and revision of mixing coefficients,” J. Mol. Spectr. **231**, 1-14 (2005).
6. M. van Exter, C. Fattinger, and D. Grischkowsky, “Terahertz time-domain spectroscopy of water vapor,” Opt. Letters **14** (20) 1128-1130 (1998).
7. T. Yuan, H. B. Liu, J. Z. Xu, F. Al-Douseri, H. Hu, and X. –C. Zhan, “THz time-domain spectroscopy of atmosphere with different humidity,” Proc. SPIE **5070**, 28-37 (2003).

8. Anritsu, “Primer on Vector Network Analysis,” Scorpion and Lightning Application Note No. 11410-00387 Rev. A, 1-8 (2006).
9. Anritsu, “ME7808B Broadband and Millimeter Wave VNA,” Anritsu Product Note 11410-00330 Rev. B, 1-12 (2006).
10. H. Eisele and R. Kamoua, “Submillimeter-Wave InP Gunn Devices,” IEEE Trans. Microwave Theory and Techn. **52** (10), 2371-2378 (2004).
11. H. Eisele and R. Kamoua, “High-Performance Oscillators and Power Combiners With InP Gunn Devices at 260-330 GHz,” IEEE Microwave and Wireless Letters **16** (5), 284-286 (2006).
12. H. Eisele, M. Naftaly, and R. Kamoua, “Generation of Submillimeter-Wave Radiation with GaAs Tunnett Diodes and InP Gunn Devices in a Second or Higher Harmonic Mode,” Inter. J. Infrared Millimeter Waves **26** (1), 1-14 (2005).
13. Wisewave, “Mechanically Tuned Gunn Diode Oscillators,” Wisewave Technologies Bulletin No. OGM, 5-4 (2004).
14. B. Gorshunov, A. Volkov, I. Spektor, A. Prokhorov, A. Mukhin, M. Dressel, S. Uchida, and A. Loidl, “Terahertz BWO-Spectroscopy,” Inter. J. Infrared Millimeter Waves **26** (9), 1217-1240 (2005).
15. C. P. Endres, H. S. P. Muller, S. Brunken, D. G. Paveliev, T. F. Giesen, S. Schlemmer, and F. Lewen, “High resolution rotation-inversion spectroscopy on doubly deuterated ammonia, ND_2H, up to 2.6 THz,” J. Mol. Structure **795**, 242-255 (2006).

16. A. Dobroiu, M. Yamashita, Y. N. Ohshima, Y. Morita, C. Otani, and K. Kawase, “Terahertz imaging system based on a backward-wave oscillator,” Appl. Optics **43** (30), 5637-5646 (2004).
17. Microtech Instruments “Compact THz Generators,” Microtech Instruments Catalog, 1 (2005).
18. A. W. M. Lee and Q. Hu, “Real-time, continuous-wave terahertz imaging by use of a microbolometer focal-plane array,” Optics Letters **30** (19), 2563-2565 (2005).
19. E. R. Mueller, “Optically-Pumped THz Laser Technology,” Coherent-DEOS product Note, 1-10 (2001).
20. E. Gornik and A. A. Andronov, “Special Issue – Far-Infrared Semiconductor-Lasers,” Optical and Quant. Elec. **23**, R5-R5 Sp. Iss. SI (1991).
21. T. W. Du Bosq, R. E. Peale, E. W. Nelson, A. V. Muravjov, C. J. Fredricksen, N. Tache, and D. B. Tanner, “Dielectric selective mirror for intracavity wavelength selection in far-infrared p-Ge lasers,” J. Appl. Phys. **94** (9), 5474-5478 (2003).
22. T. W. Du Bosq, R. E. Peale, E. W. Nelson, A. V. Muravjov, D. A. Walters, G. Subramanian, K. B. Sundaram, and C. J. Fredricksen, “Wavelength selection for the far-infrared p-Ge laser using etched silicon lamellar gratings,” Optics and Laser Tech. **37** (2), 87-91 (2005).
23. A. V. Muravjov, S. H. Withers, H. Weidner, R. C. Strijbos, S. G. Pavlov, V. N. Shastin, and R. E. Peale, “Single axial-mode selection in a far-infrared p-Ge laser,” Appl. Phys. Letters **76** (15), 1996-1998 (2000).
24. B. S. Williams, S. Kumar, Q. Hu, and J. L. Reno, “High-power terahertz quantum-cascade lasers,” Electronics Letters **42** (2), 90-91 (2006).

25. G. Scalari, L. Ajili, J. Faist, H. Beere, E. Linfield, D. Ritchie, and G. Davies, “Far-infrared (λ=87 μm) bound-to-continuum quantum-cascade lasers operating up to 90 K,” Appl. Phys. Letters **82** (19), 3165-3167 (2003).
26. S. Krishnagopal, and V. Kumar, “Free-electron lasers,” Radiation Phys. And Chem. **70**, 559-569 (2004).
27. V. S. Cherkassky, B. A. Knyazev, V. V. Kubarev, G. N. Kulipanov, G. L. Kuryshev, A. N. Matveenko, A. K. Petrov, V. M. Popik, M. A. Scheglov, O. A. Shevchenko, and N. A. Vinokurov, “Imaging techniques for a high-power THz free electron laser,” Nuclear Instr. And Methods in Phys. Research A **543**, 102-109 (2005).
28. G. P. Williams, “Filling the THz gap-high power sources and applications,” Rep. Prog. Phys. **69**, 301-326 (2006).
29. B. Ferguson and X.-C. Zhang, “Materials for Terahertz science and technology,” Nature Materials **1**, 26-33 (2002).
30. R. W. McMillan, “Terahertz imaging, millimeter-wave radar,” in Advances in Sensing with Security Applications, J. Byrnes, ed. (Springer, 2006), pp. 243-268.
31. D. R. Vizard, “Millimeter-wave Applications: From Satellite Communications to Security Systems,” Microwave J. **49** (7), 22-36 (2006).
32. L. Dolphin, “Ground Penetrating Radar (GPR) Usage and Limitations,” http://www.ldophin.org/GPRLimits.html.
33. University of Idaho, “The Twelve Soil Orders: Soil Taxonomy,” http://soils.ag.uidaho.edu/soilorders/orders.htm.

34. J. Curtis, D. Leavell, C. Weiss, R. North, E. Smith, J. Cortes, R. Castellane, and M. Fields, "Characterization of Soils from the Night Vision and Electronic Sensors Directorate Mine Lane Facility, Fort Belvoir, VA," US Army Corps of Engineers, Engineer Research and Development Center project Report, (2003)
35. F. Press and R. Siever, *Earth, 4th Ed.* (Wilt, Freeman & Co., 1986).
36. E. V. Loewenstein, D. R. Smith, and R. L. Morgan, "Optical Constants of Far Infrared Materials. 2: Crystalline Solids," Appl. Optics **12** (2), 398-406 (1973).
37. G. Elert, "Index of Refraction of Vegetable Oil," http://hypertextbook.com/facts/2006/TingTingLuo.shtml
38. A. P. Annan, "Ground Penetrating Radar Workshop Notes," http://www.terrajp.co.jp/GPR.pdf.
39. A. J. Cox, A. J. DeWeerd, and J. Linden, "An experiment to measure Mie and Rayleigh total scattering cross sections," Am. J. Phys. **70** (6), 620-625 (2002).
40. E. W. Weisstein, "Sphere Packing," http://mathworld.wolfram.com/SpherePacking.html.
41. United Nations Mine Clearance and Policy Unit, Department of Humanitarian Affairs, "Landmines Fact Sheet", http://www.un.org/Pubs/CyberSchoolBus/banmines/facts.asp.
42. K. Kowalenko, "Saving lives, one land mine at a time," The Institute **28**, 10, 2004.
43. M. Acheroy, "Mine action: status of sensor technology for close-in and remote detection of antipersonnel mines," *in Proc. Of 3rd International Workshop on Advanced Ground Penetrating Radar* (Delft, Netherlands, 2005), pp. 3-13.

44. M. Schachne, L. van Kempen, D. Milojevic, H. Sahli, Ph. Van Ham, M. Acheroy, and J. Cornelis, “Mine detection by means of dynamic thermography: simulation and experiments,” *in the Second International Conference on the Detection of Abandoned Landmines* (1998), pp. 124-128.
45. L. Yujiri, B. Hauss, and M. Shoucri, “Passive millimeter wave sensors for detection of buried mines,” Proc. SPIE **2496**, 2-6, (1995).
46. H. Zhong, N. Karpowicz, J. Partridge, X. Xie, J. Xu, and X.-C. Zhang, “Terahertz Wave Imaging for Landmine Detection,” Proc. SPIE **5411**, 33-44, (2004).
47. T. W. Du Bosq, R. E. Peale, and G. D. Boreman, Infrared Systems Laboratory, University of Central Florida, 4000 Central Florida Blvd, Orlando, FL 32816, are preparing a manuscript to be called “Terahertz/millimeter wave characterizations of soils for mine detection: transmission and scattering.”
48. X. Miao, M. R. Azimi-Sadjadi, B. Tian, A. C. Dubey, and N. H. Witherspoon, “Detection of mines and minelike targets using principal component and neural-network methods,” IEEE Trans. Neural Networks **9**, 454-463 (1998).
49. M. R. Azimi-Sadjadi, D. E. Poole, S. Sheedvash, K. D. Sherbondy, and S. A. Stricker, “Detection and classification of buried dielectric anomalies using a separated aperture sensor and a neural network discriminator,” IEEE Trans. Inst. Meas. **41**, 137-143 (1992).
50. B. Karlsen, J. Larsen, H. B. D. Sorensen, K. B. Jakobsen, “Comparison of PCA and ICA based clutter reduction in GPR systems for anti-personal landmine detection,” in *Proceedings of IEEE Conference on Statistical Signal Processing* (IEEE, 2001), pp. 146-149.

51. W. J. Smith, *Modern Optical Engineering* (McGraw-Hill, 1966).

52. National Defence Mine/Countermine Information Centre, The Department of National Defence, “Landmine Data Sheet,” http://ndmic-cidnm.forces.gc.ca.

53. D. F. Morrison, *Multivariate Statistical Methods, 3rd ed.* (McGraw-Hill, 1990).

54. J.M.Lopez-Alonso, J. Alda, and E. Bernabeu, ‘‘Principal components characterization of noise for infrared images,’’ Appl. Opt. **41**, 320–331 (2002).

55. J. Kositsky, R. Cosgrove, C. Amazeen, and P. Milanfar, “Results from a forward-looking GPR mine detection system,” Proc. SPIE **4742**, 206-217, (2002).

56. W. R. Folks, J.M. Lopez-Alonso, B. Monacelli, A. Weeks, G. Zummo, D. Mullally, G. D. Boreman, "Characterization of digital-micromirror device-based infrared scene projector, " Opt. Eng. **44**, 086402 (2005).

57. Lopez Alonso, J.M, Monacelli B., Alda J., Boreman G., “Uncertainty analysis in the measurement of the spatial responsivity of infrared antennas”, Appl. Opt. **44**, 4557-4568 (2005).

58. J. M. López-Alonso, J. M. Rico-García, and J. Alda, “Photonic crystal characterization by FDTD and principal component analysis,” Optics Express **12**, 2176-2186 (2004).

59. Schumaker, Wood, and Thacker, *Infrared Imaging Systems Analysis* (DCS Corporation, 1998).

60. L. David, “Opportunity Mars Rover Stuck in Sand,” http://www.space.com/missionlaunches/050428_ rover_update.html.

61. K. Young, “Mars Rover escapes from sand dune,” http://www.newscientist.com/article.ns?id=dn7473.

62. M. McKee, “One Mars rover gets stuck in, the other chills out,” http://www.newscientist.com/article/dn9253-one-mars-rover-gets-stuck-in-the-other-chills-out.html.

63. K. Young, “Mars Rover escapes from the “Bay of Lamentation,” http://space.newscientist.com/article/dn9286-mars-rover-escapes-from-the-bay-of-lamentation.html

64. T.W. Du Bosq, R.E. Peale, A. Weeks, J. Grantham, D. Dillery, D. Lee, D. Muh, and G. Boreman, “Terahertz/millimeter wave characterizations of soil for mine detection: transmission and scattering,” Proc. SPIE **5790**, 66-73 (2005).

65. T.W. Du Bosq, J.M. Lopez-Alonso, and G.D. Boreman, “Millimeter wave imaging system for landmine detection,” Appl. Optics **45** (22), 5686-5692 (2006).

66. H.A. Perko, J.D. Nelson, J.R. Green, “Mars soil mechanical properties and suitability of Mars soil simulants,” J. Aerospace Eng., 169-176 (2006).

67. P. Mouroulis and J. Macdonald, *Geometrical Optics and Optical Design* (Oxford,1997).

68. T. W. Du Bosq, A. V. Muravjov, and R. E. Peale, “High reflectivity intracavity Bragg mirrors for the far-infrared p-Ge laser,” Proc. SPIE **5411**, 167-173 (2004).

69. E. W Nelson, S. H. Withers, A. V. Muravjov, R. C. Strijbos, R. E. Peale, S. G. Pavlov, V. N. Shastin, and C. J. Fredricksen, “High resolution study of composite cavity effects for p-Ge lasers,” IEEE J. of Quantum Electronics **37**, 1525-1530 (2001).

70. E. Bründermann, “Widely Tunable Far-Infrared Hot-Hole Semiconductor Lasers,” in *Long-Wavelength Infrared Semiconductor Lasers*, H. K. Choi, ed. (Wiley, New Jersey, 2004), 279-350.

71. P. Brüesch, *Phonons: Theory and Experiments II* (Springer-Verlag, Berlin Heidelberg, 1986).

72. R. Schiwon, G. Schwaab, E. Bründermann, and M. Havenith, "Far-infrared multilayer mirrors," Appl. Phys. Lett. **83**, 4119-4121 (2003).

73. .A. Dobrowolski, "Optical Properties of Films and Coatings," in *Handbook of Optics: Fundamentals, Techniques, & Design Vol I*, M. Bass, ed. (McGraw-Hill, New York, 1995), 42.10-42.11.

74. T. W. Du Bosq, R. E. Peale, A. V. Muravjov, and C. J. Fredricksen, "Fixed wavelength selection for the far-infrared p-Ge laser using thin silicon intracavity etalon," Proc. SPIE **4968**, 119-125 (2003).

75. J. W. Cleary, C. J. Fredricksen, A. V. Muravjov, J. Enz, M. V. Douguikh, T. W. Du Bosq, R. E. Peale, W. R. Folks, S. Pandey, G. Boreman, and O. Edwards, "Scanning Fabry-Perot filter for terahertz spectroscopy based on silicon dielectric mirrors," Proc. SPIE **6472**, 64720E-1-64720E-12 (2007).

76. J. W. Cleary, R. E. Peale, R. Todi, K. Sundaram, and O. Edwards, "Finesse of silicon-based terahertz Fabry-Perot spectrometer," Proc. SPIE **6549** (2007).